Experimental distribution of entanglement in ion-photon quantum networks: Photon-pairs as resource

Dissertation

zur Erlangung des Grades
des Doktors der Naturwissenschaften
der Naturwissenschaftlich-Technischen Fakultät
der Universität des Saarlandes
von

Stephan Kucera

Saarbrücken
2019

Tag des Kolloquiums:	18.07.2019
Dekan:	Prof. Dr. Guido Kickelbick
Berichterstatter:	Prof. Dr. Jürgen Eschner
	Prof. Dr. Oliver Benson
Vorsitz:	Prof. Dr. Christoph Becher
Akad. Mitarbeiter:	Dr. Daniel Flormann

Abstract

The distribution of entanglement is one of the main tasks in quantum networks. It is the basis for many cryptographic protocols for secure data transmission as well as for distributed quantum computing, and offers a way to transmit qubits via quantum-state teleportation as an alternative to direct transmission.

This thesis reports on the setup, characterization and use of an entangled photon pair source for quantum network experiments based on spontaneous parametric down conversion. The source is resonant with the $D_{5/2}$-$P_{3/2}$ transition of $^{40}Ca^{+}$ at 854 nm and combines the spectral shaping and high pair rates of a doubly resonant cavity with the high-fidelity entanglement of sources in interferometric configuration. The photon pair source is used in experiments towards quantum network operations with a single trapped ion, acting as quantum node. Demonstrated are the heralded mapping of a photonic qubit to a spin qubit in the ion, the transfer of photon-photon entanglement to ion-photon entanglement by the mapping of one photon of an entangled pair, and the teleportation of a spin qubit from the ion onto a polarization qubit of one photon of an entangled pair. The interconnection of the photon-pair source to the telecom wavelength range is demonstrated in a preliminary experiment via polarization-independent quantum frequency conversion of one photon of a pair. The entanglement is preserved, which opens the way for long haul distribution of entanglement for quantum communication.

Zusammenfassung

Die Verteilung von Verschränkung ist eine der Hauptaufgaben in Quantennetzwerken. Sie ist die Grundlage vieler kryptographischer Protokolle für die sichere Datenübertragung sowie des verteilten Quantencomputings und bietet mit der Quantenteleportation eine Alternative Möglichkeit zur direkten Übertragung von Qubits.

Die vorliegende Arbeit beinhaltet Aufbau, Charakterisierung und Verwendung einer verschränkten Photonenpaarquelle für Quantennetzwerk Experimente basierend auf spontaner parametrischer Abwärtskonversion (SPDC). Die Paarquelle ist resonant mit dem $D_{5/2}$-$P_{3/2}$ Übergang von $^{40}Ca^{+}$ bei 854 nm und kombiniert die spektrale Anpassung und hohen Paarraten eines doppelt resonanten Resonators und die hohe Güte der Verschränkung von Quellen in interferometrischer Konfiguration. Die Paarquelle wird in Quantennetzwerkoperationen verwendet mit einem einzelnen gefangenen $^{40}Ca^{+}$ Ion als Quantenknoten. Demonstriert werden die angekündigte Abbildung eines photonischen Qubits auf ein Spin Qubit im Ion, die Erzeugung von Ion-Photon Verschränkung durch die Abbildung eines Photons eines verschränkten Photonenpaares, sowie die Teleportation eines Spin Qubits auf ein Polarisations Qubit eines Photons eines verschränkten Paares. Die Verbindung der Paarquelle an den Telekomwellenlängenbereich ist in einem vorbereitenden Experiment mittels polarisationsunabhängiger Quanten-Frequenzkonversion gezeigt die den Weg zur langreichweitigen Quantenkommunikation öffnet.

Contents

1. Introduction

The use of quantum effects for enhancement and extension of current technologies is a driving force in state-of-the-art research in the field of quantum technology. This field is mainly divided in quantum sensing, quantum simulation, quantum computing, and quantum communication, the latter being the topic of this thesis. The quantum sensing community investigates the opportunities to improve sensors and measurement devices with quantum effects beyond the classical limit [1]. A prominent example is the improvement of the sensitivity of gravitational-wave detectors by the use of nonclassical states of light. Another example is the use of certain entangled many-body states, known as NOON-states, in interferometry to beat the shot noise limit [1]. The field of quantum simulation addresses the problem of the computability of physical simulations with a classical computer [2, 3]. The number of operations for these simulations grow exponentially with the system size and become already difficult for relatively simple physical systems, even for the best available computers. The strategy in quantum simulation is to use a controllable quantum system to simulate Hamiltonians of other quantum systems, which is analogous to the classical analog-computing. Quantum computing generalizes a quantum simulator to a universal machine that allows to execute quantum algorithms [4–7]. Prominent examples are the Grover algorithm for database search with a quadratic speedup [8], and the Shor algorithm for prime factorization, which solves the problem in polynomial rather than exponential time [9]. The latter is especially of importance for currently used cryptographic systems, like the RSA for example, where the security is based on the computational hardness of factorization. The speedup in factorization of a quantum computer demands therefore for other cryptographic techniques. The currently competing technologies in quantum computing rely on registers of superconducting qubits [10, 11], or on single ions as qubits trapped in a Paul trap [7]. Recent publications report on implementations of quantum error correction on a superconducting circuit with $4-9$ qubits [12–14], and on a ion-trap setup with $3-4$ qubits [15, 16]. Maximally entangled Greenberger-Horne-Zeilinger states with a register of up to 14 qubits are reported on a ion-trap setup in 2011 [17] and with 20 qubits in 2018 [18]. These exam-

ples show the remarkable ongoing progress. Companies start talking about quantum computers with more than 49 qubits in the near future [19].

Quantum networking explores the possibilities to send, transmit, and receive quantum information, such as the direct transfer of a qubit, and the distribution of entanglement in a network scenario. Quantum cryptography, or quantum key distribution (QKD) is a subdivision of this field, which enables secure data transfer. The security in this case is warranted by the laws of physics rather than by mathematical algorithms: "[...] *two users, who share no secret information initially, must at a certain stage of communication use a reliable and a very secure channel. Since the interception is a set of measurements performed by the eavesdropper on this channel, however difficult this might be from a technological point of view, in principle any classical channel can always be passively monitored, without the legitimate users being aware that any eavesdropping has taken place. This is not so for quantum channels*" (Artur K. Ekert (1991) [20]). The quantum cryptography is therefore the answer to the security loophole that a quantum computer will open. There are already commercial quantum cryptography systems[1] available that are used in existing fiber infrastructure. But although the underlying process is proven to be secure, the security is always vulnerable to imperfections of the device, for example in the characterization of the physical channel, or the cryptosystem hardware. Experimentalists already successfully attacked commercially available quantum cryptosystems [21, 22]. To make use of the potentially perfect security, all the device loopholes must be closed. The device-independent quantum cryptography addresses this problem in a way to specify the security of a cryptosystem without making assumptions on the device itself.

But how should a quantum network look like? The quantum network could exist in parallel to the classical network, and extends its technological possibilities [23, 24]. The analogy to the classical network that spans the whole Internet is that there are nodes in which quantum information is generated, stored, and processed in its qubits, and channels between the nodes to exchange information. Single photons as carrier for quantum information in optical fibers or in free space are excellent candidates to implement channels between the nodes. They are as fast as possible, and offer rich possibilities to encode a qubit, for example in polarization, frequency- and spatial-mode, time-bin or orbital angular momentum. The already existing worldwide fiber infrastructure makes the low-loss telecom-wavelength range from 1260 nm to 1625 nm favorable for long haul communication tasks. Examples of systems that are suitable

[1] ID Quantique: www.idquantique.com

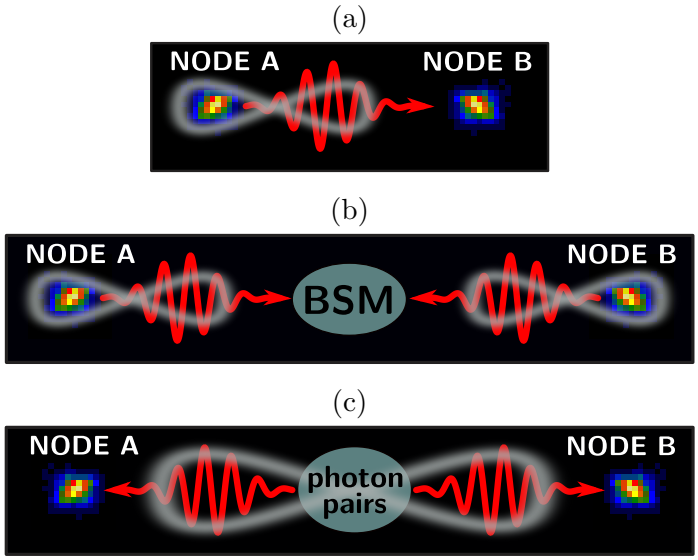

Figure 1.1.: Schemes for node-node entanglement: (a) Direct. (b) Via entanglement swapping. (c) External resource of entanglement.

as node qubits are single trapped atoms, vacancy centers in diamond, molecules, quantum dots, superconducting circuits, and clouds of atoms. From the existing implementations, single trapped ions or atoms are the most advanced and versatile quantum system in terms of existing interfaces to the channel [25–28], storage times [29–31], and the control of qubits that are implemented in their internal degrees of freedom [32]. Other systems are still in the race, for example: Diamond vacancy centers in combination with their nuclear spins offer excellent coherence properties with storage times exceeding 10 s [33]. Quantum dots have been proven to be good single photon sources that offer direct compatibility with telecom wavelength. Clouds of atoms offer high absorption efficiencies, and have multi-mode memory capacity. And the idea of printing a quantum system becomes possible with superconducting circuits.

Apart from the physical implementation the basic operations of a quantum network are the direct transmission of qubits, and the distribution of entanglement between the nodes. The direct transmission requires two interfaces. The first is the mapping of a qubit from a node qubit to a photon, and the second from a photon to the node qubit. The establishment of entanglement between two node qubits has several possibilities. Three of them are depicted in figure 1.1. Scheme (a) starts with the generation of node-photon entanglement at node A and then guides the channel photon to node B.

Subsequent photon-to-node state mapping at B establishes the node-node entanglement. Examples of the direct interaction without the distribution of entanglement have been demonstrated with distant single ions [34], and between a semiconductor quantum dot and a trapped ion [35], and with distribution of entanglement between separate neutral atoms in a cavity [36].

Scheme (b) is known as entanglement-swapping [37]. It starts with the generation of node-photon entanglement in both nodes. The two channel photons are then guided to a Bell-state measurement (BSM) setup, whereby the projective detection of a maximally entangled Bell state results in a entangled state between the selected node qubits [38]. The scheme is well experimental studied, for example with distant single trapped atoms [39], with distant diamond vacancy centers [40], or with distant atomic ensembles [41]. The third option makes use of an external resource, that generates entangled photon pairs, whereby one of the two photons is guided through the channel to node A and its partner photon to node B. The entanglement is then transferred onto the nodes by mapping the state of both photons onto the node qubits (figure 1.1 (c)) [42]. This scheme is not yet demonstrated.

The three schemes end up in entanglement between the nodes, a comparison of the schemes is possible in terms of the achievable communication data rate. This data rate is strongly dependent on the interface efficiencies of the used system, and the compatibility in terms of their spectral properties between the channel photon and the node system. One solution for the compatibility of quantum systems that are dissimilar in frequency is given by quantum frequency conversion (QFC) to a common bus wavelength, for which the telecom range is favorable, for long haul communication [43]. QFC is nowadays a well established technique and complete devices with total efficiencies well above 25 % are reported based on nonlinear waveguides [44]. The missing efficiency of the reported devices mainly comes from coupling efficiencies and not from a principle boundary, which makes them to a promising technique. A common loss of such a basic networks, independent of the used system, are the exponential scaling losses of the used channel. They are minimized by the use of telecom wavelength in optical fibers but become serious when the channel length extends beyond the tens of kilometer range. A quantum repeater [45] scheme overcomes the exponential scaling losses, by dividing the channel and adding more stationary nodes connected via a shorter transmission channel. The idea is that each neighboring node first establishes multiple pairs of entangled qubits, a protocol called entanglement purification [46] combines these multiple pairs to a single pair with higher entanglement fidelity. This high fidelity entanglement between each neighboring node is then transferred to two

outer nodes of the initial 'long' channel by entanglement swapping [37]. The quantum repeater scheme circumvents the exponential scaling losses with the cost of a polynomial increasing number of resources. Following the idea of a quantum network in a mesh type topology, the quantum repeater scheme can be adapted to establish entanglement between arbitrary nodes [23, 24].

Once a link via two entangled nodes is established, the above mentioned QKD protocols can be applied for secure data transmission, and quantum-state teleportation for quantum-data exchange: "*The existence of long range correlations between Einstein-Podolsky-Rosen (EPR) pairs of particles raises the question of their use for information transfer. Einstein himself used the word 'telepathically' in this contempt. It is known that instantaneous information transfer is definitely impossible.* [...] *EPR correlations can nevertheless assist in the 'teleportation' of an intact quantum state from one place to another, by a sender who knows neither the state to be teleported nor the location of the intended receiver*" (Bennett 1993 [47]). Experimental implementations of teleportation between photons range from laboratory situations [48, 49], over the Swisscom telecommunication network [50], over 100-kilometer free-space channels crossing the Qinghai Lake in China [51], between two canarian islands over 143 kilometres [52, 53], and recently between the ground and a moving low-Earth-orbit satellite of up to 1400 kilometer distance [54]. Between photonic states and a node qubit it was demonstrated from a coherent state into an atomic ensemble of cesium atoms [55], from a single photon to rubidium mot over 7m [56], and from a single telecom photon to a solid-state diamond vacancy center [57]. Teleportation was also realised between remote single-atom quantum nodes [58], between atomic-ensemble nodes via projective measurements [59], and between distant solid-state diamond-vacancy centers as nodes [60]. These experimental implementations of the protocol since the invention in 1993 with a variety of systems are a nice example of the fast growing and promising field of quantum network technologies.

This Thesis forms a part of an experiment that started in 2004 at The Institute of Photonic Sciences (ICFO) in Barcelona. The target of the experiment is to investigate quantum network technologies by the use of $^{40}Ca^{+}$ ions as node qubits. The essential elements of the experiment are two ion traps in ultra-high vaccum to trap single or strings of $^{40}Ca^{+}$ ions, a complex laser system, an optical system to collect fluorescence and to address the ions with the lasers, and control electronics. The setup enables a high degree of control over the quantum states of the trapped ions. The trap apparatus, laser system, control electronics for the $^{40}Ca^{+}$ ion, and a photon-pair source were set up, and tested in experiments in Barcelona [61–64]. The experiment

moved in 2010 to Saarbrücken, where my former colleagues improved many parts of the experiment, and extended the experimental toolbox by coherent control operations [65–67], which are an essential prerequisite for this thesis. An overview of the setup is given in chapter 2.

When I joined the group, the *"old"* photon-pair source [64, 68] was still in use and experiments with the a single trapped ion, a photon-pair source, and the frequency converter of the workgroup of Christoph Becher were performed, extending the experiments to low-loss telecom wavelengths [69, 70].

This thesis reports on the setup of a new entangled photon-pair source in chapter 3. The source combines state of the art technologies to get narrowband, frequency-degenerate, and polarization-entangled photon pairs that are resonant with the $^{40}Ca^{+}$ ion. The implementation of new electronics to control the ion in experiments with a high level of automation is also part of this thesis. A program based on Matlab[2] was developed to control the sequential execution of calibration measurements, and quantum network experiments. The maintenance and completion of the program was mainly done by my colleague Matthias Kreis. A major part forms the quantum network experiments in chapter 4 with the photon-pair source and a single trapped $^{40}Ca^{+}$ ion used as quantum node. The first experiment in section 4.2 demonstrates the mapping of a polarization qubit onto the node with defined quantum states. The used protocol of 4.1 was already demonstrated with laser photons in [26, 66, 71] and is now performed with heralded single photons from the photon pair source. The second experiment in section 4.3 realizes the conservation of entanglement by the mapping process. For this purpose, a photon-photon entangled state is mapped to an atom-photon entangled state by heralded absorption of one photon of an entangled pair. This experiment is a step towards the distribution of entanglement according to figure 1.1(b) with an external resource in a quantum network. Quantum-state teleportation from the atom onto one photon of an entangled pair is demonstrated in section 4.4. The key element of the teleportation is the Bell-state measurement, which is partially performed by the absorption process.

Finally the interconnection of the photon-pair source to the telecom wavelength range via polarization-independent quantum frequency conversion is demonstrated in section 4.5. The converter is build, and operated by our colleagues from the workgroup of Christoph Becher at our university [44, 69, 72]. It is located in the same building on a different floor, and connected via a 90 m long optical fiber. A tomography of

[2]MATLAB, MathWorks

the polarization entanglement after conversion demonstrates the compatibility of the converter, which opens the road for long haul quantum communication.

In parallel to the work of this thesis additional interfaces between the $^{40}Ca^{+}$ ion and single photons at 854 nm have been implemented by my colleagues. For example the generation of ion-photon entanglement at 854 nm by single-photon emission from the $^{40}Ca^{+}$ ion and subsequent quantum frequency conversion to a telecom wavelength at 1310 nm [44, 72, 73]. Also a direct atom-to-photon state-mapping scheme of the node qubit onto a 854 nm polarization qubit by the emission of a single photon is presented in [73]. Also the effect of detuning on the phase of a mapped qubit in the photon-to-atom state mapping protocol has been investigated and described in [74, 75].

2. $^{40}Ca^{+}$ as quantum node

Single trapped ions are paradigmatic examples of isolated quantum systems. The experimental proven control over the internal dynamics, motion, and the good isolation to environmental perturbations make them versatile systems for quantum network and quantum computing technologies. The ion used in our group is the single ionized calcium $^{40}Ca^{+}$ ion. It is well studied and widely used in the community. A main reason for our group to choose this element was the availability of entangled photon-pair sources – resonant with the near infrared dipole transitions at 850 nm/854 nm – when the experiment was started. Figure 2.1 shows the relevant level scheme including wavelengths, Landé-factors, and Einstein coefficients of the transitions. The two

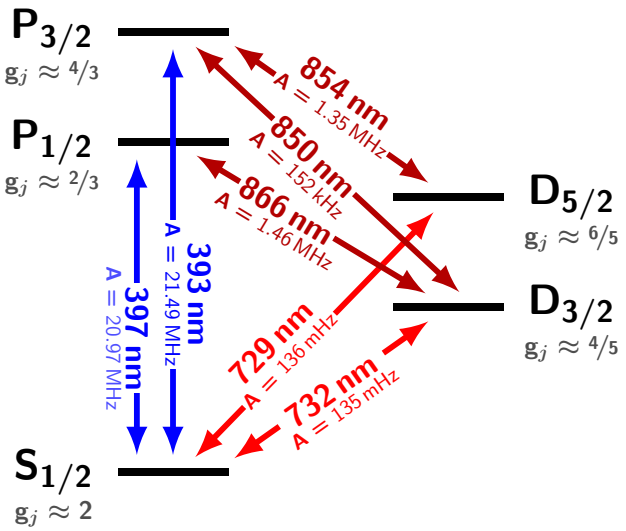

Figure 2.1.: $^{40}Ca^{+}$ level scheme: Wavelength, landé-factors g_j, and Einstein coefficients A of the relevant transitions.

short-lived states $P_{1/2}$ and $P_{3/2}$ with a lifetime of about 7 ns provide efficient laser cooling and fluorescence detection, and the two metastable states $D_{3/2}$ and $D_{5/2}$ with

a lifetime of about 1.17 s provide the possibilities of defining a qubit, and performing quantum logic operations.

This chapter briefly introduces the experimental setup with the main components needed to operate the ion as a quantum node. An overview about the experimental 'toolkit', such as cooling, optical pumping, coherent manipulations, or fluorescence detection with our setup is given in the dissertations by Jan Huwer [65] and Christoph Kurz [66].

2.1. Ion trap setup

Figure 2.2 shows pictures of the optical table with the two vacuum vessels, each containing a Paul trap setup (*c.f.* section 2.1.1). Historically, they where named as *dark trap* (left) and *bright trap* (right), because of a slightly different color after unpacking of the two vacuum chambers.

The coils mounted at the top and side flanges are used to generate the magnetic field for Zeeman splitting. The optical components around the chambers are used for imaging, collection of fluorescence, spatial mode matching, and access of the laser-light. The black box in the center of the upper picture contains an EMCCD camera[1]. The two pictures in figure 2.2 are images of a single ion and a string of two ions, trapped inside the bright trap, in which the experiments presented in this thesis were performed.

[1] Andor, DV887DCS-BV

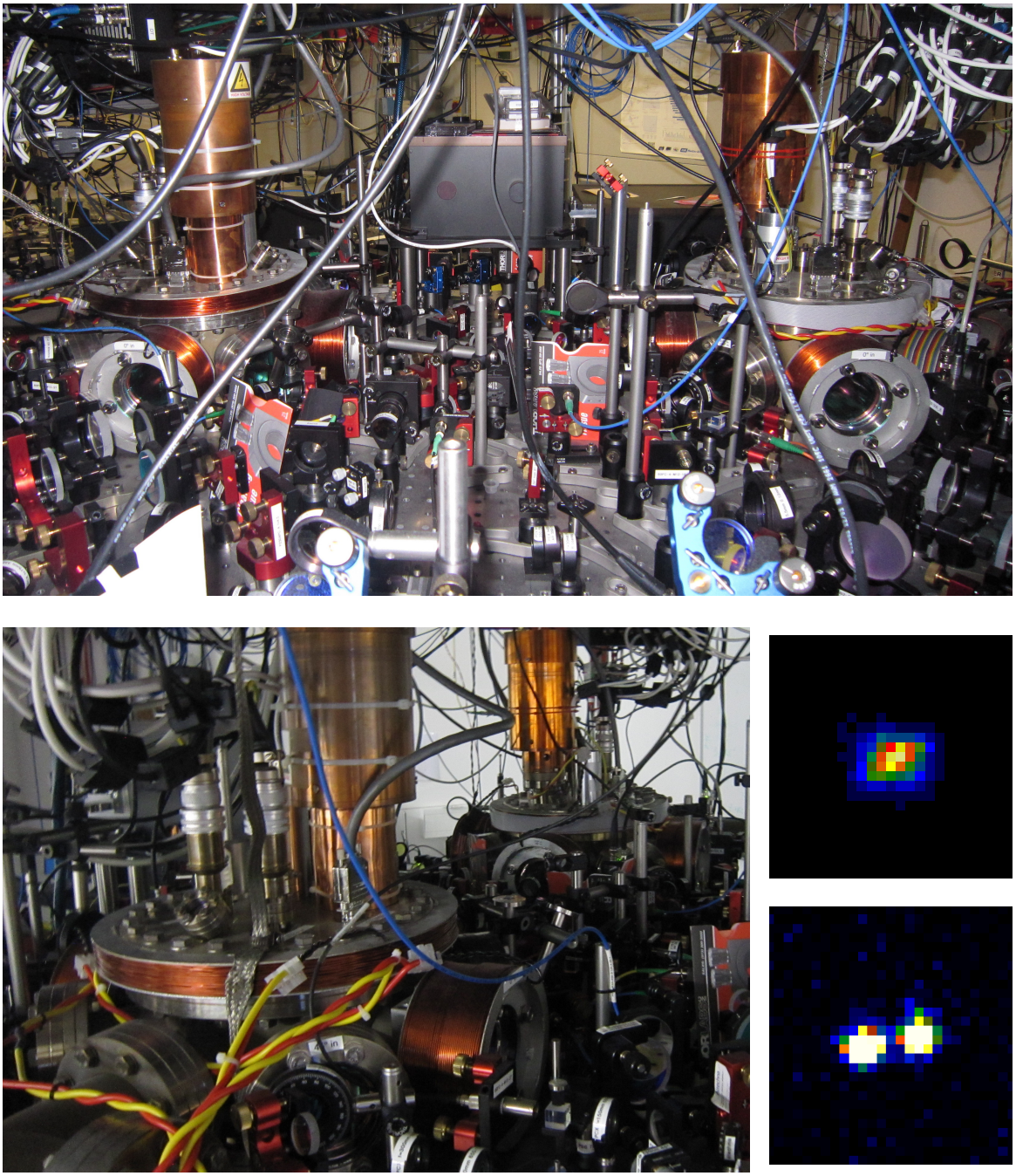

Figure 2.2.: Pictures of the optical table with the two vacuum chambers, and a camera observation of the fluorescence of a single ion and two trapped ions (1 pixel $\approx$ 0.8 µm).

2.1.1. Trapping ions: Linear Paul trap

The problem to trap charged particles is that an electrostatic potential cannot maintain stable conditions to confine them in all three dimensions (Earnshaw's theorem). The Paul trap circumvents this problem by the use of a rapidly oscillating potential, and the inertia of the particles. The direction of the forces onto the particles are thereby periodically switched, which forms an averaged confinement under specific conditions. In general the force must be inverted faster than the time needed to escape the trap. A detailed description is found in [76, 77]. Figure 2.3 shows a

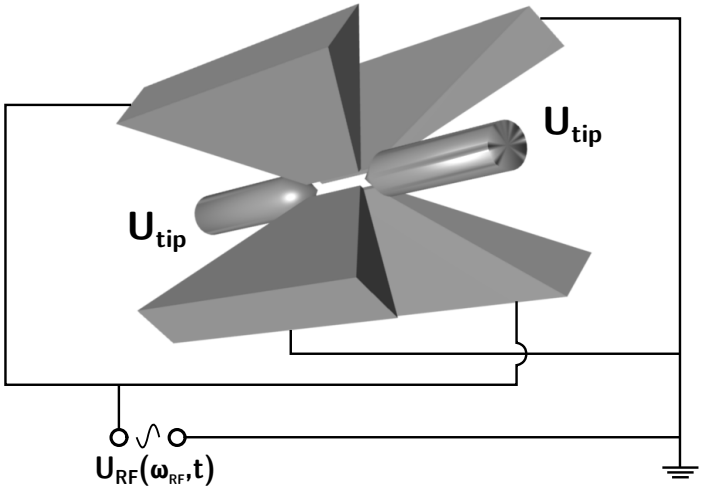

Figure 2.3.: Schematic of a linear Paul trap. The oscillating potential $\mathrm{U_{RF}}(\omega_{\mathrm{RF}}, t)$ is applied between the two pairs of opposite electrodes, and the static potential $\mathrm{U_{tip}}$ at the two end-tip electrodes.

schematic of the linear Paul-trap used in our experiment. The oscillating potential $\mathrm{U_{RF}}$ is applied on the four blade electrodes with frequency ω_{RF}, typical in the radio frequency range. The confinement along the symmetry axis $\vec{z}$ is realized by a static potential $\mathrm{U_{tip}}$ on this axis, applied on the end-tip electrodes. The confinement on this axis is smaller than on the others which forces the particles to arrange in strings along $\vec{z}$. When solving the equation of motion (*c.f.* Mathieu equations) for a particle with charge e and mass m, one finds that the motion is approximated by

$$r_i(t) \propto \cos(\omega_{sec,i}\, t)\, \left(1 - \frac{q_i}{2}\, \cos(\omega_{\mathrm{RF}}\, t)\right) \qquad \text{with} \quad i = x, y, z \tag{2.1}$$

$$q_y = -q_x = \frac{2\, e\, U_{\mathrm{RF}}}{m\, l_r^2\, \omega_{\mathrm{RF}}} \qquad , \qquad q_z = 0 \tag{2.2}$$

which is the superposition of a low frequency oscillation with $\omega_{sec,i}$, called secular motion, and a less pronounced fast oscillation at the drive frequency ω_{RF} , called micro motion. When neglecting the micro motion then the motion is well described by a three dimensional harmonic oscillator with eigen-frequencies

$$\omega_{x,y} = \frac{\omega_{\mathrm{RF}}}{2}\sqrt{\frac{q_{x,y}^2}{2} - \frac{4\,e\,\alpha'\,U_{\mathrm{tip}}}{m\,l_z^2\,\omega_{\mathrm{RF}}^2}} \qquad , \qquad \omega_z = \frac{\omega_{\mathrm{RF}}}{2}\sqrt{\frac{8\,e\,\alpha'\,U_{\mathrm{tip}}}{m\,l_z^2\,\omega_{\mathrm{RF}}^2}} \tag{2.3}$$

The parameter l_r is the distance from the trap center to the blade-electrodes and l_z is the distance from the trap center to the end tip electrodes. The numerical factor α' depends on the trap geometry, and takes shielding effects of the axial trapping potential into account.

Details of our trap apparatus including the electronics are found in the dissertations by Carsten Schuck [61] and Felix Rohde [62]. A picture of one of our traps is shown in the upper right part of figure 2.4. The stainless steal electrodes are mounted on the white holders made of Macor, a machinable glass ceramic. The distances are $l_z = 2.5\,\mathrm{mm}$ and $l_r = 0.8\,\mathrm{mm}$, and the geometry factor is approximately $\alpha' \approx 0.183$ [66, 67]. The two traps of our setup are operated at a frequency of $\omega_{\mathrm{RF}} = 2\pi \times 25.890\,\mathrm{MHz}$ with 8.5 W power (dark trap), and at $\omega_{\mathrm{RF}} = 2\pi \times 26.135\,\mathrm{MHz}$ with 9.6 W power (bright trap). This corresponds to a radio-frequency voltage amplitude $U_{\mathrm{tip}} \approx 1.5\,\mathrm{kV}$ applied to the blade electrodes and yields radial secular frequencies $\omega_{x,y} \approx 2\pi \times 3.7\,\mathrm{MHz}$. The end-tip electrodes are usually operated at a voltage of $U_{\mathrm{tip}} = 400\,\mathrm{V}$, resulting in axial secular frequencies of $2\pi \times 1.195\,\mathrm{MHz}$ for the bright trap and $2\pi \times 1.166\,\mathrm{MHz}$ for the dark trap. Extracted from these values is the parameter $|q_{x,y}| = 0.413$ (*c.f.* equation 2.2) [65, 66]. The four thin wires are used as compensation electrodes between the top and the bottom blade electrodes. They are used to correct for external electric fields that push the particle from the trap center, whereby the strength of the micro motion is increased. The position of these electrodes is a mistake in the design. It was chosen to have optimal optical access to collect fluorescence from a trapped ion, but the blade electrodes are shielding the compensation effect in the direction of the objectives. It is therefore not possible to apply sufficient micro motion compensation on this axis.

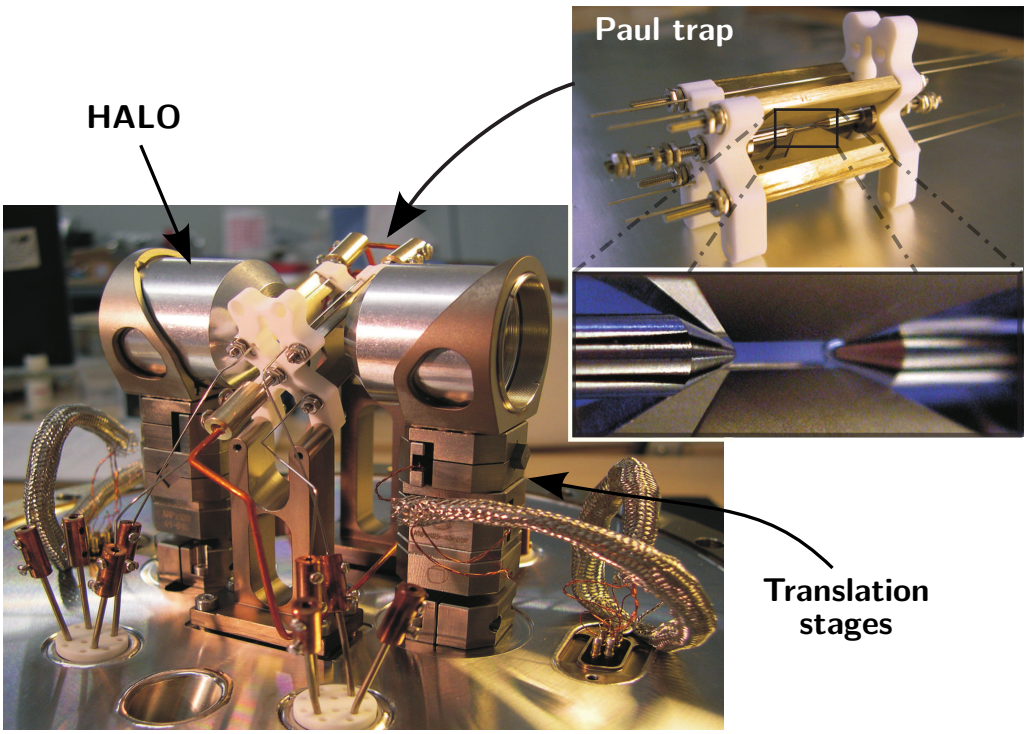

Figure 2.4.: Picture of the setup inside the vacuum chamber, one can see the trap between the two Objectives (HALO) that are mounted on the Translation stages . The trap is tilted by 22.5° for better optical access.
Inset: The assembled Paul trap.

2.1.2. Optical access: HALO

The lower left part of figure 2.4 shows the assembled setup, mounted on the top flange of the vacuum chamber. The Paul trap is located in the center, with two High numerical Aperture Laser Objective (HALO) mounted on both sides of the trap. Each HALO is hanging on xyz-translation stages[2] that allow for sub micrometer positioning of the objectives. The key facts of the objectives are a numerical aperture of 0.4 that translates to an opening angle of 47.2°, and corresponds to a covered solid angle of $\Omega = 4.17\,\% \cdot 4\pi$, and diffraction limitation over the whole range of required wavelengths from 400 nm to 870 nm. The aperture is 22 mm, and the transmission is 95.7 % at

[2]Attocube: ANPx100 and ANPz100

397 nm, and 98.8 % at 850 nm to 866 nm, calculated by the manufacturer[3]. The back focal lengths of the combined optical system at 397 nm is 13.7 mm, and 15.1 mm at 866 nm. The working distance of the objective from the focus position is 11.8 mm at 397 nm. The focal spot sizes are calculated to 1.2 µm at 397 nm and 2.6 µm at 866 nm. More details are found in the dissertation [61]. For our purposes, one HALO is typically aligned for optimal coupling to a single ion at 854 nm, and the second one for 397 nm.

2.1.3. Loading ions: Photoionization

The implemented ionization is based on a two-photon resonance-enhanced photoionization process. A resistive-heater tube oven filled with metallic calcium granules guides a evaporated beam of neutral Ca atoms through the trap center, where two light beams are overlapped with the atomic beam. The first beam excites the $4s^2\ ^1S_0$ to $4s4p\ ^1P_1$ transition at 422.67 nm. The light is generated by single-pass second harmonic generation in a ppKTP crystal pumped with a commercial grating-stabilized diode laser[4]. The second beam excites from $4s4p\ ^1P_1$ to high lying Rydberg states at a wavelength of 390 nm. The light is generated by a high-power UV LED[5] with 380 nm central wavelength and a FWHM bandwidth of about 30 nm. Both light beams are coupled to the same multi-mode 200 µm diameter fiber, and the output is focused to the trap center. The strong electric fields that are present in the Paul trap provide the remaining energy to release a high excited electron to the continuum. The ionization takes about $5 - 10$ minutes, and we are able to load a specific number of ions. A detailed described of the photoionization is found in [61, 78].

2.2. Laser system

Having full control over the $^{40}Ca^+$ ion requires a complex laser system with properties depending on the wavelength. On the one hand, one needs short term stability for different operations. Doppler cooling requires linewidths well below the natural linewidth. Coherent manipulations on a qubit transition require linewidths at least below the Zeeman splitting and the vibrational trap frequencies. When multiple coherent operations need to be done subsequently with high fidelity, then the required

[3]Linos
[4]Toptica, DL 100
[5]Nichia, NCCU001

linewidth can be even below 1 Hz.

On the other hand, long term stability is crucial for the measurement time of the experiments that range from minutes up to several days of continuous data collection. Two strategies are followed in our lab and described in the following sections, the first is a transfer lock scheme used for the laser with lower requirements, and second the stabilization onto an ultra high finesse optical resonator of the qubit laser.

Eight diode lasers are currently used in our lab:

- **846 nm:** Frequency doubled to **423 nm**, used for Photoionization.
- **852 nm:** Fundamental laser of the transfer lock scheme, stabilized to cesium.
- **393 nm:** Excitation of the $S_{1/2}$-$P_{3/2}$ transition, used for the generation of 393 nm fluorescence and single 854 nm photons, stabilized by transfer lock.
- **794 nm:** Stabilized by transfer-lock, frequency doubled to **397 nm**, used for Doppler cooling, fluorescence detection and polarization selective optical pumping.
- **866 nm:** Excitation of the $D_{3/2}$-$P_{1/2}$ transition, used as re-pump laser from the metastable $D_{3/2}$ level, stabilized by transfer lock.
- **850 nm:** Excitation of the $D_{3/2}$-$P_{3/2}$ transition, stabilized by transfer lock.
- **854 nm:** Excitation of the $D_{5/2}$-$P_{3/2}$ transition, used as re-pump laser from the metastable $D_{5/2}$ level, and generation of single 393 nm photons. Stabilized by transfer lock. Frequency doubled to **427 nm**, used as pump laser of the entangled photon-pair source.
- **729 nm:** Excitation of the $S_{1/2}$-$D_{5/2}$ qubit transition, stabilized on the ultra high finesse cavity. We obtain Rabi-frequencies of up to $\sim 2\pi \times 250$ kHz at a maximum power of ~ 70 mW at the trap.

All lasers are commercial grating-stabilized diode lasers in the Littrow configuration[6]. A wavemeter[7] is used for wavelength monitoring, and acousto-optic modulators (AOM) to control the frequency, amplitude and phase of the individual laser beams that are focused onto the trapped ion.

[6] 794 nm,854 nm: Toptica, TA-SHG pro
850 nm, 854 nm, 866 nm, 393 nm: Toptica, DL pro
729 nm: Toptica, TA pro

[7] High Finesse, WS7

2.2.0.1. Laser stabilization: Transfer lock

The idea of the transfer lock scheme is to combine the short term stability of low finesse Fabry-Pérot optical resonators with the intrinsic long term stability of the cesium D2 line in a vapor cell at room temperature. The locking scheme starts with the stabilization of the 852 nm reference laser by a combination of frequency-modulation spectroscopy and Doppler-free absorption spectroscopy of the D2 line of cesium. The stability transfer is obtained by stabilizing the length of Fabry-Pérot optical resonators ($\mathcal{F} \approx 500$, $\nu_{\mathrm{FSR}} = 1\,\mathrm{GHz}$, $\Delta\nu \approx 2\,\mathrm{MHz}$) to be resonant with the reference laser to obtain longterm stability of the absolute resonance frequency. The transfer lock is completed by locking the selected laser onto a different mode of this resonator. Such a transfer resonator is set up for each laser. The mirrors are built in confocal configuration, that allows for effective coupling under different angles. The feedback is applied onto a combination of a piezo stack for fast changes and the temperature expansion of the spacer to increase the range, which is necessary to compensate the air pressure changes over the day. The error signal for a PID-regulation is obtained by the Pound-Drever-Hall technique [79]. The frequency stability of the locked lasers is in the range of $\Delta\nu \approx 100\,\mathrm{kHz}$-$300\,\mathrm{kHz}$. A slightly different scheme is used for the locking of the 393 nm laser, because this laser is not frequency doubled. For this laser we use the stabilized and frequency doubled 397 nm light to lock the transfer resonator. The absolute frequency of the target laser is adjusted by choosing the longitudinal mode-number difference of the two modes that are used for locking the reference, and the target laser. More details and a characterization of the transfer-lock are found in [62, 80].

2.2.0.2. Laser stabilization: 729 nm qubit laser

The 729 nm laser is directly stabilized onto a passively stable ultra high finesse optical resonator[8], with a spacer made of ultra-low-expansion glass for best long-term mechanical stability. It is mounted in an ultra-high-vacuum chamber for environmental isolation. The spectral linewidth of the resonator is 4.0 kHz, and the free spectral range $\nu_{\mathrm{FSR}} = 1.9\,\mathrm{GHz}$ ($\mathcal{F} \approx 480000$). The error signal is obtained by the Pound-Drever-Hall technique [79] with a fast feedback loop[9]. The long-term drift is measured to be 80 mHz/s and the obtained laser linewidth is less than 32 Hz. More details are found in the dissertation of Jan Huwer [65].

[8] Coating: Advanced Thin Films ; Spacer: Corning
[9] Toptica, PDD 110 and FALC 110

2.3. Magnetic field

The magnetic field in the center of each trap is defined by 5 coils. Two pairs of small coils are attached to opposed CF flanges that allow the optical access from the side of the vacuum chamber (see figure 2.2). One larger diameter coil is mounted on the upper CF flange. The coils are directly connected to current supplies[10] with a longterm stability of $\sim 100\,\mu A$ [66]. The response at the position of the ion was measured to be 2.41 G/A [81] on axis of the HALO's, which results in a longterm stability of the magnetic field of $\sim 241\,\mu G$ at the ion.

Depending on the axis, a magnetic field strength of 2.8 G to 6 G at the ion position is reached. More details on the coils are found in the dissertation [62].

The experiments described in this thesis are performed with a magnetic field of 2.8 G on the axis the HALO's. The current of the other coils is adjusted to compensate for the earth magnetic field and other offset fields originating from our laboratory. To compensate for slow drifts, an additional compensation coil (~ 20 windings) around one of the main coils on HALO axis is used, and slow feedback is applied. The error signal is directly measured with the ion by a spectroscopy of the magnetic dipole transition ($S_{1/2}$, $m = -1/2$)-($S_{1/2}$, $m = +1/2$). A spectroscopy run with sufficient accuracy lasts about 10 s.

A serious problem are stray fields from the power line. The frequency of 50 Hz and its harmonics reduce the coherence time of the superpositions that are used to encode a qubit. Examples for superpositions that are used in this thesis are the ground-state qubit $\alpha\,|S_{1/2}, m = -1/2\rangle + \beta\,|S_{1/2}, m = +1/2\rangle$ and a qubit encoded in the outer Zeeman sublevels of the $D_{5/2}$ manifold $\alpha\,|D_{5/2}, m = -5/2\rangle + \beta\,|D_{5/2}, m = +5/2\rangle$. The sensitivity of the latter to magnetic field fluctuations is three times higher as in the ground state qubit due to its larger energy splitting. A single experimental run is typically faster than the 20 ms period of the power line. Each run is therefore exposed to a slightly different magnetic field which results in decoherence. One way to overcome this problem is to reduce the repetition rate of the experiments to 50 Hz to be in phase with the periodic magnetic field variation. In many cases, where one experimental cycle is completed in much less than 20 ms, this is on the cost of duty cycle down to a few percent which would extend the measurement time. It turned out that the amplitudes and phases of the frequency components remain relatively unchanged for several hours. Therefore a feed-forward compensation of the magnetic field at 50 Hz and 150 Hz is superimposed to the dc-field of the compen-

[10] TTI, QL355

sation coil. This signal is generated with an computer-controlled analog output[11] whose phase and frequency are locked to the power line, by generating the trigger for the waveform synthesis with a phase locked loop. Amplitude, and phase of the 50 Hz and 150 Hz components are measured and optimized with a Ramsey-type measurement. Such a measurement starts with optical pumping to $|S_{1/2}, m = -1/2\rangle$, a resonant radio-frequency $\pi/2$-pulse (*c.f.* section 2.4) is applied to generate the coherent superposition $(|S_{1/2}, m = -1/2\rangle + |S_{1/2}, m = +1/2\rangle)/\sqrt{2}$. A second $\pi/2$-pulse with an offset phase is applied after a fixed waiting time and we finally project onto $|S_{1/2}, m = \pm 1/2\rangle$ via electron shelving and fluorescence detection. By scanning the offset phase we obtain the Ramsey-fringe visibility which is dependent on the magnetic field fluctuations during the waiting time. We can increase the sensitivity by coherent transfer of the superposition from the $S_{1/2}$ state to the superposition in the $D_{5/2}$ state $(|D_{5/2}, m = -5/2\rangle + |D_{5/2}, m = +5/2\rangle)/\sqrt{2}$ with two subsequent coherent π-pulses with the narrowband 729 nm laser. After the waiting time we transfer the superposition back to $S_{1/2}$ with two π-pulses and continue with the second radio-frequency $\pi/2$-pulse. Due to the larger energy splitting an increase of three times in sensitivity for the fluctuations is obtained.

We then use the fringe visibility to optimize the feed-forward parameters, the amplitudes and phases of 50 Hz and 150 Hz components. The procedure for the optimization is the following: First a fixed amplitude at 50 Hz is applied, and the visibility in dependence of the phase is observed. The phase with highest visibility is selected. The next step is to scan the amplitude and set it to the best value in terms of visibility. The values for 50 Hz are left unchanged and the 150 Hz components are scanned in the same way. In the long term experiments, the coherence of the ion is monitored via the visibility of a Ramsey measurement with fixed waiting time in regular intervals. This allows to decide when the feed-forward optimization has to be repeated. The feed-forward optimization increases the coherence time of the ground-state qubit from $\sim 400\,\mu s$ to $\sim 800\,\mu s$. This compensation was mainly implemented by my colleague Matthias Kreis.

[11] national instruments: PCIe-6343

2.4. RF-coil

A magnetic field coil is used for coherent manipulations of the ($S_{1/2}$, m = $-1/2$)-($S_{1/2}$, m = $+1/2$) magnetic dipole transition. The coil is installed below the trap at a big viewport. It has 16 cm diameter, two loops, and forms with an additional capacitor an LC-circuit, whose resonance is tuned to the atomic resonance of $\sim 2\pi \times 7.8$ MHz (at ~ 2.8 G magnetic field) for resonant enhancement. Rabi-frequencies of $\sim 2\pi \times 100$ kHz are realized. More information is found in the dissertation [66].

2.5. Experiment control unit

The complex pulse sequences for experiments with single ions require on the one hand control over the frequency, amplitude and phase of the individual laser beams, which is done by acousto-optic modulators with a center frequency of 100 MHz to 200 MHz. On the other hand is the need to detect the quantum state of the ion, and to process conditions in real time. The necessary timescale of the control is in the range of nano to micro seconds for pulse length and decisions. The time precision needed for detecting single photons is in our experiments mainly given by the Larmor frequencies of superpositions that are in the range of a few 10 MHz. To resolve these frequencies sub nano second time resolution is necessary.

The control unit used in the experiments of this thesis is based on the PXI technology. The commercially available system has its roots in our group from the doctoral studies of Marc Almendros [63], who developed the prototype control unit, called HYDRA. This prototype was replaced by a the new commercially available system during this thesis. The advantage of the new system is that the number of PXI cards is easily expandable and the programming of the fast sequences is done in an easy to use flow-chart program[12]. The implementation of the new system into the experiment is also part of this thesis. A program based on MATLAB[13] to control the sequential execution of pulse sequences, which allows for a high level of automation in our experiment was developed. The maintenance, development of pulse-sequences, and completion of the program was mainly done by my colleague Matthias Kreis.

[12]The system was bought from Signadyne, a spin-off company of M. Almendros. Now they are part of Keysight.
[13]MathWorks

Currently the system consists of the following components:

- Arbitrary waveform generators (AWG):
  - 1 PXI card, 4 channels: 500 MSa/s, 16 bit, 200 MHz band-width[14].
  - 4 PXI cards, 16 channels: 1 GSa/s, 14 bit, 400 MHz band-width[15].
- Time to digital converter (TDC):
  - 1 PXI card, 8 channels: 320 ps time resolution [16].
- Digital input/output (DIO):
  - 64 digital I/O channels, 800 MBit/s [17].
- Extensions connected to the digital I/O:
  - Analog input (AI), 16 channel, 14 bit, 5.7 MHz cutoff frequency, with adjustable digital low-pass filter. More details are found in the diploma-thesis [82].
  - Camera readout electronics, for spatially resolved state discrimination of an ion-string, based on a fast micro-controller[18].
  - Currently in construction: High precision stopwatch for phase measurement. 55 ps time resolution.

The individual cards in the PXI chassis are fully synchronized, the frequency standard of the lab is an external rubidium atomic clock[19].

The programming of pulse-sequences is divided into two parts, a fast real-time program executed on the PXI cards named Hard Virtual Instrument (HVI), and a program executed on an attached pc that controls the HVI execution, processes the data, and acts as user interface. The main idea is that complex schedules, including loops and conditions, of different subsequent HVI executions are executed and evaluated automatically. Results of previously executed calibration measurements are then stored as an *ion parameter*, and thus available for the following pulse-sequences. Examples of calibration measurements are spectroscopy runs to determine precise

[14]Formerly: Signadyne, SD-PXE-AOU-H0002-1G, now: Keysight, M3201A
[15]Formerly: Signadyne, SD-PXE-AOU-H0002-1G, now: Keysight, M3202A
[16]Formerly: Signadyne, SD-PXE-TDC-H3345-1G, now: unknown
[17]Formerly: Signadyne, SD-PXE-DIO-H0002-1G, now: unknown
[18]STM Discovery F4 evaluation board
[19]Stanford Research Systems, FS725

transition frequencies, or scans to find the optimal length of Rabi-pulses that coherently manipulate the internal states of the ion.

The slow feedback on the magnetic field (*c.f.* section 2.3) is a good example for versatility of the program. The high precision on the absolute value of the magnetic field needed for the presented quantum network experiments is obtained with a control loop on the magnetic field as it is measured at the ion position. This is implemented with the ($S_{1/2}$, m = $-1/2$)-($S_{1/2}$, m = $+1/2$) transition line-center, measured via RF spectroscopy, which gives conclusion about the absolute magnetic field. A deviation of the measured magnetic field from the setpoint is then corrected with the compensation coil, which closes the slow feedback loop.

The typical schedule of the quantum network experiments in section 4 is then composed of a set of HVI executions for each measurement basis choice. This set consists of calibration measurements, and then a ~ 10 cycle loop where the magnetic-field feedback ($\sim 10\,\mathrm{s}$) alternates with the quantum network experiment ($\sim 2\,\mathrm{min}$). The set is then repeated until the required integration time is reached, and followed by the next measurement basis. The schedule runs fully automated and ensures the high stability of the magnetic field and the high fidelity of the coherent manipulations, which are required for the presented quantum network experiments.

2.6. Summary

The design and development of the experimental setup presented in this chapter involves the work of four generations of PhD students [61–67, 70]. It started at ICFO in Spain 2004 and its improvement is still in progress. So far, the experiments that have been carried out wit the simultaneous use of both traps are the demonstration of quantum interference [83, 84] and the direct heralded interaction [34] between two single trapped ions each trapped in one of the distant vacuum chambers. The statistical and spectral investigations of a single trapped ion used as single-photon [84, 85] and photon-pair [86] source are demonstrated. Quantum-beats, that have their origin in the interference of different amplitudes in absorption and emission were also demonstrated [87]. The theoretical work presented in [71] contains several schemes for heralded storage of polarization qubits of single photons in the internal states of the single ion. The demonstration of one of the schemes for heralded state mapping is presented in [26]. The scheme is extended in a programmable manner to atom-to-photon state mapping and the generation of atom-photon entanglement in [27]. The

experiments that were carried out with the *"old"* photon-pair source [68, 88], that is briefly described in the following chapter, demonstrate resonant interaction with the single ion [89], also in a heralded way [90] in a quantum jump detection scheme. This heralded interaction was also used to detect the polarization entanglement of the photon pairs [91]. Another experiment[20] demonstrates the absorption af a heralded single photon by the single ion whereby the generated Raman photon is used as herald of absorption [92]. The projective measurement of this herald of absorption is a prerequisite for the heralded state-mapping protocol [26]. Recent results demonstrate the generation of high fidelity entanglement between between the ion and a telecom photon via quantum frequency conversion [44].

The experimental setup is extended in the following chapter with a new photon-pair source which opens the way for new experiments with the ion towards a quantum network with single $^{40}Ca^{+}$ ions as quantum nodes.

[20] Which was carried out at the beginning of the work of this thesis

3. Photon-pair source

On demand photon pairs in a pure maximally entangled quantum state with tunable spectral and polarization properties to match arbitrary quantum-network systems, high rates and transmission-efficiencies, easy to operate, a favorable price in acquisition and maintenance, ... a possible abstract of a scientists and economists wish list in the field of quantum-network technologies. Each of the mentioned points is a subject of current research with remarkable ongoing progress. When discussing each point separately, most of them are already adequately fulfilled by state of the art technology. A natural strategic roadmap lies in the combination of technologies to improve the properties.

The definition of necessary requirements on a photon pair source suitable for quantum network experiments in combination with a $^{40}Ca^{+}$ ion as quantum node is a crucial step in the design of the presented source in this thesis. The basis is spontaneous parametric down-conversion (SPDC) in a $\chi^{(2)}$ nonlinear crystal, a process that converts a pump photon into two photons that are correlated in time, energy, and polarization. The availability of light sources as pump, and the efficiency of the SPDC crystals restricts the used transition in the $^{40}Ca^{+}$ ion to one of the near-IR transitions, *c.f.* figure 2.1, which is also advantageous in terms of transmission in optical fibers. The use of polarization-qubits, and the protocols of ion-photon interfaces is also subject of the research of our group, whereby the transition from $D_{5/2}$ to $P_{3/2}$ at 854 nm has beneficial properties because of its Zeeman sub-structure [71]. A first requirement on the photon-pair source is given by the linewidth and the absolute frequency of this transition, for efficient absorption of the photons. With $2\pi \cdot 22.5\,\mathrm{MHz}$ atomic linewidth we need narrowband photon pairs with longterm stability down to a fraction of the width. The geometrical restrictions for coupling and the oscillator strength of the transition give a restriction on the minimum pair rate to $> 1 \times 10^5$ to be able to realize the protocols in feasible measurement time. The purity of the entanglement is another requirement, which should be as high as possible. The situation at the beginning of this thesis was an existing pair source using single-passage SPDC in a periodically-poled $KTiOPO_4$ (ppKTP) crystal [68]. The $\sim 150\,\mathrm{GHz}$ spectral width

of the generated photon pairs was about 7000 times broader than the linewidth of the calcium ion. To match the transition, a spectral filter was designed to select the photons in a heralding arm in 22 MHz bandwidth. Energy conservation, and the narrowband pump laser ($\sim 400\,\mathrm{kHz}$) ensure that the heralded partner photons have the same bandwidth. But the filtering is on the cost of pair rate. At a maximum pump power of $\sim 55\,\mathrm{mW}$ a rate of $\sim 6000\,\mathrm{s}^{-1}$ generated ion-resonant pairs was reached [70].

Besides the choice of material, several strategies are used in the community to obtain such improvement. One way towards higher brightness is to increase the conversion efficiency by a better spatial mode overlap inside a waveguide structure. A disadvantage when coupling to an ion is the broadband emission compared to the atomic linewidth.

By the use of a macroscopic resonator that surrounds the nonlinear crystal, spectral brightness values on the order of 1×10^3 to $8 \times 10^3\,\mathrm{pairs/(s\,mW\,MHz)}$ have been reported [93–97][1]. An inherent advantage is the spectral redistribution of the emission into the longitudinal resonator modes, which simplifies the filtering to select a single frequency mode.

A remarkable improvement in terms of brightness is the integration of the resonator in the nonlinear material. A generated brightness of $1 \times 10^6\,\mathrm{pairs/(s\,mW\,MHz)}$ inside the resonator is reported in [98] by the use of a whispering-gallery mode resonator made of lithium niobate[2]. A combination of a resonator, and a waveguide structure is reported in [99] with an available brightness behind the resonator of $3 \times 10^4\,\mathrm{pairs/(s\,mW\,MHz)}$. These integrated combinations are still in an experimental stadium, therefore not commercially available, and their stability, as well as their spatial mode matching, turn out to be complicated.

An effect that further simplifies the spectral filtering is the so-called clustering.

[1] The numbers are specified in different ways. From the numbers given in the references, the available brightness behind the out-coupling mirror is inferred in the following way:
[93]: A ppKTP crystal inside a resonator with 7.2 MHz linewidth is used. They report $70\,\mathrm{pairs/(s\,mW\,MHz)}$ detected brightness and $3.4 \times 10^6\,\mathrm{pairs/(s\,mW)}$ generated photon pairs in $\sim$ 300 excited modes. The escape probability of 82 % leads to an available brightness of $1100\,\mathrm{pairs/(s\,mW\,MHz)}$.
[95]: A brightness of $\sim 330\,\mathrm{pairs/(s\,mW\,MHz)}$ is reported in a bandwidth of 2.7 MHz.
[97]: A brightness of $370\,\mathrm{pairs/(s\,mW\,MHz)}$ is reported in a bandwidth of 100 MHz.
[94]: A ppLN crystal inside a resonator with ~ 2 MHz linewidth is used. Reported is a generated brightness of $8000\,\mathrm{pairs/(s\,mW\,MHz)}$, when including the escape probability of ~ 50 % escape efficiency (reported are ~ 40 % to ~ 60 %) we get an available brightness of $2000\,\mathrm{pairs/(s\,mW\,MHz)}$.

[2] The escape probability of the photon pairs is not specified, a direct comparison is therefore not possible.

A mismatch in the free spectral range of the resonator, for the two sets of modes in which photon pairs are generated, is used in combination with the energy conservation of the conversion process, to excite only a few modes of the resonator inside the conversion bandwidth, which is called a cluster of modes. Examples are the sources in [94, 97] with only a few supported modes, and [99] with almost single frequency mode operation.

There exist several strategies to obtain polarization entanglement, two of them are described in the following. One possibility uses the splitting of orthogonal frequency degenerate photon pairs at a non-polarizing beam splitter. A detection of a photon in both arms projects the joint-state onto a Bell-bell state. This strategy was used in the *old* photon-pair source and 97.6(10) % fidelity was measured with the maximal entangled Bell state [88]. A drawback is that there exist two other cases at the non-polarizing beam splitter where both photons leave at the same output. These events produce additional background and reduce the fidelity. Another possibility combines the photon pair generation with an interferometer [100–103]. The interferometer first splits the pump-photons in two paths by a beam splitter, each path pumps a SPDC process which generates orthogonal polarized photon pairs. The interferometer paths are finally combined on a polarizing beam splitter and generate an entangled photon-pair state at the output. One advantage is that the pairs are always split at the polarizing beam splitter. This principle also works with non frequency degenerate photon pairs [103] and high fidelities ($> 99.5\,\%$ [101] for example) with a maximal entangled Bell state are reported. A special case is the use of a Sagnac type of interferometer, in this case the requirement of phase stability is simplified due to its intrinsic stability [101, 104].

The source described in this chapter is based on type-II conversion in a ppKTP crystal which has the highest nonlinear coefficient for the conversion from 427 nm to 854 nm. The generated photon pairs are orthogonally linear polarized, and frequency degenerate at the atomic resonance. The conversion is enhanced by a bow-tie ring resonator, resonant for both generated photons. The clustering effect is used to generate only one cluster with a few modes, which simplifies the spectral filtering. We decided to use a macroscopic resonator with an additional compensation crystal inside, to be able to tune the resonator doubly resonant for the two photons, and to the atomic resonance at the same time.

An overview on the expected photon pair quantum state is given in section 3.1. The influence of accidental coincidences on the fidelity that an unbiased observer will reconstruct is discussed in section 3.2. Section 3.3 contains details on the design

of the SPDC crystal, the resonator, and its expected tunability, furthermore it contains a characterization of the photon-pair source. Sections 3.3.8 and 3.4 contain two strategies for the generation of polarization entanglement. The first one uses a non polarizing beam splitter and post selection. The second one uses the principle of the interferometric-type sources, where the photon pair source is embedded in an interferometer for the pump and the output paths that enables the generation of high-fidelity entangled photon pair states without post selection.

3.1. SPDC quantum state

The derivation of the photon pair state is based on the explanations given in [99, 105, 106].

The polarization of a material depends upon the strength of the applied optical field $\vec{P}(\vec{E})$ ($\vec{P} = (P_1, P_2, P_3)$, $\vec{E} = (E_1, E_2, E_3)$). The nonlinearity is typically weak, this justifies the expansion into a Taylor series evaluated at $\vec{E} = \vec{0}$

$$\begin{aligned} P_i(\vec{E}) &= \epsilon_0 \left(\sum_j \frac{\partial P_i}{\partial E_j} E_j + \frac{1}{2} \sum_{jk} \frac{\partial^2 P_i}{\partial E_j \partial E_k} E_j E_k + \frac{1}{6} \sum_{jkl} \frac{\partial^3 P_i}{\partial E_j \partial E_k \partial E_l} E_j E_k E_l + \dots \right) \\ &= \underbrace{\epsilon_0 \sum_j \chi^{(1)}_{ij} E_j}_{P_i^L} + \underbrace{\epsilon_0 \sum_{jk} \chi^{(2)}_{ijk} E_j E_k + \epsilon_0 \sum_{jkl} \chi^{(3)}_{ijkl} E_j E_k E_l + \dots}_{P_i^{NL}} \end{aligned} \tag{3.1}$$

(3.2)

The coefficients $\chi^{(1)}_{ij}$, $\chi^{(2)}_{ijk}$, and $\chi^{(3)}_{ijkl}$ are the elements of tensors that correspond to the first, second and third order polarization of the material. The polarization is divided into the linear $\vec{P}^L$, and the nonlinear response $\vec{P}^{NL}$. The fact that three fields are involved in the second order polarization is the reason for the name *three wave mixing* or $\chi^{(2)}$-process. Two quantum applications are the quantum frequency conversion (QFC) and the spontaneous parametric down conversion (SPDC). In QFC a strong classical pump field is mixed with a single photon to convert this to the sum or difference frequency. SPDC is a process in which a photon of a pump field spontaneously generates two photons that are correlated in time, energy, and polarization.

In the following we focus on SPDC, we treat this process in perturbation theory, and derive the first and second order correction term of the quantum state. The first step is the simplification of the $\chi^{(2)}$ tensor. The Taylor expansion (Eq.3.1) shows that $\chi^{(2)}_{ijk}$ is proportional to $\frac{\partial^2 P_i}{\partial E_j \partial E_k}$, the partial derivatives can be exchanged, therefore $\chi^{(2)}_{ikj}$ is invariant to exchange of j and k ($\chi^{(2)}_{ijk} = \chi^{(2)}_{ikj}$). Furthermore lossless non-dispersive media have the intrinsic symmetry that they are invariant to permutations of the indeces. The remaining independent elements are listed in literature as an 3×6 array d_{iJ} with the assignment

J	1	2	3	4	5	6
jk	11	22	33	23, 32	31, 13	12, 21

for the six independent combinations of jk. Assuming three monochromatic waves

with frequencies ω_1, ω_2 and ω_3, one writes the three wave mixing process in the form

$$\begin{pmatrix} P_1(\omega_3) \\ P_2(\omega_3) \\ P_3(\omega_3) \end{pmatrix} = \begin{pmatrix} \mathrm{d}_{11} & \mathrm{d}_{12} & \mathrm{d}_{13} & \mathrm{d}_{14} & \mathrm{d}_{15} & \mathrm{d}_{16} \\ \mathrm{d}_{21} & \mathrm{d}_{22} & \mathrm{d}_{23} & \mathrm{d}_{24} & \mathrm{d}_{25} & \mathrm{d}_{26} \\ \mathrm{d}_{31} & \mathrm{d}_{32} & \mathrm{d}_{33} & \mathrm{d}_{34} & \mathrm{d}_{35} & \mathrm{d}_{36} \end{pmatrix} \begin{pmatrix} E_1(\omega_1)E_1(\omega_2) \\ E_2(\omega_1)E_2(\omega_2) \\ E_3(\omega_1)E_3(\omega_2) \\ E_2(\omega_1)E_3(\omega_2) + E_3(\omega_1)E_2(\omega_2) \\ E_3(\omega_1)E_1(\omega_2) + E_1(\omega_1)E_3(\omega_2) \\ E_1(\omega_1)E_2(\omega_2) + E_2(\omega_1)E_1(\omega_2) \end{pmatrix} \tag{3.3}$$

with fulfilled frequency-, and phase-matching conditions:

$$\omega_3 = \omega_1 + \omega_2 \qquad \vec{k}_3 = \vec{k}_1 + \vec{k}_2 \tag{3.4}$$

The coefficients can be categorized in three groups, depending on the three polarizations of the fields

- type-0 : All three polarizations point in the same direction ($i = J$).
- type-I : The generated polarizations point in the same direction, orthogonal to the pump ($i \neq J$ and $J \leq 3$).
- type-II : The generated polarizations are orthogonal ($J \geq 3$)

Depending on the dispersion properties of a material one can select the coefficient for which the phase-matching conditions 3.4 are fulfilled.

We treat the nonlinear interaction in perturbation theory to calculate the generated quantum state. A second order nonlinear material, and a fixed polarization of the pump along the z-axis are assumed. The interaction Hamiltonian in the interaction volume V is written as

$$\begin{aligned} \hat{H}_I &= \frac{1}{2}\int_V dV\ \hat{\mathbf{P}}_{NL} \cdot \hat{\mathbf{E}} \\ &= \frac{\epsilon_0 A}{2}\int_L dz\ \big(\sum_{jk} \chi^{(2)}_{1jk}\hat{E}_j\hat{E}_k\big)\cdot\hat{E}_1 + \big(\sum_{jk}\chi^{(2)}_{2jk}\hat{E}_j\hat{E}_k\big)\cdot\hat{E}_2 \end{aligned}$$

simplified by the cross section A and the interaction length L. Now we specify the material to KTP with the susceptibility [64, 107]

$$d_{i,J} = \begin{pmatrix} 0 & 0 & 0 & 0 & 6.1 & 0 \\ 0 & 0 & 0 & 7.6 & 0 & 0 \\ 2.4 & 4.4 & 16.9 & 0 & 0 & 0 \end{pmatrix} \text{pm/V} \tag{3.5}$$

and select the highest nonlinear coefficient for type-II phase matching d_{24}, and neglect all other components. For historic reasons we call the three fields *signal*, *idler*, and *pump* (s, i, p). The interaction Hamilton operator simplifies to

$$\hat{H}_I = \frac{\epsilon_0 A}{2} \int_L dz \; \mathrm{d}_{24} \, \hat{E}_s \hat{E}_i \hat{E}_p \tag{3.6}$$

The signal and idler fields are expressed by the quantized vacuum field operator

$$\hat{E}(z,t) = \frac{i}{2\pi} \int d\omega \sqrt{\frac{\hbar\,\omega}{2\,\epsilon_0\,c^2\,l}} \left(\hat{a}_\omega \exp\left[i\,(kz - \omega t)\right] + \hat{a}^\dagger_\omega \exp\left[-i\,(kz - \omega t)\right] \right) \tag{3.7}$$

with quantization volume l^3. The strong pump field is expressed as a classical monochromatic wave $E_p(z,t) = E_p \cdot \exp\left[i\,(k_p z - \omega_p t)\right]$.

A technique called periodic poling is used to match the phase of the three waves. During the manufacturing of the crystal, strong electric fields are applied to change the crystal structure periodically at a length Λ. This results in a periodic altered sign of the nonlinear coefficient which is now dependent of the position

$$\begin{aligned} d(z) &= \begin{cases} +d_{24} & 0 \quad < (z \mod \Lambda) \leq 0.5\Lambda \\ -d_{24} & 0.5\Lambda < (z \mod \Lambda) \leq \Lambda \end{cases} \\ &\approx \frac{4\,d_{24}}{\pi} \sin\left(\frac{2\pi\,z}{\Lambda}\right) \end{aligned} \tag{3.8}$$

and approximated by a sine function. The interaction Hamiltonian is then written as

$$\begin{aligned} \hat{H}_I = -\frac{A\,\hbar\,d_{24}\,E_p}{4\,\pi^3\,c^2\,l} & \int_L dz \; \sin\left(\frac{2\pi\,z}{\Lambda}\right) \cdot \exp\left[i\,(k_p z - \omega_p t)\right] \\ & \cdot \int d\omega_s \sqrt{\omega_s} \left(\hat{a}_{\omega_s} \exp\left[i\,(k_s z - \omega_s t)\right] + \hat{a}^\dagger_{\omega_s} \exp\left[-i\,(k_s z - \omega_s t)\right] \right) \\ & \cdot \int d\omega_i \sqrt{\omega_i} \left(\hat{a}_{\omega_i} \exp\left[i\,(k_i z - \omega_i t)\right] + \hat{a}^\dagger_{\omega_i} \exp\left[-i\,(k_i z - \omega_i t)\right] \right) \end{aligned} \tag{3.9}$$

We apply the expansion of the time evolution operator in the interaction picture to the initial quantum state $|0_s, 0_i\rangle$

$$|\Psi\rangle = |0_s, 0_i\rangle + \frac{1}{i\hbar} \int dt\, \hat{H}_I \, |0_s, 0_i\rangle + \frac{1}{2} \left(\frac{1}{i\hbar} \int dt\, \hat{H}_I \right)^2 |0_s, 0_i\rangle + \ldots$$

to obtain the generated quantum state $|\Psi\rangle$. We use the relation $\hat{a}_{\omega_{s,i}}|0_s, 0_i\rangle = 0$, and the Fourier transformation of the δ-function, and choose the limits of the z-integration to $[-L, 0]$. This leads to the single-pass photon state after the nonlinear medium

$$\begin{aligned}|\Psi\rangle = \quad & |0_s, 0_i\rangle \\ & + \eta \int d\omega_s\, d\omega_i\, \sqrt{\omega_s\, \omega_i}\; e^{-i\,\Delta k_{s,i}\,L/2}\; \mathrm{sinc}\left(\Delta k_{s,i}\,\frac{L}{2}\right)\, \delta(\Delta\omega)\; \hat{a}^\dagger_{\omega_s} \hat{a}^\dagger_{\omega_i}\; |0_s, 0_i\rangle \\ & + \frac{\eta^2}{2} \int d\omega_s\, d\omega_{s'}\, d\omega_i\, d\omega_{i'}\, \sqrt{\omega_s\, \omega_i\, \omega_{s'}\, \omega_{i'}}\; e^{-i\,\Delta k_{s,i}\,L/2}\; e^{-i\,\Delta k_{s',i'}\,L/2} \\ & \qquad \cdot \mathrm{sinc}\left(\Delta k_{s,i}\,\frac{L}{2}\right)\; \mathrm{sinc}\left(\Delta k_{s',i'}\,\frac{L}{2}\right)\, \delta(\Delta\omega)\; \delta(\Delta\omega')\; \hat{a}^\dagger_{\omega_s} \hat{a}^\dagger_{\omega_{s'}} \hat{a}^\dagger_{\omega_i} \hat{a}^\dagger_{\omega_{i'}}\; |0_s, 0_i\rangle \end{aligned} \tag{3.10}$$

where the constants are grouped in the parameter η, energy and quasi-phasematching

$$\Delta\omega = \omega_p - \omega_s - \omega_i \qquad \Delta k_{s,i} = k_p - k_s - k_i - \frac{2\pi}{\Lambda} \quad , \tag{3.11}$$

and renormalization of the state is neglected. The first and second order terms correspond to the single-, and double-photon-pair state.

The spectral envelope of the single-pair state is dominated by the sinc function with a width given by the difference of the group velocities of the three waves in the nonlinear material. For example a 2 cm long ppKTP crystal has a spectral width on the order of $\sim$ 200 GHz. To couple the generated photons to an atomic quantum memory with a bandwidth on the order of $\sim$ 10 MHz, spectral filtering by 4 orders of magnitude is necessary. A better way is to modify the spectral distribution of the vacuum field (*c.f.* equation 3.7) by an optical resonator which is described in the following.

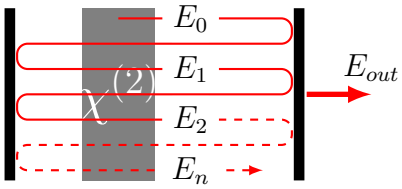

Figure 3.1.: Resonator model

The simple resonator depicted in figure 3.1 is assumed, consisting of two opposite mirrors that have fixed reflection, transmission, and loss, and a medium between

them with fixed loss [108]. The internally generated electric field E_0 overlaps with the remaining field after each round trip, and sums up to the total internal field $E_{int} = E_0 + E_1 + E_2 + \ldots + E_n$. After each round-trip the wave is damped due to absorption of the mirrors and the medium, scattering, and the designed transmission of the mirrors. The phase at the overlapping point is given by the path length of one round-trip and phase jumps at the surfaces of the components. We combine the loss, and the collected phase for one round-trip into the complex amplitude loss factor $h = |r|\, e^{i\,\Phi}$. The internal field[3] is then the geometric series $E_{int} = E_0(1+h+h^2+\ldots+h^n) = E_0/(1-h)$. With the loss factor h_0 that contains the transmission and the loss of the outcoupling mirror, we obtain the wave outside the resonator. The external field is then represented by $E_{out} = E_0 \cdot A(\omega)$ with the resonator modulation function $A(\omega) = h_0/(1-h)$. Relevant parameters for the description of optical resonators are the finesse $\mathcal{F} = \pi\sqrt{|r|}/(1-|r|)$, the free-spectral range $\omega_F = 2\pi\, c/L_{eff}$ (FSR) with the effective optical path length L_{eff} for one round trip and the speed of light c, and the linewidth $\delta\omega = \omega_F/\mathcal{F}$.

Applying the modulation function $A(\omega)$ to the vacuum fields of signal and idler leads to the spectral envelope $\Phi\,(\omega_s, \omega_i)$ of the generated single photon-pair state

$$\Phi\,(\omega_s, \omega_i) = A_s(\omega_s)\, A_i(\omega_i)\ \mathrm{sinc}\left(\Delta k_{s,i}\,\frac{L}{2}\right) \tag{3.12}$$

which is characterized by the parameters of the resonator: free-spectral range of signal $\omega_{F,s}$ and idler $\omega_{F,i}$, the finesse of signal $\mathcal{F}_s$ and idler $\mathcal{F}_i$, and the crystal properties: length L and phase-matching $\Delta k_{s,i}$. The resonant enhancement of generated photon pairs is now used to match the bandwidth of both generated photons to the transition bandwidth of the ion. The pump wavelength is therefore 427 nm, which corresponds to twice the transition frequency of $\omega_{854} \approx c/854\,\mathrm{nm}$. We now focus on the case when the FSR of signal and idler is equal $\omega_F = \omega_{F,s} = \omega_{F,i}$, and the longitudinal mode number $n = \omega_{854}/\omega_F$ is in resonance with the ion. The free spectral range of a macroscopic resonator, with a few centimeter length, is still smaller than the phase-matching bandwidth of the crystal. Therefore the comb structure is supported inside the phase-matching bandwidth, which is given by the sinc-function in 3.12. A signal photon generated in the i-th neighboring mode $n-i$ must have a partner in the $n+i$ due to energy conservation, and the narrowband pump. As an example, a resonator with $L_{eff} = 15\,\mathrm{cm}$ has a free-spectral range of 2 GHz and 100 modes would be enhanced in

[3] The intensity I inside the resonator is then given by $I = |E_{int}|^2 = \frac{|E_0|^2}{1+(2\,\mathcal{F}/\pi)^2\cdot\sin^2(\pi\,\omega/\omega_F)}$ with the definitions of the finesse $\mathcal{F}$ and the free-spectral range ω_F.

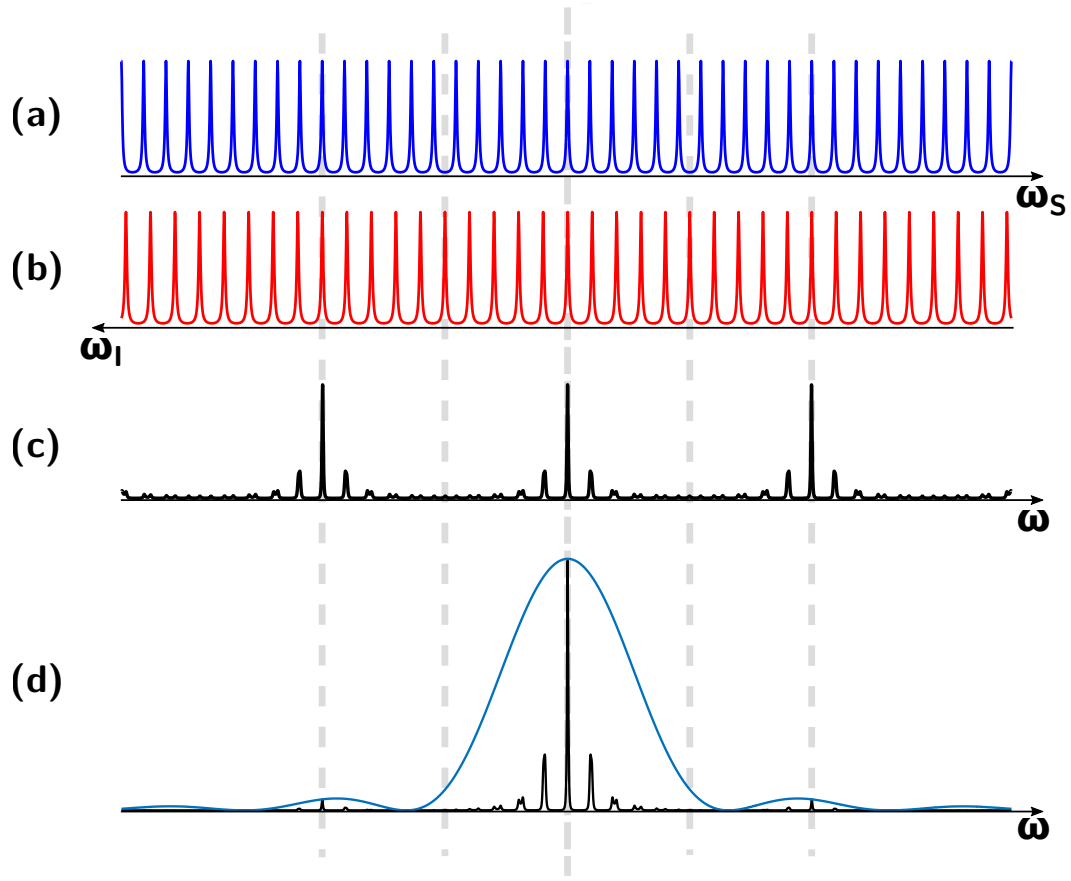

Figure 3.2.: Schematic model of the spectral envelope for the generated photons. (a) Resonator modulation function for the signal photon. (b) Resonator modulation function for the idler photon. (c) Combined two-photon modulation function. Due to energy conservation only clusters of modes are enhanced where both photons are resonant. (d) Combined two photon modulation with sinc-shaped spectral envelope of the SPDC process. When the pump frequency is set to $2\times$ the center frequency of (d), signal-idler pairs are generated either degenerate in the center mode or in two modes symmetrically displaced from the center.

the 200 GHz bandwidth of a 2 cm long ppKTP crystal. A scenario for two different FSRs, $\omega_{F,s} \neq \omega_{F,i}$ is depicted in 3.2. Here the mode $n_s = \omega_{854}/\omega_{F,s}$ for the signal photon and $n_i = \omega_{854}/\omega_{F,i}$ for the idler photon is resonant with the ion (*c.f.* 3.2 (a) and (b)). The i-th neighboring mode has therefore a mismatch of $i \cdot |\omega_{F,s} - \omega_{F,i}|$ which gets at some point larger than the linewidth of the modes. A resonant mode of the signal

photon has then a non-resonant mode of the idler photon due to energy conservation of the SPDC process. The generation of these pairs is therefore suppressed. This combined two-photon-modulation function is depicted in figure 3.2 (c). The result is the generation of photon pairs in a so called *cluster* of modes. The next cluster has then a distance of $\frac{\omega_F}{|\omega_{F,s}-\omega_{F,i}|} \cdot \omega_F$ with the mean free-spectral range ω_F. Together with the phase-matching bandwidth it is possible that only a single cluster is supported (*c.f.* figure 3.2 (d)), whereby the resonant enhancement of the ion resonant mode is (almost) not affected. The clustering is therefore a useful tool to suppress the generation of photons in non-ion-resonant modes, and acts like a spectral filter. For experiments where the signal photons are sent to an ion and the idler photons are used as heralds and therefore detected, it is necessary to filter out the resonant photon pairs on the detector side to suppress background. The clustering simplifies this spectral filtering, for example with a Fabry-Pérot filter, whereby a lower free-spectral range of the filter is required.

3.2. Signal to background ratio (SBR)

The time correlation of the generated photon pairs is typically measured as the cross correlation of the detection times of photons after splitting the signal and idler mode. Such measurements are used to characterize the photon pair source of this thesis, for example the entanglement in section 3.3.8 and 3.4. The probabilistic generation of the photon pairs and the spectral properties of a cw-pumped SPDC source lead to a overlap between different photon pairs which is described by the signal to background ratio (SBR). The scaling of the SBR and its influence on the entanglement is treated in the following.

In the cross correlation measurements, both photons will be detected with certain efficiencies η_1 and η_2. The probability to detect both photons of a pair – a coincidence – is then given by the product of the two efficiencies. The exponential cavity ring-down for the generated photons, with $1/e$ decay time τ for both photons, results in a double-sided exponential for the cross-correlation function. We specify now the number of coincidences C as the fraction of the photon wave-packet in the time bin Δt at a generated pair rate R_{pair} in the measurement time T:

$$C = \eta_1\eta_2 \ \left(1 - e^{-\Delta t/2\tau}\right) \ R_{pair} \ T \tag{3.13}$$

In a measured cross correlation shown schematically in figure 3.3, this value is read out as the number of events in the peak above the background B. It should be mentioned

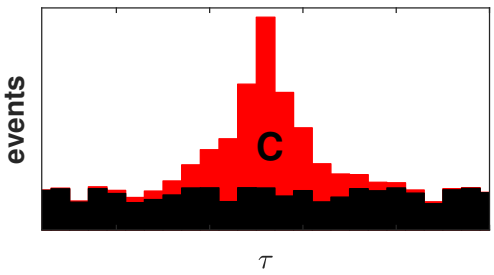

Figure 3.3.: Typical cross correlation function of the signal, and idler detection times with $\Delta t >> \tau$. The coincidences C (red) are visible as a peak on a background (black).

that a photon with exponential temporal shape requires an infinite time until the complete wave packet is observed. This is not possible in applications which means that a time bin will always be used.

The detected event rate $R_{Det,i}$ at each single-photon detector i has a contribution of the dark-count rate $R_{dc,i}$ of the detector, and is connected to the generated pair rate by

$$R_{Det,i} = R_{pair}\ \eta_i + R_{dc,i} \tag{3.14}$$

The individual efficiencies of the channels are obtained by dividing equation 3.13 by equation 3.14

$$\frac{C}{R_{Det,1}T} \approx \eta_2 \qquad \frac{C}{R_{Det,2}T} \approx \eta_1 \tag{3.15}$$

with the assumption of negligible dark-counts $R_{dc,i}\,T << C$ compared to the detected coincidences, and a chosen time bin to select a fraction of the wave-packet close to one. The calculated efficiencies and eq. 3.14 lead to the generated pair rate

$$R_{pair} \approx \frac{C}{\eta_1\ \eta_2} \tag{3.16}$$

To quantify the number of background events in a certain time bin, we make the assumption that the dark-count events in each detector, as well as the time between two subsequent generated pairs are random. This means that these do not show any correlation and lead to a symmetric triangular envelope[4] in the cross correlation. It starts at zero at the negative acquisition time of the measurement, gets its maximum at

[4]The triangular shape results from the finite length of the data set.

zero time difference and runs out to zero at a time difference of the positive acquisition time. If the time window of the correlation is small compared to the acquisition time and close to zero time delay, then the total number of background events is approximated by the maximum of this triangle. The total number of background events in this triangle is then given by the product of the number of detected events in both channels $N_{Det,i} = R_{Det,i}\,T$ corrected by the number of coincidences. The number background events B in a bin of size Δt is then

$$\begin{aligned} B &= (N_{Det,1} N_{Det,2} - C)\,\frac{\Delta t}{T} \\ &= R_{Det,1}\,R_{Det,2}\,\Delta t\,T - C\frac{\Delta t}{T} \\ &\approx \eta_1\,\eta_2\,R_{pair}^2\;\Delta t\,T \end{aligned} \tag{3.17}$$

approximated for low dark-count rates and large measurement times. Care must be taken when one arm is spectrally filtered. The photons in the unfiltered arm whose partners were filtered out act as an effective dark count rate.

We now obtain the signal to background ratio (SBR) with eq. 3.13 and 3.17

$$\mathrm{SBR} = \frac{C}{B} \approx \frac{1 - e^{-\Delta t/2\tau}}{R_{pair}\,\Delta t} \tag{3.18}$$

This value describes the certainty, that a detected coincidence is a detection of two photons that belong to the same photon pair. The relation between the detected coincidences C and the bin size Δt (*c.f.* equation 3.13) leads to a higher SBR for smaller bin size, at the cost of detected coincidences C, with the limit at small bin size

$$\lim_{\Delta t \to 0} \mathrm{SBR} = \lim_{\Delta t \to 0} \frac{1 - e^{-\Delta t/2\tau}}{R_{pair}\,\Delta t} = \frac{1}{2\,R_{pair}\,\tau} \tag{3.19}$$

The SBR is limited to 1 at a pair rate $R_{pair} = (2\,\tau)^{-1}$.

The dependence of the SBR on the generated pair rate R_{pair} describes the overlap of the photon pairs due to the exponential decay of the resonator, which is tunable via the pump power of the photon-pair source[5].

[5]It should be noted that the calculation of the SPDC quantum state (*c.f.* section 3.1) assumes that only the vacuum fields are present when a pair is generated. This assumption is not correct for large generated pair rates. In this situation stimulated generation of pairs becomes dominant, whereby the physical properties of the source change.

3.2.0.1. Influence of the SBR on the polarization entanglement

The photon pair source is used in section 3.4 to generate entangled photon pairs for quantum-network experiments. One can now ask about the fidelity that an unbiased observer would reconstruct when the scaling of signal and background, described by equations 3.13 and 3.17, is considered.

We therefore treat the photon pair source first as an idealized converter of a pump photon into an entangled two-photon state which has good overlap with the Bell state $|\Psi^-\rangle$ but is partially mixed. This corresponds to the case when the pump power is low and therefore also the generated pair rate R_{pair} is low. The partially mixing is due to imperfections of the setup and described by the small depolarization parameter ϵ in the initial density matrix

$$\rho_0 = (1-\epsilon)\,|\Psi^-\rangle\langle\Psi^-| + \epsilon\,\frac{\mathbb{1}}{4} \tag{3.20}$$

This is the state that the observer reconstructs when subtracting the whole background. We call the fidelity of this state *inferred fidelity*.

We choose now the HV-basis and ask for the number of events that an observer detects in correlation experiments with ρ_0 as the initial state. The probability P_{HH,ρ_0} to detect both photons with horizontal polarization, and P_{HV,ρ_0} to detect the first one with horizontal and the second one with vertical polarization is then given by

$$P_{HH,\rho_0} = \langle HH|\,\rho_0\,|HH\rangle = \frac{\epsilon}{4} \qquad P_{HV,\rho_0} = \langle HV|\,\rho_0\,|HV\rangle = \frac{1}{2} - \frac{\epsilon}{4} \tag{3.21}$$

The signal given by the number of coincidences C detected are detected with the aforementioned probabilities. We treat the background as uncorrelated events, which is valid when ϵ is small. These events are then detected with 25 % probability in each of the four possible combinations at a fixed measurement basis, in this case $\{HH, HV, VH, VV\}$. For the two measurement settings of 3.21 is the number of detected events E given by

$$E_{HH,\rho_0} = \frac{1}{4}\cdot B + \frac{\epsilon}{4}\cdot C \qquad E_{HV,\rho_0} = \frac{1}{4}\cdot B + \left(\frac{1}{2} - \frac{\epsilon}{4}\right)\cdot C \tag{3.22}$$

These events, and in general more basis combinations, are then used by an unbiased observer to reconstruct the density matrix. Because we assume only uncorrelated background as error source, the reconstructed state will also be a depolarized state of the form

$$\rho_{out} = (1-\Phi)\,|\Psi^-\rangle\langle\Psi^-| + \Phi\,\frac{\mathbb{1}}{4} \tag{3.23}$$

with the parameter Φ. The probabilities $P_{HH,\rho_{out}}$ and $P_{HV,\rho_{out}}$, and in general more combinations, that the observer calculates to reconstruct the density matrix ρ_{out} are given by

$$P_{HH,\rho_{out}} = \langle HH| \rho_{out} |HH\rangle = \frac{\Phi}{4} \qquad P_{HV,\rho_{out}} = \langle HV| \rho_{out} |HV\rangle = \frac{1}{2} - \frac{\Phi}{4} \tag{3.24}$$

Because the number of detected events are used to calculate these probabilities, the ratio of these events must be equal to the corresponding probabilities

$$\frac{E_{HV,\rho_0}}{E_{HH,\rho_0}} = \frac{P_{HV,\rho_{out}}}{P_{HH,\rho_{out}}} \tag{3.25}$$

which leads to

$$\Phi = \frac{1 + \epsilon \cdot \mathrm{SBR}}{1 + \mathrm{SBR}} \tag{3.26}$$

with the signal to background ratio described by equation 3.18. For a vanishing background, which means a large SBR, the value of Φ tends to: $\lim_{B\to 0} \Phi = \epsilon$, the inferred fidelity. The fidelity of this state reconstructed by the observer is then given by

$$\langle \Psi^-| \rho_{out} |\Psi^-\rangle = 1 - \frac{3}{4}\Phi \tag{3.27}$$

We use now the theoretical considerations to describe the dependence of the reconstructed fidelity on the pair rate of the entangled photon-pair source that is presented in section 3.4. It has a linewidth of $\sim 10\,\mathrm{MHz}$ which corresponds to an $1/e$ decay time of $\tau \approx 16\,\mathrm{ns}$. The resonator has an escape probability for a photon pair of $\eta_{esc} \approx (0.8)^2$, which limits the detected pair rate to the out-coupled pair rate $R_{out} = \eta_{esc} \cdot R_{pair}$.

Figure 3.4 shows the dependence of the reconstructed fidelity on the out-coupled pair rate R_{out}. Plotted is the theoretical limit (gray line) for the SBR (*c.f.* equation 3.19) with an inferred fidelity of 100 % ($\epsilon = 0$) and $\Delta t \to 0$, and the four scenarios: an inferred fidelity of 100 % ($\epsilon = 0$) and 98 % ($\epsilon = 0.027$) each for a time bin of $\Delta t = 2 \cdot \tau$, and $\Delta t = 6 \cdot \tau$ which correspond to 63 %, and 95 % collection of the wave packet. The steep drop in fidelity starts with a $R_{out} \approx 1 \times 10^5\,\mathrm{s}^{-1}$ and is close to 25 %, the complete mixture, at $R_{out} \approx 1 \times 10^8\,\mathrm{s}^{-1}$. This SBR is inherent with the cw-pumped SPDC source, and describes the amount of information that a independent observer will experience. The reconstructed fidelity is therefore a intrinsic limitation of the fidelity at a given generated pair rate.

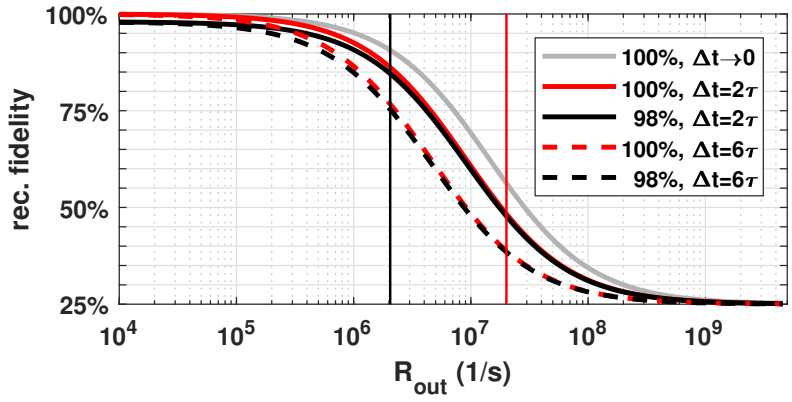

Figure 3.4.: Reconstructed fidelity in dependence of the pair rate behind the resonator $R_{out} = \eta_{esc} \cdot R_{pair}$. The $1/e$ decay time is chosen to $\tau \approx 16\,\text{ns}$, which corresponds to 10 MHz linewidth, and the photon pair escape probability to $\eta_{esc} = (0.8)^2$. Plotted is the theoretical limit (gray line) with an inferred fidelity of 100 % ($\epsilon = 0$) and $\Delta t \to 0$, and the four scenarios: inferred fidelity of 100 % (red lines) and 98 % (black lines), each for a binsize of $\Delta t = 2 \cdot \tau$ (solid), and $\Delta t = 6 \cdot \tau$ (dashed). The vertical lines denote the pair rates of the experiments of section 4.2 and 4.3.3 (black), and the pair rate when SBR = 1 (when $\Delta t \to 0$) (red).

3.3. Resonant photon-pair source

In this section the design and characterization of the photon-pair source is described. The aim is to generate orthogonal linear polarized photon pairs that are frequency degenerate at the atomic resonance with type-II conversion in a ppKTP crystal. The conversion is enhanced by a ring resonator that is resonant for both generated photons, and the clustering effect is used to generate only one cluster of a few modes to simplify spectral filtering. An additional compensation crystal inside the resonator is used, to be able to tune at the same time to double resonance for the two polarizations, and to the atomic resonance while attaining maximum conversion efficiency. The following section contains details on the design of the SPDC crystal (3.3.1), a characterization of the phase matching (3.3.2), and the resonator properties (3.3.3). The properties of the photon pairs are characterized with multi mode correlations of the generated cluster (3.3.4), and the spectral envelope of the cluster is measured (3.3.5). The single-mode photon-pair rate, and background contribution is measured (3.3.6), and the single mode operation is characterized with $g^{(2)}(\tau)$ measurements (3.3.7). Also the polarization entanglement by splitting the photons with a non-polarizing beam splitter of the photon-pair source is characterized (3.3.8).

3.3.1. Resonator design

We decided to use a four mirror ring resonator in bow-tie configuration around the ppKTP crystal, that is widely used for second harmonic generation (SHG), and SPDC sources (for example [93, 94, 96]). The main reason for this configuration is that losses are minimized, and the small angles of incidence of the beams on the mirrors induce only low astigmatism. The dimensions of the crystal[6] are 3.5 mm × 1 mm × 20 mm (y,z,x), and it has two 1 mm wide regions with different poling periods. The two chosen periods are designed such that optimal conversion should be possible at moderate temperatures (15 °C - 80 °C) even with a slight deviation in the fabrication process or a mismatch of the refractive indices that are used for the design. The poling periods were calculated to 14.575 µm, and 14.45 µm to fulfill phase matching at frequency degeneracy of signal and idler at $\sim$ 25 °C and $\sim$ 55 °C. The Sellmeier equations of [109] are used to model the thermo-optic properties of the KTP crystal.

An additional tunable birefringent element is placed inside the resonator that allows for separate tuning of the effective optical path length of the two generated

[6] fabricated by: Raicol Crystals Ltd.

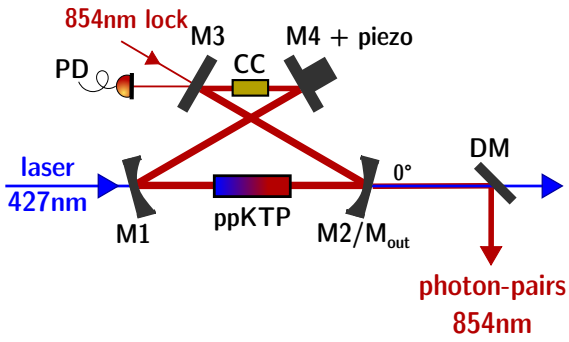

Figure 3.5.: Schematic of the four mirror bow-tie resonator. Inside the resonator is the ppKTP crystal, and a compensation crystal (CC) mounted. The 427 nm laser is coupled through mirror M1, the generated photons exit the resonator at mirror $M2/M_{out}$ under 0°, and are separated from the unconverted pump by a dichroic mirror (DM).

polarizations at the maximum conversion efficiency. Figure 3.5 shows a schematic of the resonator. It consists of two curved mirrors (M1, M2), and two flat mirrors (M3, M4). Mirror M1, M3, and M4 are coated with high reflectivity for 854 nm, M2 is used as the out-coupling mirror with 96 % reflectivity for 854 nm, which is discussed in the next section. All four mirrors are high transmissive coated for the pump wavelength at 427 nm. Attached to M4 is a piezo actuator[7] with a stroke of $\sim 44\,\mathrm{nm/V}$ for stabilizing the resonator length. The residual transmission ($< 1 \times 10^{-4}$) of the high reflective mirror M3 is used to stabilize the resonator-length. A phase modulated reference laser at 854 nm is used to generate the error signal with the Pound-Drever-Hall technique [79]. The angle of incidence of the beams onto the mirrors is chosen as 15°. The dimensions were chosen that on the one hand, commercially available mirror holders[8] could be used and the holders for the crystals have enough space without cutting the modes inside the resonator. On the other hand the free spectral range should be as large as possible, such that the effective optical path length should be as small as possible. It is clear that at this point a tradeoff had to be found. The distances were chosen as $|M1 - M2| = 69\,\mathrm{mm}$, $|M2 - M3| = |M4 - M1| = 57.2\,\mathrm{mm}$, and $|M3 - M4| = 30\,\mathrm{mm}$.

We considered two options for the compensation crystal. The first one uses a 10 mm

[7] Piezomechanik, HPSt 150/14-10/12 VS22
[8] M1,M2: Newport 9810-5-K ; M3: Newport 9871 (Tinymount) ; M4: Liop-Tec SR100-HS-100-3

long KTP crystal where the refractive index is tuned by temperature, and the second uses a 10 mm long Lithium Niobate crystal tuned by an external electric field.

A numerical simulation of the double resonance tuning is shown in figure 3.6. The bright spots are the combinations of the temperature respectively the applied voltage, and the relative position of the mirror M4, where double resonance at the atomic transition wavelength is reached. The main difference is that with thermo-optic tun-

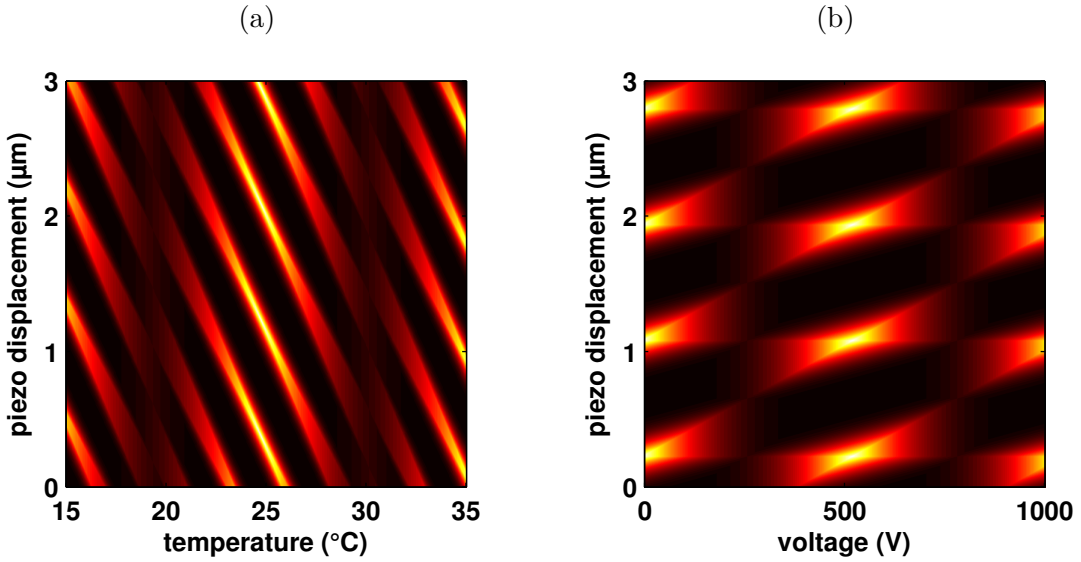

Figure 3.6.: Simulation of the double resonance tuning. The bright spots mark the combinations with double resonance. (a) Temperature tuning of a 10 mm long KTP crystal. (b) Elektro-optic tuning of a 10 mm long Litium Niobate crystal.

ing both polarizations are affected, and with electro-optic tuning only the polarization that points in the direction of the electric field. A sufficient range is 2 µm for the piezo displacement, 20 °C for the thermo-optic tuning, and 1000 V for the electro-optic tuning. We decided to use the thermo-optic tuning to avoid high voltage amplifiers in our setup, although the electro-optic tuning might be interesting in terms of fast switching of the resonance frequencies. This would enable one to switch the generated photons out of the atomic resonance which becomes necessary in atom-photon experiments.

The next step is the design of the spatial mode inside the resonator. Besides the necessary stability the focusing into the nonlinear crystal is crucial for the conversion efficiency. The Boyd-Kleinman theory [110] predicts an optimal focusing down to $\omega_{\mathrm{BK}} = 23\,\mu\mathrm{m}$ which is valid when all other effects are neglected. These side effects

such as gray-tracking and thermal lensing were studied for ppKTP in [111, 112] with the result that doubling the optimal waist ω_{BK} is sufficient that these effects become negligible. A simulation of the spatial mode inside the resonator is done with a standard ray matrix formalism for Gaussian beam propagation [108, 113]. Figure 3.7 shows a flattened illustration of the 1/e beam radius of the mode calculated in the sagittal and tangential plane for each polarization. The mirrors (M1,M2) are chosen

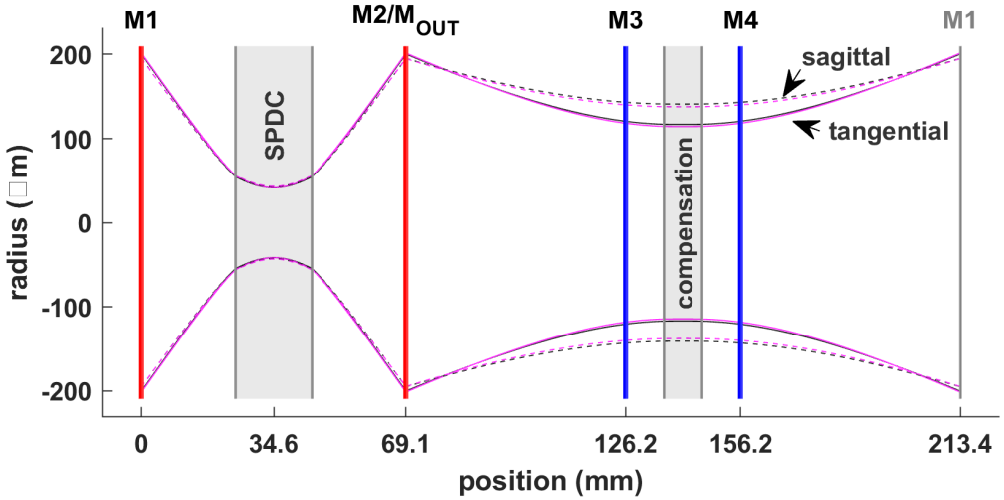

Figure 3.7.: Simulation of the beam propagation inside the resonator with the SPDC crystal, and the compensation crystal (rotated by 90°), for one round trip. Magenta colored lines correspond to horizontal polarization, black corresponds to vertical polarization.

with 50 mm radius of curvature. As a result we get a circular beam waist at the center of the ppKTP crystal of 42 µm, and a slightly elliptic beam waist in the center of the compensation crystal.

The remaining task is the choice of the output mirror reflectivity, which mainly determines the linewidth of the resonator. Besides the linewidth for optimal absorption we need a good photon-pair extraction efficiency, which is the square of the single-photon escape probability. The loss inside the resonator at 854 nm is mainly determined by the anti reflection coatings at the surfaces of the crystals. The manufacturer specified these to be lower than 0.5 % per surface. With a design reflectivity of M2 of 96 % we get a lower bound to the finesse of 100, a minimum escape probability per photon of 66 %, and an upper bound of the linewidth of 12 MHz.

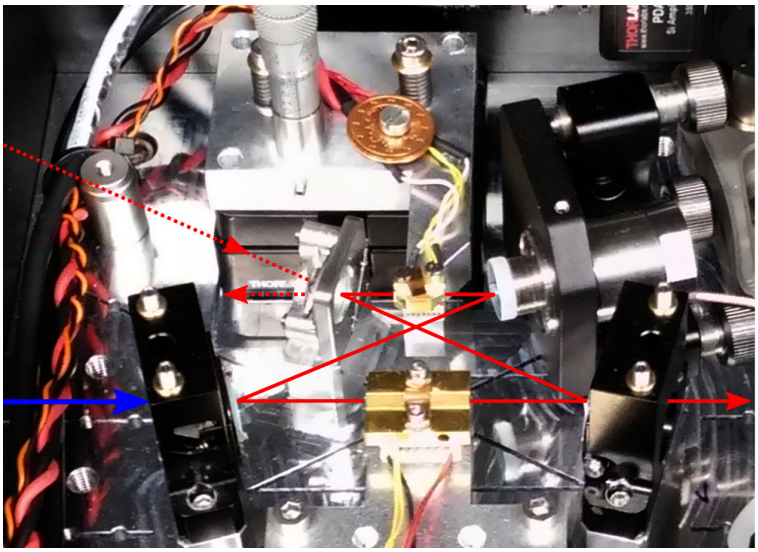

Figure 3.8.: Picture of the assembled resonator. The arrangement of the components is analogous to the schematic in figure 3.5.

Figure 3.8 shows a picture of the assembled resonator with the two crystal holders (gold coated). The red lines indicate the 854 nm beams, the blue arrow shows the direction of the pump. The holders were fabricated by our workshop. They are made of copper, and coated with gold to avoid oxidation. The crystal is lying in a groove, fixed by a spring from the top. The holders are attached via a Peltier element to a holder made of aluminum that is mounted to a five-axis translation stage[9] for independent positioning of the crystals. The baseplate is machined out of a solid aluminum block to ensure mechanical stability.

3.3.2. Phase-matching temperature of the crystal

The phase-matching temperature of the two poling sections (*c.f.* section 3.3.1) was measured by varying the temperature of the crystal and detecting the second-harmonic generated (SHG) 427 nm light of a single-pass 854 nm laser beam. The incoming beam was set to be diagonally polarized, and the beam was focused with a f=200 mm plano-convex lens. The crystal temperature was stabilized with a commercial temperature controller[10]. After passing the crystal , the unconverted light was split from the

[9]Thorlabs PY005/M
[10]ILX Lightwave, LDT-5412

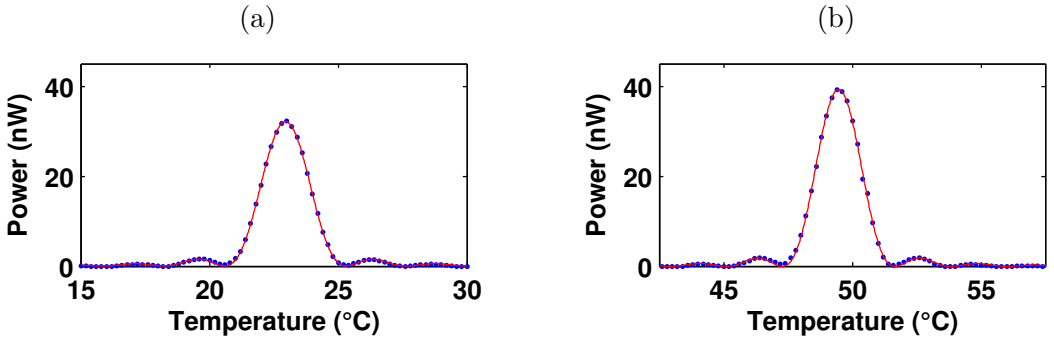

Figure 3.9.: Phase-matching temperature dependence: (a) Maximum at 22.954(2) °C measured on the 14.575 µm poling period with 3.7 mW 854 nm pump power. (b) Maximum at 49.468(3) °C measured on the 14.45 µm poling period with 4.4 mW 854 nm pump power.

converted light by two dichroic mirrors and a 427 nm bandpass filter. The 854 nm power was measured with a power meter[11], and the generated 427 nm power with a calibrated current mode PMT[12]. The temperature dependence of the SHG-power is shown in figure 3.9 for both poling periods. Optimal phase-matching is at 22.954(2) °C for the 14.575 µm poling-period section, and 49.468(3) °C for the 14.45 µm section. Both measured phase-matching temperatures differ by less than five degrees from the expected values. We use in the following the 14.575 µm period.

3.3.3. Resonator linewidth and escape probability

The resonator linewidth was measured with a frequency stabilized 854 nm laser. The beam was coupled via the high reflective mirror M3 (*c.f.* figure 3.5) that is later used for resonator length stabilization. The resonator length was scanned by applying a triangular voltage onto the piezo at mirror M4, and transmission at mirror M2 was measured with a photodiode. The laser was set to horizontal and vertical polarization in subsequent measurements. The compensation crystal temperature was set to non-degeneracy to be able to distinguish between the two polarizations. The scans are shown in figure 3.10. The fundamental spatial mode corresponds to the high peaks, higher spatial modes are also slightly visible. This is mainly the case because of the ellipticity of the mode at the mirror M3 (*c.f.* the beam profile in figure 3.7). We

[11] Thorlabs PM100D, S130C)
[12] Hamamatsu, H9307-04

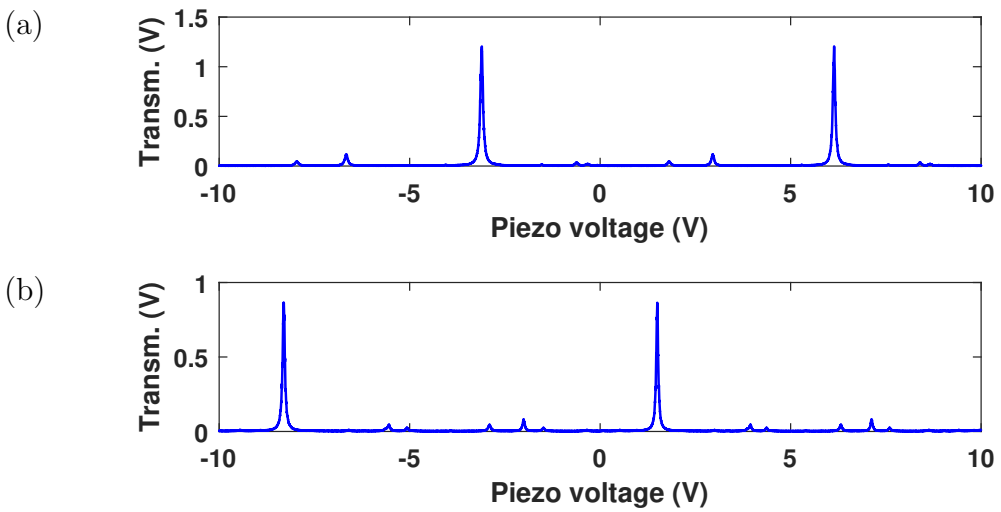

Figure 3.10.: (a) transmission of H-polarized light (b) transmission of V-polarized light

spent no effort on beam shaping of the locking beam. A linear behavior of the piezo in the low voltage range is assumed, and the calculated free spectral ranges (FSR) of the two polarizations were used to calibrate the abscissa. A fit to the intensity profile leads to the finesse $\mathcal{F}$, and the linewidth $\delta\omega$ of the resonator. A comparison of the measured out-coupling mirror (M2) reflectivity R_{out} with the finesse implies the internal losses L_{int}, and the escape probability, as the relation of transmitted power to the sum of lost power

$$\eta_{esc} = \frac{1 - R_{out}}{L_{\text{int}} + 1 - R_{out}}$$

Table 3.1 shows the summary of the measured properties. With the escape probability per photon we get a photon-pair extraction probability of 68 %.

Table 3.1.: Properties of the resonator for horizontal (H) and vertical (V) polarization.

pol.	FSR	R_{out}	$\mathcal{F}$	$\delta\omega$	L_{int}	η_{esc}
H	$2\pi \cdot 1.2661\,\text{GHz}$	95.77 %	121.2(1)	$2\pi \cdot 10.45(1)\,\text{MHz}$	0.82 %	83.7 %
V	$2\pi \cdot 1.2615\,\text{GHz}$	96.68 %	150.2(1)	$2\pi \cdot 8.40(1)\,\text{MHz}$	0.78 %	81.1 %

The modeled spectral envelope according to eq. 3.12 is plotted in figure 3.11 based on the measured linewidths, and the expected group-velocity difference of the conver-

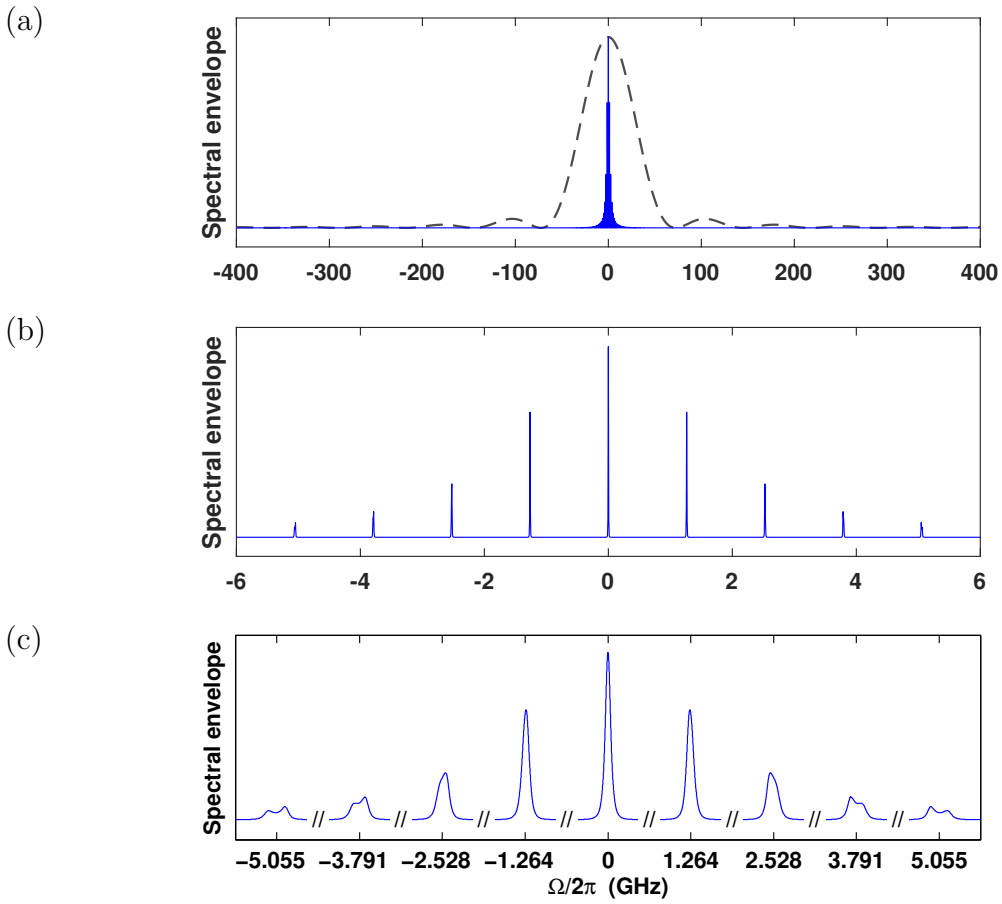

Figure 3.11.: Modeled spectral envelope of the generated photon pairs using the measured properties of the resonator: (a) overview, (b) zoom into central cluster, (c) zoom into the modes.

sion crystal. A ±400 GHz wide overview around frequency degeneracy of the photons is shown in figure 3.11(a). The gray dashed line is the spectral envelope without resonator, the blue structure in the middle is the main cluster. One can barely see the next neighboring clusters at about ±350 GHz. Their intensity is so small because the phase-matching of the crystal does not support them. Figure 3.11(b) shows a zoom into the central cluster. The modes are separated by the mean free-spectral range of ~ 1.26 GHz of the two polarizations. A zoom into the modes with discontinued abscissa is shown in 3.11(c). The modes spread into single peaks symmetrically

around frequency degeneracy. The ratio of the central frequency degenerate peak to the whole modeled intensity profile is 15.6 %. This means that one of 6.4 generated photons will be detected in the central mode.

3.3.4. Multi-mode photon pair correlation

The multi-mode two-photon cross correlation is a measurement that gives first information about spectral properties and pair rate of the generated photons. The resonator is stabilized onto the atomic reference, and the compensation crystal temperature is tuned to double resonance for the horizontally (H) and vertically (V) polarized photons. The generated photon-pairs are split by a polarizing beam splitter, coupled to a single mode fiber, and detected with single-photon detectors[13]. The detection pulses are then recorded by a time-tagging module[14]. Figure 3.12 shows

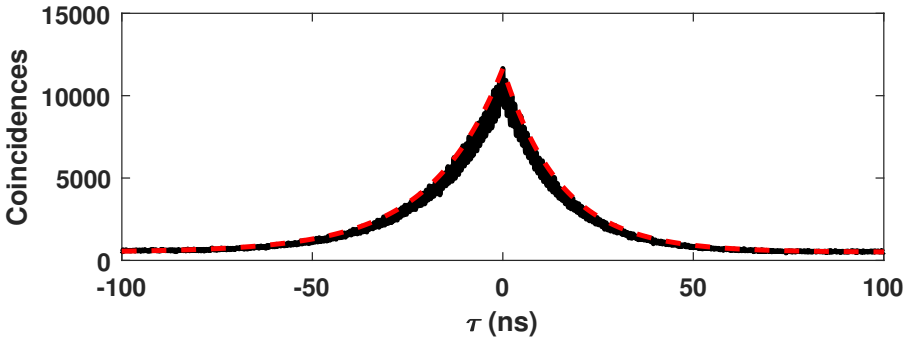

Figure 3.12.: Multi-mode photon pair correlation, τ is the delay between a vertically polarized photon and a horizontally polarized photon. Experimental data (black line) is measured with 840 µW pump power in 5 min with a binsize of 100 ps. The red curve is the expected envelope. The measured curve is smeared out at small $|\tau|$, due to a periodic oscillation caused by the resonator round trip time.

the calculated correlation function (black line) for a pump power of 840 µW in 5 min integration time and 100 ps binsize. The measured curve is smeared out at small $|\tau|$, due to a periodic oscillation caused by the resonator round trip time, which is investigated with higher time resolution later in this section. The dashed line is a double sided exponential [99]

$$\mathrm{G}^{(1,1)}_{H,V}(\tau) = C\,\left(\Theta(\tau)\,e^{-\delta\omega_H\,\tau} + \Theta(-\tau)\,e^{\delta\omega_V\,\tau}\right) + B \tag{3.28}$$

where C is a proportionality constant, $\Theta(\tau)$ is the Heaviside step function, and B is the background per bin. The measured linewidths (*c.f.* section 3.1) $\delta\omega_H$ ($\delta\omega_V$) are

[13]Perkin Elmer, SPCM-AQR-FC
[14]Picoquant, PicoHarp 300

used for the horizontal (vertical) polarization at $\tau > 0$ ($\tau < 0$). The measured rates are $R_H = 1.11 \times 10^5\,\mathrm{s}^{-1}$, and $R_V = 1.26 \times 10^5\,\mathrm{s}^{-1}$. The background-corrected coincidence rate is extracted as $C = 1.13 \times 10^4\,\mathrm{s}^{-1}$, and the background rate as $1.67\,\mathrm{s}^{-1}$. The total detection efficiencies are determined to be $\eta_H = 9\,\%$, and $\eta_V = 10.2\,\%$, and the generated pair rate is $R_{pair} = 1.5 \times 10^6\,\mathrm{s}^{-1}$ inside the cavity (*c.f.* equations 3.15, 3.16). As a result we get a signal to background ratio (SBR) of 6766, which matches the theoretical SBR (*c.f.* equation 3.18) of 6711 when only lost-partner events are taken into account for the background. Detector dark counts play no significant role. The modulation that becomes visible in the zoom shown in figure 3.13(a) is due to the

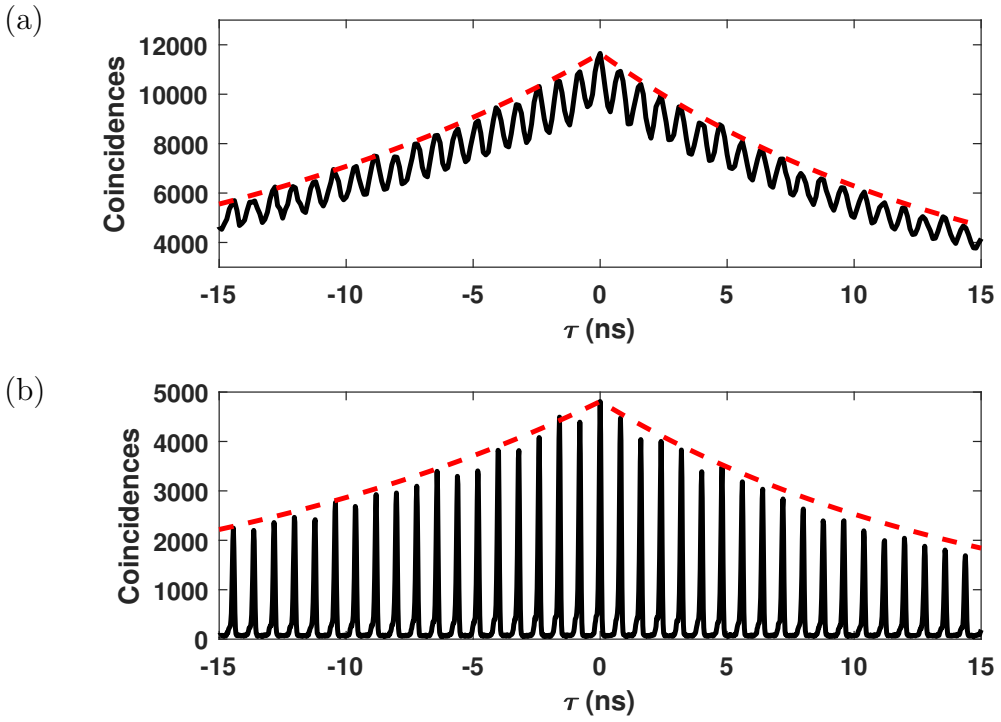

Figure 3.13.: Zoom into the multi-mode photon pair correlation, which reveals the resonator round-trip time in the periodicity. Shown are the experimental data (black line) and predicted envelope (red line). (a) Zoom into figure 3.12, measured with silicon APD's. (b) High-time-resolution measurement with superconducting single-photon detectors (SSPD).

cluster of frequency modes and the timing resolution of the used detector. The periodicity corresponds to the 791 ps round-trip time of the photons inside the resonator. A high-time-resolution measurement is shown in figure 3.13(b), recorded with supercon-

ducting single-photon detectors (SSPD)[15] with a time resolution of 55 ps. The binsize was chosen to 20 ps. The detectors are located in the laboratory of Christoph Becher, and connected via ∼ 90 m of multi-mode fiber. The data was recorded with 2 mW of 427 nm pump power in 62.5 min integration time. The longer integration time was required due to the high losses in the used fibers and the low detection efficiencies at this wavelength. The peaks have a width of 90 ps which is a convolution of the detector timing resolution, and the time uncertainty of the generated photons, which is given by the spectral envelope of the cluster. The red dashed line is the expected temporal envelope.

3.3.5. Spectrally-resolved cluster

The spectrum of the generated photon pairs was directly measured by the use of a tunable narrow-band filter in the horizontally polarized arm as depicted in figure 3.14. The spectral filter is a Fabry-Pérot interferometer (FPI) made of a plano-

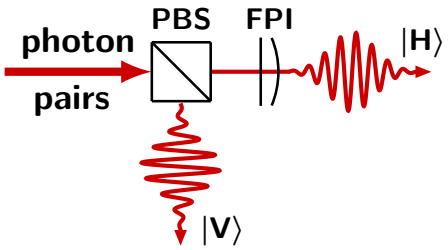

Figure 3.14.: Setup to spectrally resolve the cluster of modes with a tunable FPI.

convex lens of BK7 glass, coated from both sides with R= 99.35 % reflectivity, and temperature stabilized following the example presented in [114, 115]. The linewidth is $\delta\omega = 2\pi \cdot 111.7$ MHz, and the free spectral range FSR= $2\pi \cdot 53.956$ GHz. The resonator is temperature-tunable by 17.85 K/FSR and stabilized to 1 mK (corresponding to 3 MHz). The filter resonance was shifted for each data point by $2\pi \cdot 15.1$ MHz (5 mK temperature step) over $\pm 2\pi \cdot 10$ GHz. The signal was integrated for 10 s at each frequency. A waiting time of 30 s was used after each temperature change for the filter temperature stabilization. The result is shown in figure 3.15. Plot (a) shows the rate of filtered horizontally-polarized photons and (b) the detected coincidences between the horizontally and vertically polarized photons. The observed signal is a convolution

[15]Single Quantum, EOS X10

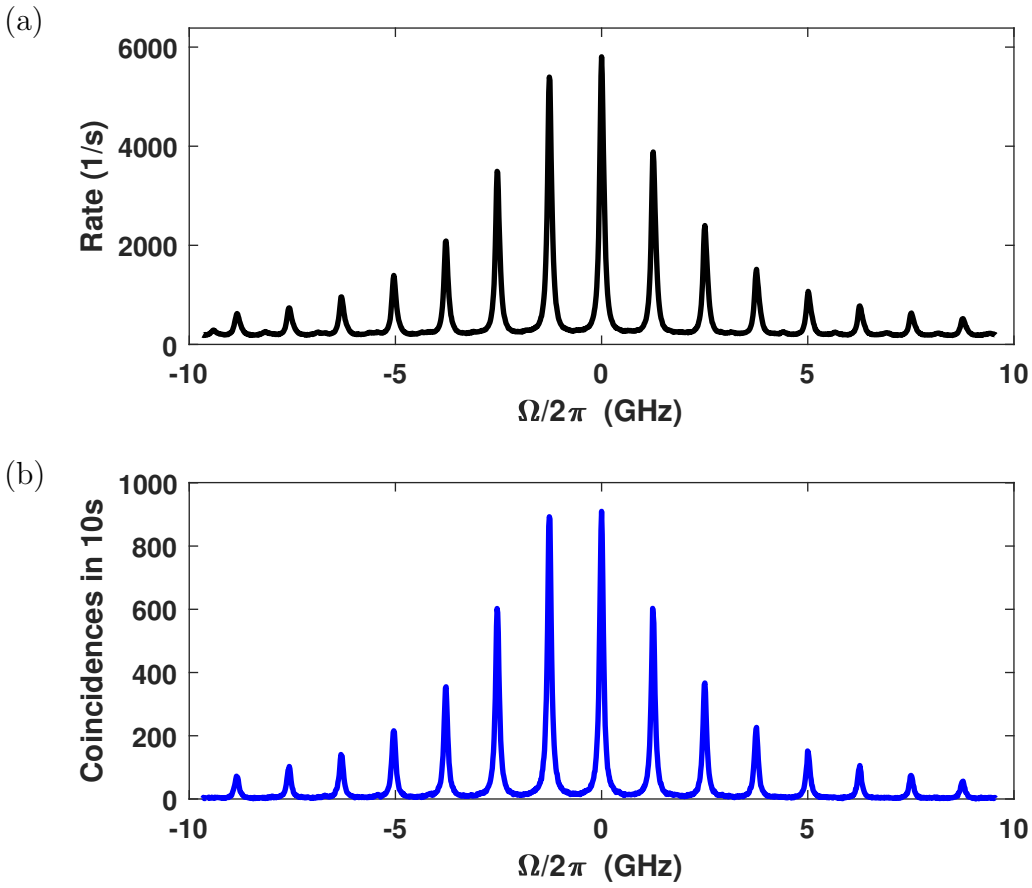

Figure 3.15.: Frequency scan of the generated photons of the central cluster of modes. (a) Rate of the horizontally polarized (filtered) photons. (b) Detected coincidences with the unfiltered vertically polarized partner photons.

of the spectral filter transmission and the spectral envelope of the generated photons. As a consequence we see that the width of the peaks is mainly given by the linewidth of the FPI. The offset in the rate (figure 3.15(a)) corresponds to the dark-count rate of the detector of $180\,\mathrm{s}^{-1}$. The free spectral range of both curves also matches the prediction in figure 3.11. The predicted ratio of the central peak to the whole spectrum is 15.6 %. By taking the sum of detected coincidences in the central peak and divide it by the sum of all detected coincidences we get a ratio of 17.5 %. A contribution to the deviation of this ratio to the modeled value is that only a finite number of side modes is used for the calculation. It is also notable that the central peak is not the highest. Three reasons could be behind this. The first is that the resonator was not perfectly

tuned to double resonance for signal and idler at frequency degeneracy. For example when the resonator of the signal photons is resonant to two times the pump frequency and the resonance of the idler photon is shifted by a fraction of the difference in free spectral range of the two. If the shift is half of this difference, in our case $\sim 2.3\,\mathrm{MHz}$, then due to energy conservation of the SPDC process there will be two modes at the center with equal enhancement. The second is a 427 nm pump power drift during the $\sim 25\,\mathrm{h}$ lasting measurement and the third is a temperature drift of the FPI-filter due to the electronics.

3.3.6. Single-mode photon pair correlations

Single frequency mode operation of the pair source is achieved by tuning the FPI to resonance with the central mode. The temporal correlation of the recorded detection times reduces to the double sided exponential of equation 3.28, and no modulation is visible. Such a correlation is shown in figure 3.16. The 427 nm pump power was set to 1.16 mW, and the acquisition time was 9 min. The horizontally polarized (transmitted) photons are filtered and used as start signal for the correlation. The red curve is a fit to the data with $1/e$-times of $18.4(1)\,\mathrm{ns}$ for $\tau < 0$ and $14.8(1)\,\mathrm{ns}$ for $\tau > 0$.

The expected $1/e$-times from the calibration measurements are $1/(2\pi \times 8.4\,\mathrm{MHz}) = 18.9\,\mathrm{ns}$ for $\tau < 0$ and $(1/(2\pi \times 10.4\,\mathrm{MHz}) + 1/(2\pi \times 111.7\,\mathrm{MHz})) = 16.7\,\mathrm{ns}$ for $\tau > 0$, which is the convolution of the resonator and the FPI $1/e$-time used in this arm. We realigned the resonator twice between the calibration measurements and this measurement. By changing the position of the crystals, the loss inside the resonator slightly changes, and as a consequence the linewidth of the photons become slightly different.

This measurement was repeated for different 427 nm-pump powers to extract the pair rate per pump power and to verify the theoretical model for the signal to background ratio (SBR) of section 3.2. The number of coincidences is extracted from the data by the sum of all events in a correlation window of $\pm 400\,\mathrm{ns}$ with subtracted background, which corresponds to $> 99.999\,\%$ of the photon wave packet. The background per bin is determined by the mean value of the offset at large times, compared to the photon wave-packet, the total background is then calculated by the background per bin multiplied with the number of bins. Figure 3.17(a) shows the detected coincidence rate R_C (left ordinate axis), and the inferred out-coupled pair rate R_{out} directly after the out-coupling mirror (right axis). The procedure to infer this value is explained in the following. A linear fit to the detected coincidences (*c.f.* figure 3.17(a)), and the

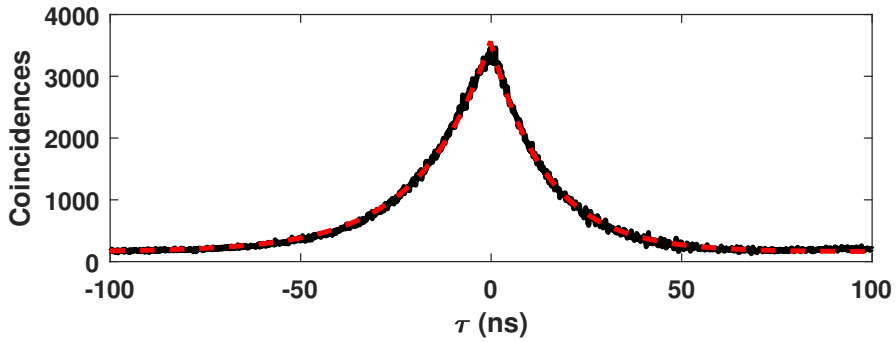

Figure 3.16.: Single mode correlation (black line), by filtering the horizontally polarized photons with the FPI. The red line is a fit to the data with a double-sided exponential which reveals the $1/e$ decay times of the resonator. There is no oscillation visible in the data (*c.f.* section 3.3.4), which is a clear sign of single-mode operation.

rates of the two detector arms (not shown) results in the rates per pump power, in their slopes:

- Coincidence rate: $R_C = 1490(22)/(\mathrm{s\,mW})$
- Rate of horizontally polarized channel (filtered): $R_H = 7.75(8) \times 10^3/(\mathrm{s\,mW})$
- Rate of vertically polarized channel (unfiltered): $R_V = 1.61(2) \times 10^5/(\mathrm{s\,mW})$

The measured rates R_H (R_V) of the horizontally-(vertically-)polarized arms and the rate of detected coincidences R_C are used to infer the generated multi-mode pair rate of $R_{MM,pair} = 9.97(15) \times 10^5/(\mathrm{s\,mW})$ inside the crystal according to equations 3.15 and 3.16 and a correction of the measurement time due to the chopper duty cycle of 83.3 % which is used for stabilizing the resonator. The spectral filter acts like loss in this arm, therefore the division of the R_C by R_H (R_V) leads to the multi-mode efficiencies $\eta_{MM,H} = 0.91\,\%$ ($\eta_{MM,V} = 19.8\,\%$). The generated single-mode pair rate of $R_{SM,pair} = 1.56(3) \times 10^5/(\mathrm{s\,mW})$ inside the crystal is obtained by multiplying $R_{MM,pair}$ with the spectral intensity ratio of the central mode to the full spectrum 15.6 % (*c.f.* section 3.3.3). The available single-mode pair rate $R_{out} = 88(1) \times 10^3/(\mathrm{s\,mW})$, which is the single-mode pair rate outside the resonator including the optical chopper, is then the product of $R_{SM,pair}$ with the two resonator escape probabilities (*c.f.* table 3.1) and the chopper duty cycle.

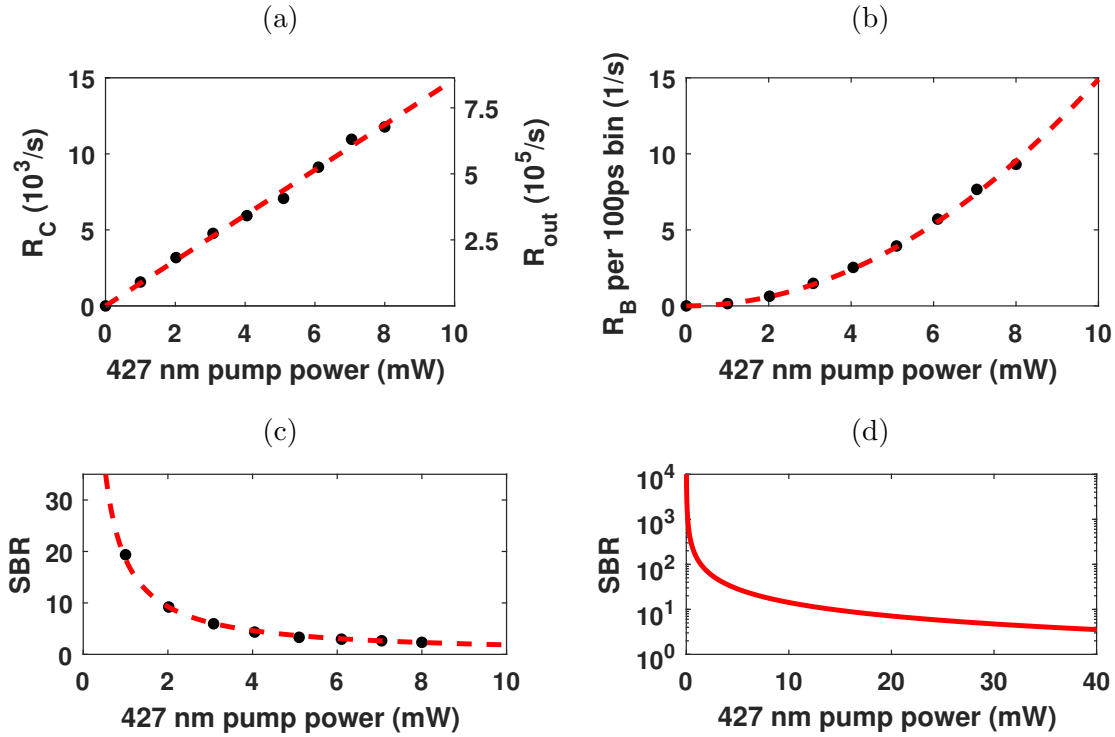

Figure 3.17.: (a) Pair rate in dependence of the 427 nm pump power P_{427}. Left axis: detected pair rate. Right axis: inferred out-coupled pair rate. The red line is a linear fit ($R_C = a \cdot P_{427}$) to the measured values whith the slope 1490(22)/(s mW). (b) Detected background in a 100 ps bin. The red line is a prediction from the model $R_B = \eta_{MM,H}\,\eta_{MM,V}\,\Delta t\,R^2_{MM,pair}\cdot P^2_{427} = 0.149\,/(\mathrm{s(mW)^2})\cdot P^2_{427}$. (c) Measured signal-to-background ratio (SBR) with only one arm filtered. The red line is the prediction from the model. (d) Predicted SBR when both arms are filtered.

The detected background rate R_B in a bin of size $\Delta t = 100$ ps is plotted in figure 3.17(b), the red line is the predicted behavior starting with the multi-mode pair rate, the extracted efficiencies, and equation 3.17.

Figure 3.17(c) shows the comparison of the measured signal to background ratio (SBR), with the predicted curve (red line), when only one arm is spectrally filtered. The SBR is calculated for a time window of $\pm 1 \cdot \tau$ of the double sided exponential. The accidental coincidences are the dominant background source as shown by the good overlap of prediction and measurement. Figure 3.17(d) shows the predicted SBR when both arms are spectrally filtered.

3.3.7. Single mode $g^{(2)}(\tau)$

A sensitive proof of single-mode operation is the second-order auto-correlation function of a single arm. The setup is depicted in figure 3.18 the relevant part for this measurement is the 50:50 beam splitter (BS) with the two detectors in one arm of signal and idler that form an Hanbury-Brown-Twiss setup. The other optical components are used to overcome technical problems that are discussed in the following. This measurement is sensitive to the two-photon and in general multiple-photon events

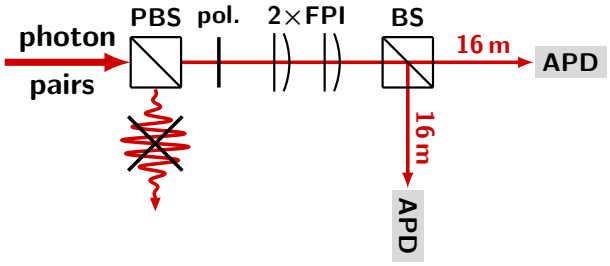

Figure 3.18.: Setup to measure the second-order correlation function $g^{(2)}(\tau)$.

of the SPDC state of equation 3.10. We therefore need to split the generated pairs with an extinction ratio that is better than the ratio of single pairs to multiple pairs. Otherwise there will leak signal-idler pairs to the detectors which cause a strong peak at zero time delay and the cross correlation of signal and idler would dominate the measurement. It turned out during the experiments that this was not possible at the central mode of the cluster. The signal-idler correlation was always leaking and the double sided exponential, like in figure 3.16, dominated the data. This means, that the splitting ratio of signal and idler at the polarizing beam splitter (PBS) is not high enough. The prerequisites to achieve high splitting ratio at the PBS are: the polarization of the signal and idler pairs must be linear orthogonal polarized and aligned with the PBS, and the PBS must have a high extinction ratio. The alignment of the polarization was carefully done in the experiment, and the extinction ratio of the PBS is specified to $< 10^{-3}$. To achieve higher splitting ratio we record the data for the neighboring modes of the cluster: these are not frequency-degenerate because of the energy conservation of the SPDC process and the narrowband pump laser and we use additional spectral filtering. The frequency splitting of the first neighboring modes is twice the FSR of the resonator, $\sim 2\,\mathrm{GHz}$.

Two consecutive filtering cavities, with 50 MHz, and 112 MHz linewidth, are used

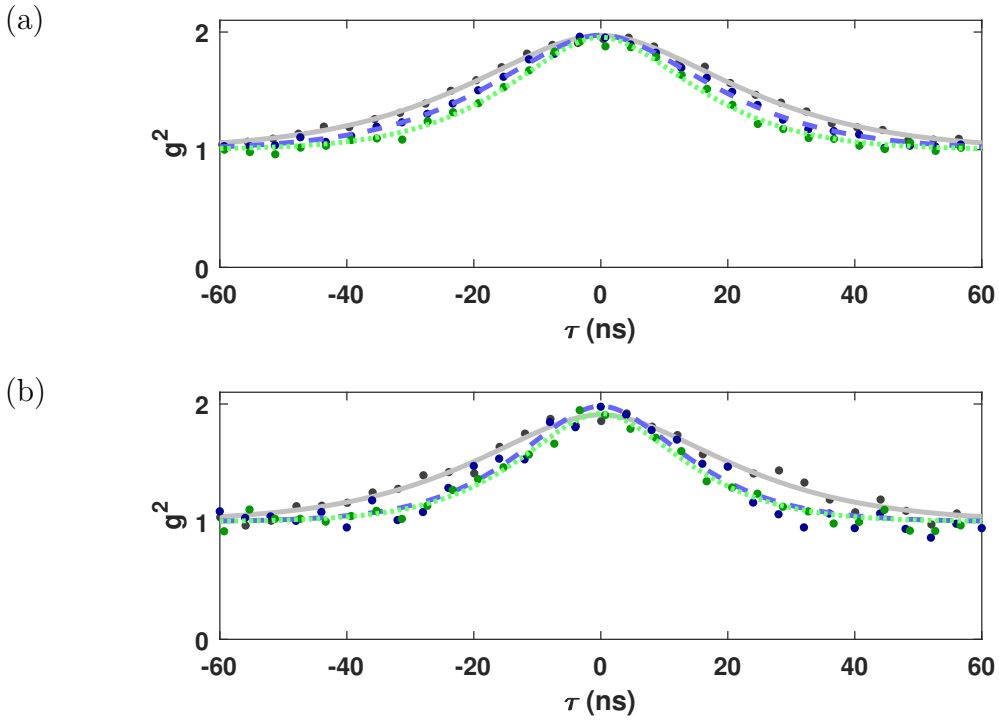

Figure 3.19.: $g^{(2)}(\tau)$ measurement for three side modes: (a) horizontally polarized photons, (b) vertically polarized photons. 1th side mode: grey dots (fit: solid grey line). 2nd side mode: blue dots (fit: dashed blue line). 3rd side mode: green dots (fit: dotted green line).

with an extinction ratio of $< 10^{-6}$ (together) to the partner photon at the first neighboring mode of the cluster. Additional to the PBS ($< 10^{-3}$), we add a linear polarizer[16] ($< 10^{-7}$). As Hanbury-Brown-Twiss setup we use a 50:50 fiber beam splitter, and a 16 m ($\sim$ 80 ns) delay fiber at each output before the detector. These delay fibers turned out to be necessary because of the optical after-pulsing of the detectors that is back-reflected by the optics in front of the 50:50-beam splitter, and afterwards detected by the other detector. The additional delay separates these pulses by $\sim 2 \times 80$ ns from the point of interest. Figure 3.19 shows the measured data for

[16]Thorlabs: LPNIR050

Table 3.2.: Summarized results of the $g^{(2)}(\tau)$ measurement for the first three side modes of horizontally- and vertically polarized photons.

	acquisition time	linewidth	$g^{(2)}(\tau = 0)$
H-pol: 1. side mode	1 h 11 min	$2\pi \times 14.5(1)$ MHz	1.971(8)
H-pol: 2. side mode	2 h 57 min	$2\pi \times 17.4(3)$ MHz	1.97(1)
H-pol: 3. side mode	9 h 35 min	$2\pi \times 20.7(4)$ MHz	1.96(1)
V-pol: 1. side mode	6 h 44 min	$2\pi \times 15.3(4)$ MHz	1.91(2)
V-pol: 2. side mode	4 h 41 min	$2\pi \times 22.5(11)$ MHz	1.98(4)
V-pol: 3. side mode	13 h 33 min	$2\pi \times 23.2(9)$ MHz	1.92(3)

the first three neighboring modes for horizontal, and vertical polarized photons. The curves are not corrected for background. The dashed lines are fits with the second order correlation function [99]

$$\mathrm{g}^{(2)}(\tau) = 1 + |\,\mathrm{g}^{(1)}(\tau)|^2 \tag{3.29}$$

and the normalized first order correlation function $\mathrm{g}^{(1)}(\tau)$

$$\mathrm{g}^{(1)}(\tau) = \; e^{-\frac{\delta\omega}{2}|\tau|}\left(1 + \frac{\delta\omega}{2}\,|\tau|\right) \tag{3.30}$$

with the assumption of equal linewidths $\delta\omega = \delta\omega_s = \delta\omega_i$. The results of the $g^{(2)}(\tau)$ measurement for the horizontally polarized photons are summarized in table 3.2. The value of $g^{(2)}(\tau = 0) \approx 2$ for all the measurements is a clear sign of single mode operation of the SPDC source with thermal statistics. The scaling with the number of modes N is $g^{(2)}(\tau = 0) = 1 + 1/N$ in multi-mode operation [99, 116]. In addition, the curves become narrower as we go away from the central mode. This corresponds to the spectral broadening shown in the modeled spectrum in figure 3.11, where the cavity modes for signal, and idler photons do not perfectly overlap, and as a resulting spectral envelope, the product gets broader.

3.3.8. Resonant photon-pair source: Polarization entanglement

The two-photon state with orthogonal linear polarizations is now used to generate polarization entanglement by splitting the photons with a non-polarizing 50:50 beam splitter. The FPI is used behind the beam splitter (BS) in one arm to obtain single-frequency-mode operation. The 50:50 beam splitter is described by the unitary operator $\hat{\mathrm{S}} = \exp(\frac{\pi}{4}\,(\hat{a}_A^\dagger\,\hat{a}_B - \hat{a}_A\,\hat{a}_B^\dagger))$ [117], for one photon at input A and zero photons at input B we get at the output

$$\hat{\mathrm{S}}\;|1_A, 0_B\rangle = \frac{1}{\sqrt{2}}\,|1_{A'}, 0_{B'}\rangle + \frac{i}{\sqrt{2}}\,|0_{A'}, 1_{B'}\rangle$$

When two photons with different polarizations are entering on the same port we get

$$\begin{aligned}\hat{\mathrm{S}}_H \otimes \hat{\mathrm{S}}_V\;\; |1_A, 0_B\rangle_H\,|1_A, 0_B\rangle_V = \frac{1}{2}\Big(\,&|1_{A'}, 0_{B'}\rangle_H\,|1_{A'}, 0_{B'}\rangle_V + |0_{A'}, 1_{B'}\rangle_H\,|0_{A'}, 1_{B'}\rangle_V\,\Big)\\ + \frac{i}{2}\underbrace{\Big(\,|1_{A'}, 0_{B'}\rangle_H\,|0_{A'}, 1_{B'}\rangle_V + |0_{A'}, 1_{B'}\rangle_H\,|1_{A'}, 0_{B'}\rangle_V\,\Big)}_{\rightsquigarrow|\Psi^+\rangle}\end{aligned}$$

Coincident detections at both detectors – that means one photon in arm A and one photon in arm B – project this state onto the maximal entangled $|\Psi^+\rangle$ state. The splitting happens in 50 % of the cases which effectively lowers the efficiency and increases the background. To verify the entanglement, a set of half-waveplate and linear polarizer is used at each output of the BS, in front of the detector. The waveplate of the reflected arm is set to a fixed linear polarization, and the coinciding detections in dependence of the angle of the half-waveplate axis are recorded. The resulting fringes are plotted in figure 3.21. An acquisition time of 10 s for each point, a step-size of 3°, and a 427 nm pump power of 6.7 mW were used. The projection of the transmitted arm was set to horizontal (H, green), diagonal (D, red), vertical (V, blue) and anti-diagonal (A, black). The data is fitted with a cosine function to extract phase-offset and visibility of the fringes , the values are summarized in table 3.3. The data is corrected for background originating from lost-partner events, detector dark counts, and not-splitted photon-pairs. We subtract an additional phase-offset of 2.8° due to imperfect calibration of the half-waveplate, and get the summarized values of table 3.3. The mean visibility of 96.9 % and the phase increasing in 22.5° steps are clear signs of entanglement. A reason for the different amplitudes is probably a residual wedge-angle of the used waveplate in the transmitted arm, which causes a spatial shift, and as a result a lower coupling efficiency into the single mode fiber. Another possibility is a pump power drift during the measurement.

Figure 3.20.

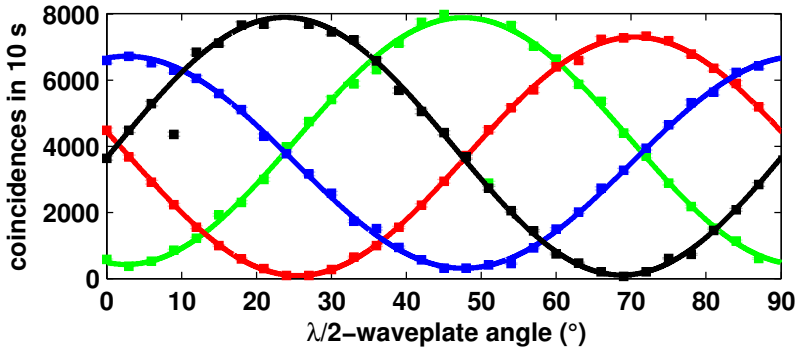

Figure 3.21.: Polarization correlation measurement. The projection of one arm is fixed: horizontal (H, green), diagonal (D, red), vertical (V, blue) and anti-diagonal (A, black). The other arm is projected on different linear polarizations. The data is fitted with a cosine function to extract the phase-offset, and the visibility of the fringes.

Table 3.3.: Phase, and visibility of the polarization correlation measurement.

fixed projector setting:	H	D	V	A
phase (°)	−0.1(1)	22.8(1)	44.9(1)	66.0(1)
visibility	94.6(4) %	98.8(2) %	95.4(3) %	98.7(3) %

A full tomography of the two photon density matrix was performed via measurements in 16 different basis combinations and a maximum-likelihood calculation following the procedure of [118]. The first dataset was measured with 200 µW of 427 nm pump power. The coincidences are recorded for each basis combination for 1 min. The number of coincidences is extracted from the data by the sum of all events in a correlation window of ±180 ns with subtracted background, which corresponds to $> 99.99\,\%$ of the photon wave packet. The background per bin is determined by the mean value of the offset at large times, compared to the photon wave-packet, the total background is then calculated by the background per bin multiplied with the number of bins. The reconstructed density matrix represented in the $\{|H,H\rangle,\ |H,V\rangle,\ |V,H\rangle,\ |V,V\rangle\}$ ba-

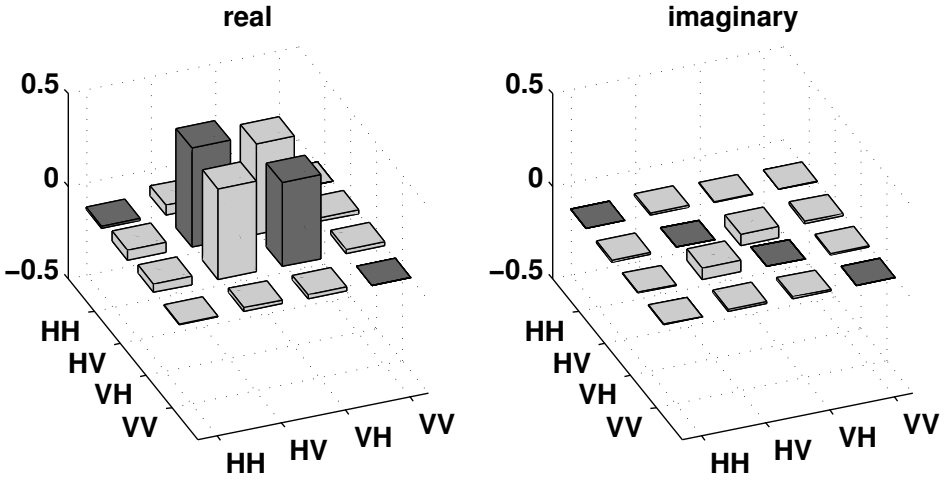

$$\begin{pmatrix} 0.01 & 0.05 & 0.05 & 0.00 \\ 0.05 & 0.54 & 0.49 & 0.02 \\ 0.05 & 0.49 & 0.45 & 0.02 \\ 0.00 & 0.02 & 0.02 & 0.00 \end{pmatrix} \qquad \begin{pmatrix} 0.00 & 0.01 & 0.00 & -0.00 \\ -0.01 & 0.00 & -0.06 & -0.01 \\ -0.00 & 0.06 & 0.00 & -0.01 \\ 0.00 & 0.01 & 0.01 & 0.00 \end{pmatrix}$$

Figure 3.22.: Reconstructed two-photon density matrix at 200 µW of 427 nm pump power.

sis is shown in figure 3.22. A fidelity with the maximal entangled $|\Psi^+\rangle$ state of 98.2 %, a purity of $\mathrm{tr}(\hat{\rho}^2) = 98.7\,\%$, and a concurrence $\mathrm{C} = 0.971$ are calculated from the reconstructed density matrix [119].

The second set was measured at 10 mW pump power and 10 s integration time for each basis combination. The reconstructed density matrix is shown in figure 3.23. A fidelity of 89.7 %, a purity of $\mathrm{tr}(\hat{\rho}^2) = 81.9\,\%$, and a concurrence of $\mathrm{C} = 0.805$ is reconstructed.

It is not fully understood why we do not get a perfect pure $|\Psi^+\rangle$-state even at low power, and why it gets even worse at higher pump power. The pure $|\Psi^+\rangle$-state would need totally indistinguishable photons. Their difference in linewidth of $\delta\omega_H = 2\pi \cdot 10.45(1)\,\mathrm{MHz}$, and $\delta\omega_V = 2\pi \cdot 8.40(1)\,\mathrm{MHz}$ induces a discriminability. This is easier to understand in the time domain: a broader photon is shorter in time, the detection of an 'early' photon is most likely the broader photon, and the detection of a 'late' photon has most likely the narrower linewidth. This discriminability ("which-

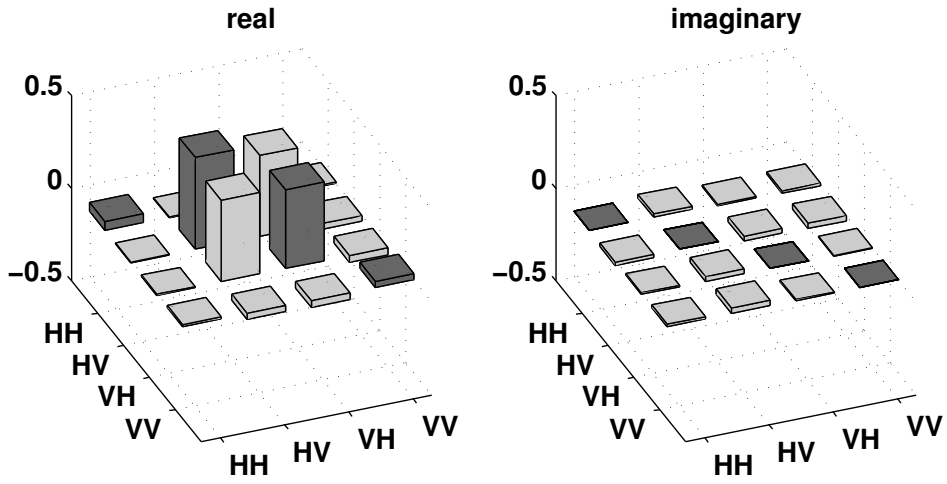

$$\begin{pmatrix} 0.05 & -0.00 & -0.01 & 0.01 \\ -0.00 & 0.50 & 0.44 & -0.03 \\ -0.01 & 0.44 & 0.43 & -0.04 \\ 0.01 & -0.03 & -0.04 & 0.03 \end{pmatrix} \begin{pmatrix} 0.00 & 0.02 & -0.01 & -0.01 \\ -0.02 & 0.00 & -0.02 & -0.03 \\ 0.01 & 0.02 & 0.00 & -0.00 \\ 0.01 & 0.03 & 0.00 & 0.00 \end{pmatrix}$$

Figure 3.23.: Reconstructed two-photon density matrix at 10 mW of 427 nm pump power.

path information") reduces the entanglement, the reduction is estimated to $\sim 99.4\,\%$ by calculating the overlap of two photons with Lorentzian spectral distributions and the measured linewidths ($\delta\omega_H$, $\delta\omega_V$). One possible source of the missing fidelity is again a wedge-angle of the used waveplates, whereby the detection probability for the projection settings is slightly different which results in an error in the reconstructed state. The reduced fidelity at high pump power is not understood. The creation of double pairs is a possible error source.

3.4. Resonant photon-pair source in interferometric configuration

To overcome the problem of reduced purity of the state due to the different linewidth of the two generated photons of one pair, or at higher pump power, we embed the resonator into a Mach-Zehnder type interferometer [100, 102]. The principle is depicted in figure 3.25. The blue pump photons are split by a 50:50 beam splitter (BS) and

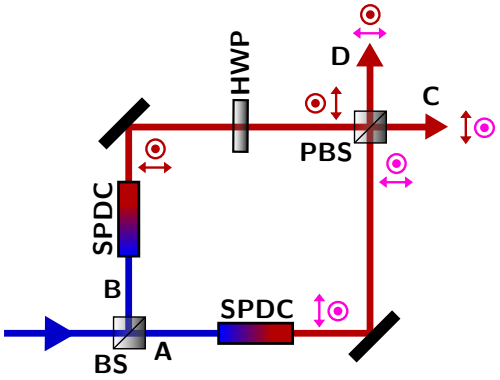

Figure 3.24.: Schematic of a two-crystal source of polarization entangled photons [102].

sent to two identical crystals with type-II phase-matching in each arm of the interferometer. When the two partial amplitudes of a blue photon get converted, we obtain the amplitude of a 'half pair' of orthogonal polarized red photons in each arm. By rotating the polarization in one arm, and overlapping the two 'half pairs' on a polarizing beam splitter (PBS) we get a maximal entangled state without post-processing where the distinguishability due to different linewidth $\delta\nu_{1,2}$, and the which-path information is erased. The result is a maximally entangled state of the form

$$|\Psi^{\varphi}\rangle = \frac{1}{\sqrt{2}}\left(\hat{a}^{\dagger}_{C,\delta\nu_1,H}\ \hat{a}^{\dagger}_{D,\delta\nu_2,V} + e^{i\varphi}\ \hat{a}^{\dagger}_{C,\delta\nu_1,V}\ \hat{a}^{\dagger}_{D,\delta\nu_2,H}\right)|0\rangle \tag{3.31}$$

with a phase φ that is given by the phase difference of the interferometer arms. This phase needs to be stable to get a fixed quantum state at the output of the interferometer. A passive stable scheme like in [101], obtained by an Sagnac-type of interferometer, is not possible in our case, so we need an interference signal to stabilize the interferometer. We utilize that the second polarizing beam splitter (PBS) is only partially polarizing at the pump wavelength, and use the interference fringes of the

unconverted light for the phase stabilization, which is explained later in this section. To account for losses inside the interferometer, efficiencies $\eta_{A,B}$ must be introduced into equation 3.31. These account for the splitting ratio of the BS, conversion efficiency and the loss in each arm of the interferometer. For an ideal PBS at the output we get the state

$$|\Psi^{\varphi}\rangle = \frac{1}{\sqrt{\eta_A^2 + \eta_B^2}} \left(\eta_A \ \hat{a}^{\dagger}_{C,\delta\nu_1,H} \ \hat{a}^{\dagger}_{D,\delta\nu_2,V} + \eta_B \ e^{i\varphi} \ \hat{a}^{\dagger}_{C,\delta\nu_1,V} \ \hat{a}^{\dagger}_{D,\delta\nu_2,H} \right) |0\rangle \tag{3.32}$$

which is the maximally entangled state of equation 3.31 when the efficiencies are balanced ($\eta_A = \eta_B$).

The interferometric scheme is demonstrated with single pass SPDC crystals, and waveguides, with high quality entanglement properties as documented in [101, 103, 120–123]. In the following a combination of the interferometric scheme with the resonant photon pair source is presented, with a characterization of the phase-tunable polarization entanglement. Part of this work was done in the master project of my colleague Jan Arensk̈otter. More information is found in his master thesis [124].

Instead of using two identical crystals, as in the schematic of figure 3.24, we pump the same crystal inside the optical resonator from two sides, and therefore excite two counter-propagating modes in the ring resonator. The two modes exit the resonator at the same mirror, but under different angles. The advantage is that any induced distinguishability, for example due to local heating, is identical for both modes and the interferometric overlap erases that distinguishability. A detailed setup is shown in figure 3.25. The 427 nm pump laser is sent to a 50:50 beam-splitter (BS). The transmitted output is first directed through the ring resonator, and focused into the SPDC crystal from the left. The reflected output of the BS is redirected by two mirrors (PM2) which are adjustable by piezo-stacks to control the phase difference of the interferometer. This beam passes a dichroic-mirror (DM) from the backside, and is then focused into the crystal from the right side. The two excited, and counter-propagating, modes at 854 nm exit the resonator at the same mirror (M_{out}) but under different angles. The photons generated by the pump beam from the left side exit under 0°, and from the right under 30° with respect to the crystal axis. The 0° mode is first collimated with a spherical lens, and then reflected by the dichroic mirror (DM) onto one input of the polarizing beam splitter. The 30° mode is shaped by a set of a cylindrical and a spherical lens to match the beam parameters of the 0° mode. The polarization is rotated by 90° (HWP2) until the beam is overlapped with the second input of the polarizing beam splitter. The two outputs of the PBS are then

sent through a chopper disk that alternates these two beams with an 854 nm reference laser beam (854 nm lock), which is used for stabilizing the resonator. The chopper prevents the single photon detectors from damage. One output is filtered with the FPI for single frequency mode operation.

As mentioned before, we use the unconverted 427 nm pump beam for the stabilization of the interferometer. The resonator is a part of this interferometer, and is actively stabilized. We therefore do not expect phase fluctuations from the resonator. The remaining task is the stabilization of the remaining paths of the blue interferometer and the two output paths. As illustrated in figure 3.26, we use the weak reflection from the dichroic mirror (DM) of the beam coming from the left side, and for the beam that is pumping the crystal from the right side we use the weak reflection at the cavity-outcoupling mirror (M_{out}). The PBS is designed for 854 nm and is only partially polarizing for 427 nm. We therefore see interference of the two beams. After the PBS we select the polarization with the highest contrast in the interference signal by using an linear-polarization filter (POL) before we detect the light for stabiliza-

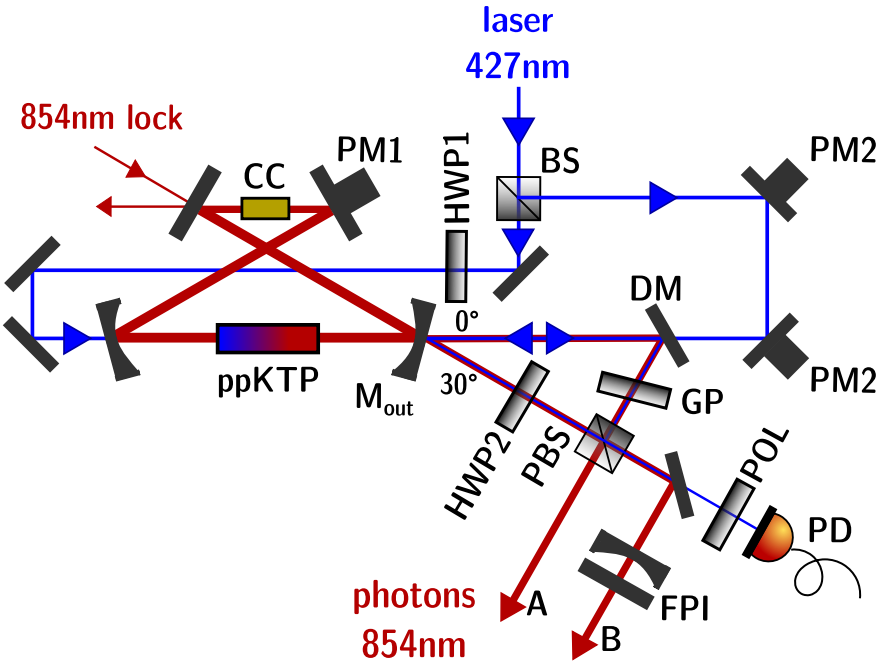

Figure 3.25.: Schematic of the interferometric source of polarization entangled photons.

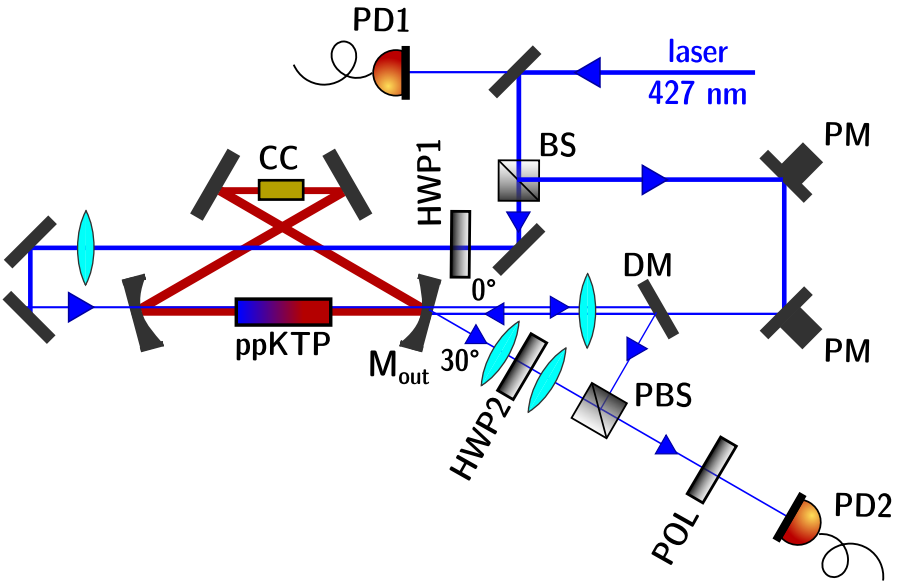

Figure 3.26.: Schematic of the interferometer used for stabilization.

tion with a photo-diode (PD2). A second photodiode (PD1) is used at the input of the interferometer to calibrate the interference signal. The second output of the PBS is not used. The stabilization of the resonator, together with the stabilization of the blue interferometer fulfills the requirements to generate a controlled phase φ of the state $|\Psi^{\varphi}\rangle$ according to equation 3.32. To adjust the efficiencies $\eta_{A,B}$ we do two steps. First the 854 nm-photon detection efficiency is tuned to equilibrium for both pump directions with the following procedure: by blocking subsequently one of the two pump beams inside the interferometer and recording a cross correlation of the detected photons between the two arms we measure the detection efficiencies for each arm (*c.f.* equation 3.15) and each pump direction. This is done with the alignment and beam shaping of the two out-coupled beams from the cavity-mirror (M_{out}) to the polarizing beam splitter (PBS) by the adjustment of the dichroic mirror (DM), and the polarizing beam splitter (PBS). The optimal alignment for both pump directions is reached when the generated photons from both pump directions overlap perfectly at the PBS. This procedure makes the assumption that the loss in the optical path from the PBS to the detector, and the detector efficiency is independent of the polarization,

and therefore equal for both pump directions, which is supported by our observations. With this assumption, also the efficiencies from the generation of a photon pair to the PBS are equal, which is the 854 nm part of the interferometer. It has to be noted that only the ratio of the efficiencies has to be equal for the two pump directions $\eta_{A,0°}/\eta_{B,0°} = \eta_{A,30°}/\eta_{B,30°}$, a symmetric imbalance is compensated by the second step. The second step to equalize the efficiencies $\eta_{A,B}$ is then performed by adjusting the number of detected photons for each pump direction. In this way the 427 nm part of the interferometer and the SPDC conversion (and also the aforementioned imbalance) is tuned by inserting loss in the interferometer arm that has higher efficiency. This is done with the half-waveplate (HWP1) in the 427 nm pump beam that pumps the crystal from the left. By rotating the polarization we adjust the amount of converted light, and as a result the detected number of photons of this arm. With this procedure we tune the efficiencies and approach the entangled state of equation 3.31.

The reconstructed density matrices for 40 mW of 427 nm pump power are shown in figure 3.28(a) with the phase set to $\varphi = 0°$, and in figure 3.29(a) with the phase set to $\varphi = 180°$. The data is corrected for lost-partner events and detector dark-counts by background subtraction. Fidelity, purity, and concurrence for the $|\Psi^+\rangle$, and the $|\Psi^-\rangle$ state are summarized in tables 3.28(b), and 3.29(b). In contrast to the observation of the previous section, there is no power dependence that influences the photonic state. The mean fidelity of 98.2 % is a clear improvement to the case without the interferometer. We found out that we have reflections of the photons, and the pump beam mainly at the crystal surfaces which are perpendicular to the beam propagation direction. These reflections mix up the state and should be the main error source for the residual infidelity of the generated photonic state. Using crystals with angled surfaces whereby the reflections are not coupled to the counter-propagating mode would be a possible improvement. It should be noted that the background-corrected values have to be handled with care. The accidental events due to lost partners are inherent with SPDC as described in section 3.2 and cannot be neglected in a network scenario.

From the detected rates we infer the single-mode photon-pair rate per pump power to be $4.5(5) \times 10^4/(\mathrm{s\,mW})$ measured from the input (BS) to the output (PBS) of the interferometer. This value is about two times lower as without the interferometer. The main reason for the lower value is the loss of the optical components for the blue part of the interferometer.

A demonstration of the tunability of the phase in the photonic state 3.31 is given in figure 3.27. Two scans of the reconstructed phase of the two-photon state in

(a)

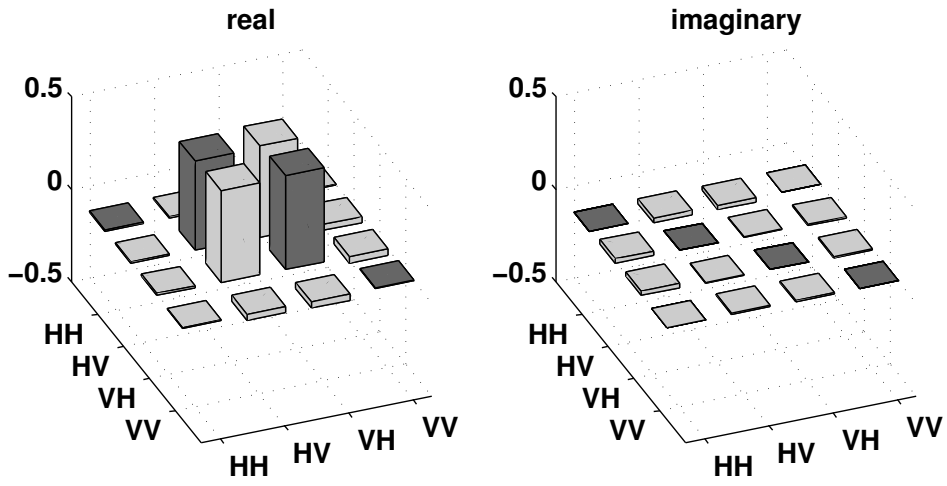

$$\begin{pmatrix} 0.01 & 0.01 & 0.01 & -0.00 \\ 0.01 & 0.48 & 0.49 & -0.03 \\ 0.01 & 0.49 & 0.51 & -0.04 \\ -0.00 & -0.03 & -0.04 & 0.01 \end{pmatrix} \quad \begin{pmatrix} 0.00 & -0.02 & -0.02 & 0.00 \\ 0.02 & 0.00 & 0.00 & -0.01 \\ 0.02 & -0.00 & 0.00 & -0.01 \\ -0.00 & 0.01 & 0.01 & 0.00 \end{pmatrix}$$

(b)

Pump power (mW)	Fidelity $\langle\Psi^+\vert\,\hat{\rho}\,\vert\Psi^+\rangle$	Purity $\mathrm{tr}(\hat{\rho}^2)$	Concurrence
10	0.982(9)	0.970(17)	0.97(2)
20	0.979(8)	0.970(13)	0.97(2)
30	0.983(8)	0.974(15)	0.98(1)
40	0.982(4)	0.972(7)	0.98(1)

Figure 3.28.: The photonic phase is set to $\varphi = 0°$. (a) Reconstructed two-photon density matrix at 40 mW of 427 nm pump power. (b) Fidelity, purity and concurrence of in dependence of the pump power.

(a)

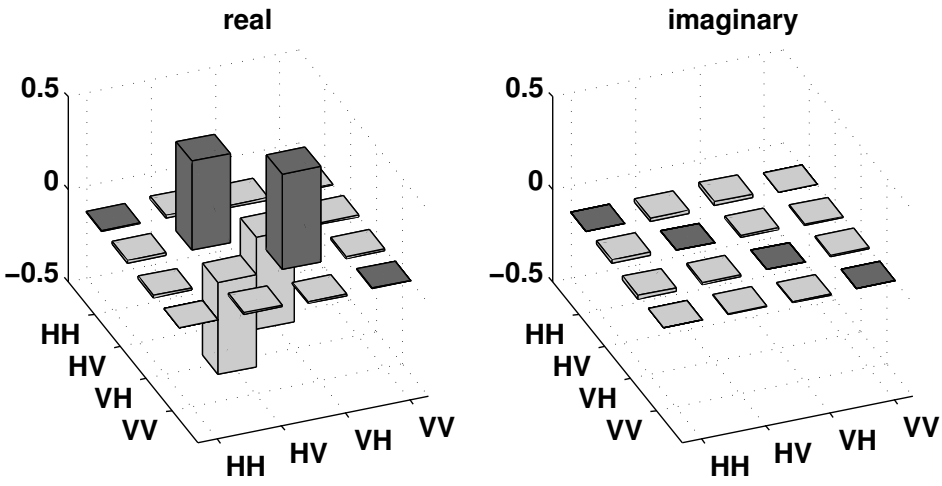

$$\begin{pmatrix} 0.00 & 0.01 & -0.01 & -0.00 \\ 0.01 & 0.48 & -0.50 & 0.01 \\ -0.01 & -0.50 & 0.51 & -0.01 \\ -0.00 & 0.01 & -0.01 & 0.00 \end{pmatrix} \quad \begin{pmatrix} 0.00 & -0.02 & 0.02 & -0.00 \\ 0.02 & 0.00 & 0.01 & -0.00 \\ -0.02 & -0.01 & 0.00 & 0.01 \\ 0.00 & 0.00 & -0.01 & 0.00 \end{pmatrix}$$

(b)

Pump power (mW)	Fidelity $\langle\Psi^-\vert\,\hat{\rho}\,\vert\Psi^-\rangle$	Purity $\mathrm{tr}(\hat{\rho}^2)$	Concurrence
10	0.985(11)	0.976(19)	0.97(2)
20	0.981(8)	0.970(16)	0.97(2)
30	0.983(8)	0.972(15)	0.97(1)
40	0.983(5)	0.971(9)	0.97(1)

Figure 3.29.: The photonic phase is set to $\varphi = 180°$. (a) Reconstructed two-photon density matrix at 40 mW of 427 nm pump power. (b) Fidelity, purity and concurrence of in dependence of the pump power.

dependence of the interferometer stabilization setpoint are shown. A 3 mm thick glass plate (GP) (*c.f.* figure 3.25) is used in one arm of the interferometer before the PBS to add an additional phase-shift between the 427 nm light that is used for stabilizing, and the 854 nm photons. By tilting the glass plate the effective path-length difference is controlled. The red data in figure 3.27 shows a scan with an additional phase-offset of about 220°. The blue data is without the additional glass plate. The linear variation

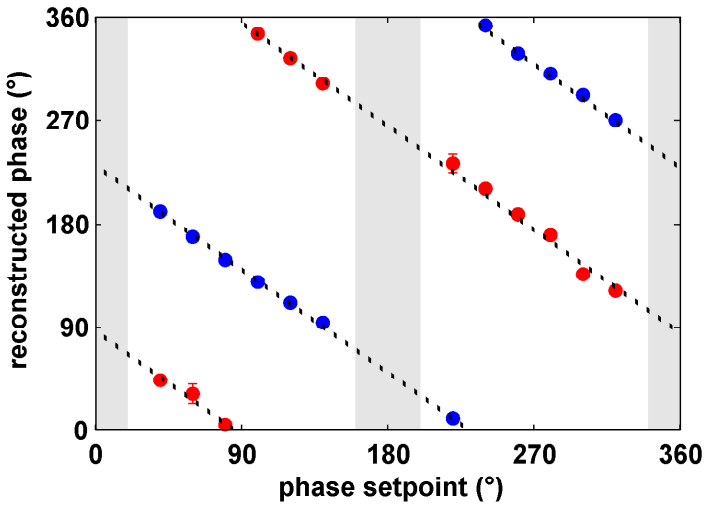

Figure 3.27.: Reconstructed phase of the two-photon state in dependence of the interferometer stabilization setpoint (blue dots). The red dots are recorded with an additional glass plate. The gray shaded areas are the unfavorable setpoints close to the maximum and minimum of the cosinusoidal interference signal.

of the reconstructed photonic phase with phase setpoint is clearly observed. No data is recorded in the gray shaded areas, where the slope of the cosinusoidal interference signal is to small for an adequate stabilization. A phase offset between setpoint and reconstruction is also notable. The reason for the difference is the dispersion of the optical components. The stabilization setpoint in combination with the tilt of the glass plate allows tuning the phase of the state to any desired angle.

The high pair rate, the narrowband frequency-degenerate spectral properties, and the excellent polarization entanglement make the presented photon-pair source a suitable and efficient resource of entanglement for quantum network experiments with $^{40}Ca^{+}$ quantum nodes, which will be explained in the following chapter.

3.5. Summary

The source described in this chapter is based on type-II conversion in a ppKTP crystal for the conversion from 427 nm to 854 nm. The generated photon pairs are orthogonally linear polarized and frequency degenerate at the atomic resonance. The conversion is enhanced by a bow-tie ring resonator, resonant for both generated photons with an additional compensation crystal inside, to be able to tune the resonator doubly resonant for the two photons, and to the atomic resonance at the same time.

The measured linewidth and finesse is $\delta\omega_V = \pi \times 8.4\,\mathrm{MHz}$ and $\mathcal{F}_V = 150.2(1)$ ($\delta\omega_H = 2\pi \times 10.4\,\mathrm{MHz}$ and $\mathcal{F}_H = 121.2(1)$) of the vertically- (horizontally-) polarized photons. The difference in free spectral range results in a cluster with ~ 6.4 modes. The available single-mode pair rate was measured to $R_{out} = 88(1) \times 10^3/(\mathrm{s\,mW})$, which is the single-mode pair rate outside the resonator including the optical chopper.

The entanglement was characterized with two strategies for the generation of polarization entanglement. The first using a non polarizing beam splitter and post selection, a fidelity with the maximal entangled $|\Psi^+\rangle$ state of 98.2 % was measured at low pump power (200 µW). At higher pump power (10 mW) a drop to a fidelity of 89.7 % was measured. With the second strategy, using the principle of the interferometric-type sources, where the photon pair source is embedded in an interferometer for the pump and the output path generating entangled photon pair states, a mean fidelity of 98.2 % was measured at pump powers of up to 40 mW, with a single-mode photon-pair rate per pump power of $4.5(5) \times 10^4/(\mathrm{s\,mW})$, a clear improvement to the case without the interferometer. The tunability of the phase in the photonic state from $|\Psi^+\rangle$ to $|\Psi^-\rangle$ was also characterized.

The photon pair source presented in this chapter is now used in experiments with a single trapped $^{40}Ca^+$ ion with its two modes of operation: as heralded single photon source to generate heralded single photons in a defined polarization state, and as a source of entangled photon pairs.

4. Quantum network experiments

Quantum network experiments that combine the photon pair source and the $^{40}Ca^{+}$ ion as quantum node are presented in this section. The experiments demonstrate the qualities of the trapped ion in receiver mode, which also offers an alternative way for quantum state readout via quantum state teleportation.

The first experiment is about the characterization of the photon-to-atom quantum-state-transfer protocol. A similar protocol was already demonstrated in [26, 66] with laser photons whose polarization-qubit state was mapped onto the ion's ground-state qubit. The protocol is now extended to a more efficient protocol for our setup, and heralded single photons are used whose quantum states are mapped. Section 4.1 contains a theoretical description of the protocol, and an overview of the relevant error sources. Section 4.2 contains the experimental results including a full quantum process tomography. The transfer of photon-photon to atom-photon entanglement by the use of the protocol is the subject of section 4.3. Two experiments are presented which differ in their initial photon-photon entanglement creation. The first one uses the source presented in section 3.3.8, and the second one uses the source in interferometric configuration of section 3.4.

Section 4.4.1 describes a protocol for atomic state readout by teleporting the atomic quantum state onto the polarization state of a single photon, which comprises an alternative to direct mapping via the emission of a single photon [25, 27]. The necessary resource of entanglement is provided by the interferometric photon pair source of section 3.4. The projective Bell-state measurement is performed by a heralded absorption process, i.e., an atomic Raman transition and subsequent projective measurement of the final atomic state and the generated Raman-photon. The protocol is described in section 4.4.1. A discussion of the experimental data is presented in section 4.4.2. The last experiment, in section 4.5, connects the entangled photon-pair source to telecom wavelength via quantum frequency conversion.

4.1. Photon to atom quantum-state transfer: Protocol

A schematic with the relevant levels and transitions of the protocol for photon-to-atom state transfer is shown in figure 4.1. The implemented scheme for starts with a

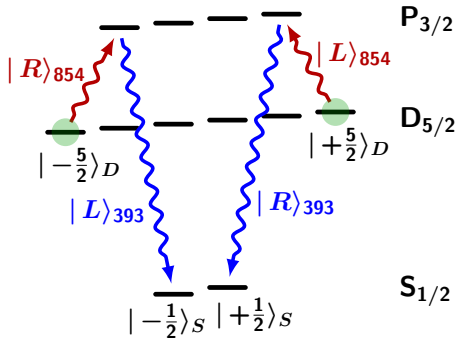

Figure 4.1.: Relevant level-scheme for the photon-to-atom state transfer.

coherent superposition of the $|\pm 5/2\rangle_D = |\mathrm{D}_{5/2},\ m = \pm 5/2\rangle$ Zeeman levels with phase φ_0

$$|\Psi\rangle_D = \frac{1}{\sqrt{2}}\Big(|-5/2\rangle_D + e^{i\varphi_0}\,|+5/2\rangle_D \Big) \tag{4.1}$$

An 854 nm photon with the polarization state expressed in the circular basis $\{|L\rangle,\ |R\rangle\}$ with amplitudes α and β,

$$|\Psi\rangle_{854} = \alpha\,|R\rangle_{854} + \beta\,|L\rangle_{854} \tag{4.2}$$

is then focused onto the ion along the magnetic field axis. This means that we have a direct translation from the laboratory polarization basis into the natural atomic basis: $|R\rangle_{854} \rightsquigarrow \sigma^+_{854}$-transition, and $|L\rangle_{854} \rightsquigarrow \sigma^-_{854}$-transition. The ion decays with 93.47 % probability to $\mathrm{S}_{1/2}$ (*c.f.* figure 2.1: A_{393}/Γ) after absorbing the 854 nm photon with the polarization $|\Psi\rangle_{854}$. Thereby a 393 nm Raman photon in the state $|\varphi\rangle_{393}$ gets emitted. The detection of this photon enables us to identify a successful absorption, we therefore call it herald of absorption. Only heralded absorption events are taken into account in the protocol. There are two other possible decay channels. The first leads with 0.66 % probability to the metastable $\mathrm{D}_{3/2}$ level (A_{850}/Γ) that is not part of the process. Thus we get no herald, and the fidelity of the final state is not affected, only the efficiency is lowered. The second decay channel is back to the $\mathrm{D}_{5/2}$ level with 5.87 % probability (A_{854}/Γ) where the ion can absorb another 854 nm photon. The influence of this decay channel to the final state is discussed later in this section.

We collect the 393 nm photon along the magnetic field axis, so we have the translation from the natural atomic basis to the laboratory basis: σ^{+}_{393}-transition $\rightsquigarrow |L\rangle_{393}$ and σ^{-}_{393}-transition $\rightsquigarrow |R\rangle_{393}$. The absorption of the 854 nm photon, and the transition to the Zeeman sublevels $|\pm 1/2\rangle_S = |\mathrm{S}_{1/2},\ m = \pm 1/2\rangle$ with the emission of the 393 nm herald is described by the Raman process operator [71]

$$\hat{\mathrm{R}}_{854,D} = \ |L\rangle_{393}\,|{-1/2}\rangle_S\,\langle R|_{854}\,\langle {-5/2}|_D \ + \ |R\rangle_{393}\,|{+1/2}\rangle_S\,\langle L|_{854}\,\langle {+5/2}|_D \tag{4.3}$$

The joint state of atom and 393 nm photon after absorption and emission of the herald is then

$$\begin{aligned} |\Psi\rangle_{joint} &= \hat{\mathrm{R}}_{854,D} \ \ |\Psi\rangle_{854} \otimes |\Psi\rangle_D \\ &= \frac{1}{\sqrt{2}}\Big(\alpha\ |L\rangle_{393}\,|{-1/2}\rangle_S + \beta\, e^{i\varphi_0}\ |R\rangle_{393}\,|{+1/2}\rangle_S\Big) \end{aligned} \tag{4.4}$$

which is in general an entangled atom-photon state. By projecting the 393 nm photon of the joint state $|\Psi\rangle_{joint}$ onto the linear polarizations

$$|H\rangle_{393} = \frac{|R\rangle_{393} + |L\rangle_{393}}{\sqrt{2}} \qquad |V\rangle_{393} = \frac{|R\rangle_{393} - |L\rangle_{393}}{i\,\sqrt{2}} \tag{4.5}$$

we complete the mapping process and obtain the final $|S\rangle_{1/2}$ state

$$|\Psi\rangle_S = \frac{1}{\sqrt{2}}\ \big(\alpha\,|{-1/2}\rangle_S \pm \beta\, e^{i\varphi_0}\ |{+1/2}\rangle_S\big) \tag{4.6}$$

depending on the result, $|H\rangle_{393}$ or $|V\rangle_{393}$, of the photon projection. When the initial phase φ_0 is zero, then the polarization state of the incoming 854 nm photon $|\Psi\rangle_{854}$ is mapped onto the atomic ground-state spin qubit $|\Psi\rangle_S$. The initial atomic phase φ_0 is composed of a constant phase due to the preparation, and a time dependent phase $\omega_L t$ because of the Larmor precession with frequency ω_L that arises from the energy difference of the Zeeman sublevels. This time dependence is not a problem, and can be corrected[1] by using the detection time of the herald of absorption at 393 nm. It has to be noted that there is also a constant contribution at a fixed detuning of the 854 nm photons to the phase due to the scattering of 393 nm photons [74]. The constant phase contributions in the protocol are calibrated in the measurements and compensated with a constant offset.

[1] The detection time t of the 393 nm herald is measured, and the magnetic field, which sets the Larmor frequency is controlled. The phase φ_0 can therefore be calculated in real time and compensated, in order to match $|\Psi\rangle_S$ to $|\Psi\rangle_{854}$, by shifting the reference oscillator phase by this value.

4.1.1. Efficiency considerations

The overall efficiency of the photon-to-atom state mapping protocol consists of the absorption efficiency of the 854 nm photon, the internal efficiency of the scheme, and the detection efficiency of the 393 nm heralding photon. The three efficiencies are discussed in the following:

- **Absorption efficiency of the 854 nm photon:**
  The first part of the absorption efficiency of the 854 nm photon is given by the overlap of the spatial profile of the photons with the dipole pattern of the ion. The photons are sent to the ion trap setup via a single mode optical fiber, we therefore take the mode overlap of a Gaussian beam with the fraction of the dipole pattern that is collected by the HALO into account. This overlap is estimated to $\eta_{SM} \approx 40\,\%$ [73] when the incoming beam waist coincides with the radius of aperture. The second contribution is the fraction of the dipole pattern that is collected by the HALO, which is aligned along the quantization axis. When considering the solid-angle of the HALO we get an (multi-mode) overlap

  $$\eta_\sigma = 6\,\% \qquad \eta_\pi = 0.51\,\% \tag{4.7}$$

  for the two transitions [67]. The last contribution to the absorption efficiency is the oscillator strength, which is given by the Einstein coefficients $A_{854}/\Gamma = 5.87\,\%$ (see figure 2.1). The loss in the optical components at 854 nm are very low and neglected in this estimation.

- **Internal efficiency:**
  The internal efficiency of the protocol is mainly limited by the factor of $1/\sqrt{2}$ in equation 4.6 to $\eta_{int} = 50\,\%$. This can be seen as a mean overlap of 50 % between all possible incoming polarizations and the polarization that the atom can absorb optimally. This is most easily seen when the ion is in one of the $|\pm 5/2\rangle_D$ states, because then it only absorbs one circular polarization. The second contribution to the internal efficiency is the branching ratio: after absorbing an 854 nm photon, the ion decays with $A_{393}/\Gamma = 93.47\,\%$ probability to $S_{1/2}$.

- **Detection efficiency of the heralding photon:**
  The last contribution is the detection efficiency of the heralding photon at 393 nm. We collect these photons with the second HALO, project them with a polarizing beam splitter, and send these in free space or via a multi-mode fiber

to the detector. We therefore collect η_σ of the σ-transition emission pattern due to the multi-mode collection. The last contribution is transmission of optical components $\eta_{loss,393} \approx 90\,\%$ and the detector quantum efficiency $\eta_{det} \approx 55\,\%$ of the APDs[2] (or $\eta_{det} \approx 30\,\%$ when using PMTs[3]).

The total protocol efficiency starting with a fiber coupled 854 nm photon is

$$\eta_{total} = \underbrace{\eta_{SM}\,\eta_\sigma\,\frac{A_{854}}{\Gamma}}_{\text{absorption}} \cdot \underbrace{\eta_{int}\,\frac{A_{393}}{\Gamma}}_{\text{internal}} \cdot \underbrace{\eta_\sigma\,\eta_{loss,393}\,\eta_{det}}_{\text{herald detection}} \approx 1.95 \times 10^{-5} \tag{4.8}$$

from input to output when using the APDs and 1.07×10^{-5} when using the PMTs.

4.1.2. Influence of phase jitter

From equation 4.6 we see that uncertainties in the determination of φ_0 decrease the state-mapping fidelity. Possible origins are timing uncertainties in the preparation of the initial superposition in $D_{5/2}$ (*c.f.* equ. 4.1), magnetic field fluctuations during the exposure time, and the timing jitter of the 393 nm herald detection. The frequency standard in the laboratory is given by a rubidium atomic clock[4] which provides a 10 MHz frequency with a one second Allan Variance of $< 2 \times 10^{-11}$. We can therefore neglect timing uncertainties in the preparation. Magnetic field fluctuations are a serious problem. We quantify the the coherence time of the initial superposition in $|\mathrm{D}_{5/2},\ m = \pm 5/2\rangle$ with Ramsey measurements: the sequence starts with optical pumping to $|\mathrm{S}_{1/2}, \mathrm{m} = -1/2\rangle$, an RF $\pi/2$-pulse creates the 50:50 superposition in $\mathrm{S}_{1/2}$ and two subsequent π-pulses with the 729 nm laser generate the superposition $(|\mathrm{D}_{5/2}, \mathrm{m} = -5/2\rangle + |\mathrm{D}_{5/2}, \mathrm{m} = +5/2\rangle)/\sqrt{2}$. After the waiting time in $\mathrm{D}_{5/2}$ (scanning parameter) we apply again two 729 nm π-pulses and the second RF $\pi/2$-pulse with phase offset that finishes the Ramsey sequence. A consecutive state projection onto $|\mathrm{S}_{1/2}, \mathrm{m} = \pm 1/2\rangle$ is performed using electron shelving with an additional 729 nm π-pulse and fluorescence detection. We now scan the phase offset of the second RF $\pi/2$-pulse and measure the visibility for each waiting time. Such a scan is shown in figure 4.2 with a coherence time of 178 µs. The maximal possible fidelity is in fixed relation $\mathcal{F} = (1 + \mathrm{V})/2$ with the plotted visibility V. At the 1/e coherence time with $\sim 60\,\%$ visibility we get a maximum achievable state fidelity of 80 %.

[2]Laser Components, COUNT® BLUE
[3]Hamamatsu, H7422P-40 SEL; PicoQuant, PAM 102-P
[4]Stanford Research Systems, FS725

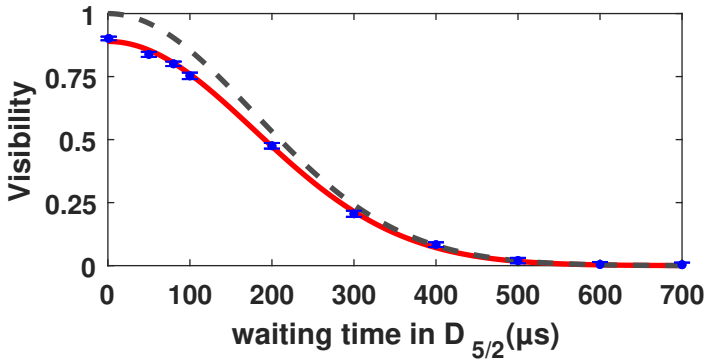

Figure 4.2.: Ramsey measurement with waiting time in $(|\mathrm{D}_{5/2}, \mathrm{m} = -5/2\rangle + |\mathrm{D}_{5/2}, \mathrm{m} = +5/2\rangle)/\sqrt{2}$. The fit (red line) with a Gaussian distribution reveals the 1/e coherence time of the superposition of 178 µs. The curve does not start at 1, the main reason for this are imperfections in the 729 nm π-pulses which have an efficiency of $\sim$ 98 %. The gray line shows the ideal curve, when only fluctuations during the waiting time in $\mathrm{D}_{5/2}$ are considered (the amplitude is set to 1).

The 393 nm photon detection has two possible jitter sources. The first one is caused by the time jitter of the single-photon detector, in our case an avalanche photo-diode (APD[5]) or a photo-multiplier tube (PMT[6]). The second one is the time resolution of the time-tagging electronics.

To estimate the effect on the final state, we consider a mapped state (c.f. equ. 4.6) with additional phase φ_j. The overlap fidelity $\mathcal{F}$ with the state after an ideal process is then given by

$$\mathcal{F}(\varphi_j) = \left| \langle \Psi |_{S,ideal} \, |\Psi\rangle_{S,jitter} \right|^2 = \left| \alpha^2 + e^{i\,\varphi_j}\, \beta^2 \right|^2 \tag{4.9}$$

The highest effect on the fidelity is found for the mapping of a linear polarization ($|\alpha| = |\beta| = 1/\sqrt{2}$), and equ. 4.9 simplifies to

$$\mathcal{F}(\varphi_j) = \frac{1 + \cos(\varphi_j)}{2} \tag{4.10}$$

We assume a Gaussian-distributed timing jitter with standard deviation σ. The ex-

[5]Laser Components, COUNT® BLUE
[6]Hamamatsu, H7422P-40 SEL; PicoQuant, PAM 102-P

pectation value of the fidelity is then given by

$$\langle \mathcal{F} \rangle = \frac{1}{2\sqrt{2\pi\sigma^2}} \int_{-\infty}^{\infty} e^{-\frac{\varphi_j^2}{2\sigma^2}} \left(1 + \cos(\varphi_j)\right) \mathrm{d}\varphi_j \tag{4.11}$$

The used APDs have a specified jitter of 1 ns. At 3 G magnetic field we get a Larmor frequency in the range of 16 MHz. This results in a phase jitter of $\sigma = 2\pi \cdot 16\,\mathrm{MHz} \cdot 1\,\mathrm{ns} \approx 0.1$, and the corresponding expectation value of the fidelity is $\langle \mathcal{F} \rangle = 99.75\,\%$ (the PMTs have even lower timing jitter of $\sim 228\,\mathrm{ps}$). In the experiments we use two different time tagging electronics with 82.3045 ps[7], and 320 ps[8] per least significant bit. The expected fidelity due to this discretization is more than 99.97 %. These two timing jitter are both negligible compared to the reduced fidelity due to magnetic field fluctuations at waiting times $> 10\,\mu\mathrm{s}$.

4.1.3. Coherence of the final state vs. the branching ratio

The protocol of section 4.1 assumes that the atom-to-photon state transfer is performed with a single 854 nm photon, and that the ion decays to $S_{1/2}$ whereby a 393 nm Raman photon is scattered. But what happens if we perform the protocol by sending a stream of photons with rate R and the back decay is taken into account?

The branching ratio from the excited $P_{3/2}$ state to the final $S_{1/2}$ state is $A_{854}/\Gamma = 94.1\,\%$ (c.f Einstein coefficients in fig. 2.1). This tells us there is a non negligible probability of decaying back to the initial $D_{5/2}$ state after absorbing a 854 nm photon, whereby the phase of the absorbed photon contributes. There are decay channels to all of the Zeeman sublevels of $D_{5/2}$, it follows that a second absorbed 854 nm photon releases a 393 nm which has all the possible transitions from $P_{3/2}$ to $S_{1/2}$. The projection of the 393 nm photons for the protocol lead therefore to a statistical mixture in the final state if there was a back decay to $D_{5/2}$. We describe the final state in $S_{1/2}$ with the density matrix

$$\rho_S = (1 - \Phi) \left|\Psi\right\rangle_S \left\langle\Psi\right|_S + \frac{\Phi}{2} \mathbb{1} \tag{4.12}$$

with the parameter Φ and the ideal output state of the protocol $\left|\Psi\right\rangle_S$ (*c.f.* equation 4.6). The fidelity of ρ_S with the ideal output state is then given by

$$\mathcal{F} = \left\langle\Psi\right|_S \rho_S \left|\Psi\right\rangle_S = 1 - \frac{\Phi}{2} \tag{4.13}$$

[7]Roithner Lasertechnik, TTM8000
[8]Signadyne, SD-PXE-TDC-H3345-1G

For an infinite waiting time t is the parameter Φ given by the probability for a back decay to $D_{5/2}$, which is the branching ratio A_{854}/Γ [125]. This corresponds to a fidelity of 97 %. In the limit of waiting times close to zero it must be 100 %. We treat the process

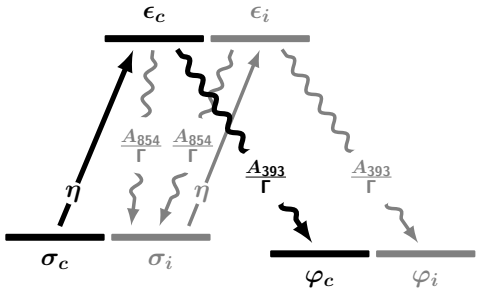

Figure 4.3.: Simplified Λ-like level scheme with coherent and incoherent part.

in the simplified Λ-like level scheme of figure 4.3 to estimate the amount of 393 nm photons that contribute to the mixing of the final state between the two limits. The ideal protocol translates to this picture in the following way: the initial superposition of the protocol (*c.f.* equation 4.1) is considered as the coherent part σ_c, which is a pure superposition. A first absorption with probability η leads to the coherent excited part ϵ_c, which decays with probability A_{393}/Γ to the final coherent superposition φ_c. The back decay to $D_{5/2}$ with probability A_{854}/Γ leads to the incoherent part of the level scheme, where all following absorptions remain incoherent and lead to the incoherent final part φ_i. The rate equations for σ_c, σ_i and $\sigma = \sigma_c + \sigma_i$ are written as

$$\dot{\sigma_c} = -R\eta\ \sigma_c \tag{4.14}$$

$$\dot{\sigma_i} = -R\eta\ \sigma_i + \frac{A_{854}}{\Gamma} R\eta\ \sigma_i + \frac{A_{854}}{\Gamma} R\eta\ \sigma_c \tag{4.15}$$

$$\dot{\sigma} = \dot{\sigma_c} + \dot{\sigma_i} = -\frac{A_{393}}{\Gamma} R\eta\ \sigma \tag{4.16}$$

with the solutions

$$\sigma_c(t) = e^{-R\eta t} \qquad \sigma(t) = e^{-\frac{A_{393}}{\Gamma} R\eta t} \tag{4.17}$$

The rate equations for the final states are then given by

$$\dot{\varphi_c} = \frac{A_{393}}{\Gamma} R\eta\ \sigma_c \qquad \dot{\varphi_i} = \frac{A_{393}}{\Gamma} R\eta\ \sigma_i \qquad \dot{\varphi} = \dot{\varphi_c} + \dot{\varphi_i} = \frac{A_{393}}{\Gamma} R\eta\ \sigma \tag{4.18}$$

The parameter Φ of the of the resulting density matrix in dependence of exposure

time interval T is then given by $\Phi(T) = 1 - {}^{\varphi_c(T)}/_{\varphi(T)}$. This leads to the fidelity

$$\mathcal{F}(T) = 1 - \frac{\Phi(T)}{2} = \frac{1}{2}\left(1 + \frac{\int_0^T \dot{\varphi}_c \, dt}{\int_0^T \dot{\varphi} \, dt}\right) = \frac{1}{2}\left(1 + \frac{A_{393}}{\Gamma} \frac{1 - e^{-R\eta T}}{1 - e^{-\frac{A_{393}}{\Gamma} R\eta T}}\right) \tag{4.19}$$

Figure 4.4 shows the fidelity, and the final population in dependence of the mean number of absorptions in the time interval T defined as $N = R\eta T$. We see that

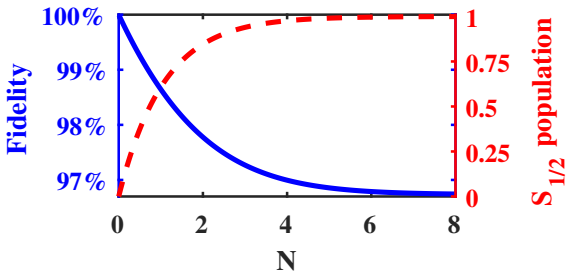

Figure 4.4.: Fidelity (blue line), and the final population in $S_{1/2}$ (red line) in dependence of the mean number of absorptions.

the fidelity for low number of absorptions is close to 100 % and for large number of absorptions it tends to ${}^{A_{854}}/_{\Gamma} \approx 97\,\%$.

4.2. Photon to atom quantum-state transfer

This experiment implements and characterizes the photon-to-atom state-mapping protocol of section 4.1 with single photons. We use the photon-pair source as heralded single-photon source as described in section 3.3. The frequency-degenerate photon pairs, resonant with the atomic $D_{5/2}$ - $P_{3/2}$ transition, are split with a polarizing beam splitter (PBS) as depicted in figure 4.5, and the bandpass filter (FPI) is used in the transmitted arm for single-mode operation. A photon detection in this horizontally-polarized arm heralds the presence of the ion-resonant partner photon with vertical polarization in the reflected arm. The vertical partner photons are sent through a ${}^{\lambda}/_{2}$- and a ${}^{\lambda}/_{4}$-waveplate to rotate the polarization to well-defined state $|\Psi\rangle_{854}$, and are then guided via ∼7 m optical single-mode fiber[9] to the ion-trap setup. The out-coupled beam gets expanded to ∼2 cm before it enters the vacuum chamber and is focused onto

[9]Non polarization maintaining, Thorlabs P3-780A-FC-5 and P3-780A-FC-2 connected with a fiber to fiber connector.

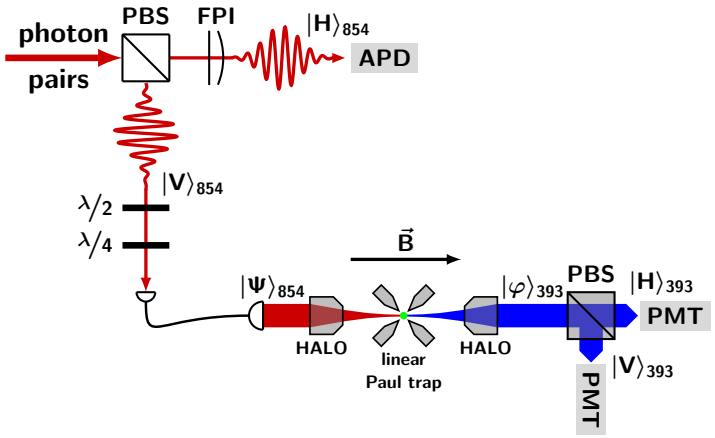

Figure 4.5.: Schematic of the experiment. The frequency-degenerate photon pairs, resonant with the atomic $D_{5/2}$ - $P_{3/2}$ transition, are split with a polarizing beam splitter (PBS). The transmitted photons are spectrally filtered (FPI) and used as heralds, and the polarization of the reflected photons is adjusted with a half- and a quarter-wave plate and sent to the ion-trap setup.

the ion with a HALO. This photon in the state $|\Psi\rangle_{854}$ is now used as input state for the photon to atom quantum state transfer protocol (cf. section 4.1). The magnetic field axis is aligned with the HALO axis, and the herald of absorption in the state $|\varphi\rangle_{393}$ at 393 nm is collected on the same axis. The herald of absorption is then projected with a polarizing beam splitter to the linear $|H/V\rangle$-polarization basis behind the vacuum chamber and detected with a photo-multiplier tube (PMT)[10]. The angles of the two 854 nm waveplates were calibrated with a polarimeter[11] placed in front of the vacuum chamber – the closest position with respect to the ion we can access – to provide six input polarizations $\{|H\rangle, |D\rangle, |V\rangle, |A\rangle, |R\rangle, |L\rangle\}$. After the state-mapping protocol a tomography of the atomic state for each of the input polarizations is performed to reconstruct the quantum process matrix [126].

Preparatory measurement: Absorption rate

At the beginning of the experiment we performed three preparatory measurements. The first is about the absorption rate. We prepare the ion in the $|D_{5/2},\ m = -5/2\rangle$ Zeeman state, switch on the cooling laser, and we send σ^+-polarized photons to the

[10]Hamamatsu, H7422P-40 SEL
[11]Thorlabs PAX5710IR1-T

ion. To get the absorption rate we correlate the time of preparation with the detection of a quantum jump. A quantum jump is detected on the transition from the dark to a bright ion. In the dark period the ion is still in the $|D_{5/2},\ m = -5/2\rangle$ state, and the only detections are detector dark counts. In the bright period the ion is emitting fluorescence due to the cooling laser. More details on the quantum-jump detection is found in [64]. The inverse of the rate of detected fluorescence photons limits the time resolution for the quantum jump detection to $\sim 7.5\,\mu s$. The correlation of the preparation time (at $\tau = 0$) with the detected quantum jump time is shown in figure 4.6. One sees a steep rise followed by an exponential decay. It is not completely

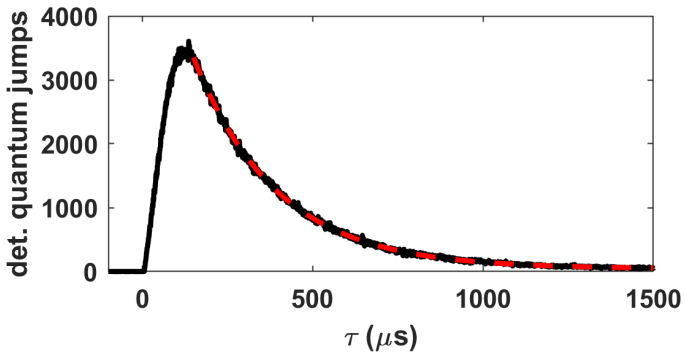

Figure 4.6.: Histogram of waiting times τ between the preparation of the ion in $D_{5/2}$ and its exposure to 854 nm photons (at $\tau = 0$), and the detected quantum jumps. The fit (red line) reveals an absorption rate of $R_{abs} = 4345(7)\,s^{-1}$.

clear what caused the relatively long rise time of $\sim 100\,\mu s$, as we have not observed this in other experiments. One reason might be the chopper used for stabilization of the SPDC resonator (see section 3.3). The preparation of the ion was not synchronized with the chopper which is used to switch between the stabilization laser and the photon-pair generation. This results in cycles in that the photon exposure starts at a random time during the exposure window, causing a time-spread. The important conclusion from the data is the time constant of the exponential decay of the curve. This effective lifetime τ_{eff} is extracted by a fit to the exponential decay, and the absorption rate is derived as $R_{abs} = \left(\tau_{eff}^{-1} - \tau_{sp}^{-1}\right)/0.94$, corrected for spontaneous decay from $|D_{5/2}\rangle$ to $|S_{1/2}\rangle$ with $\tau_{sp} = 1.17\,s$, and for the fraction of undetected absorptions ($\sim$6 %) that lead to decay back to $|D_{5/2}\rangle$. The result is an absorption rate of $R_{abs} = 4345(7)\,s^{-1}$ at a 427 nm pump power of 23.4 mW. With the generated single-mode pair rate of $R_{SM,pair} = 1.56(3) \times 10^5/(s\,mW)$ inside the crystal

(*c.f.* section 3.3.6), 83 % escape probability and 83 % fiber coupling and optical loss we calculate $R_{photons} = 2.5 \times 10^6\,\mathrm{s}^{-1}$ fiber-coupled resonant photons sent to the ion when the chopper that is used for stabilization is open. As a result we get an absorption probability of $\eta_{abs} = {}^{R_{abs}}/_{R_{photons}} = 1.7 \times 10^{-3}$ of the fiber coupled photons. The comparison with the ideal coupling efficiency (*c.f.* section 4.1.1) $\eta_\sigma \frac{A_{854}}{\Gamma} = 3.6 \times 10^{-3}$ yields a fiber coupling efficiency of 48.2 %.

Preparatory measurement: Photon switching

In order to avoid absorption outside the exposure time, it is required to switch off the photon stream off during the preparation of the superposition in $|D_{5/2},\ m = \pm{}^5/_2\rangle$ needed for the protocol, and during the electron shelving needed to project the ion onto a certain basis. Preparation is performed in $\sim 10\,\mu\mathrm{s}$, the probability for having an absorption in this period is about 4 %. Electron shelving with subsequent fluorescence detection is performed in $\sim 55\,\mu\mathrm{s}$. Here the absorption probability is on the order of 20 %. These high probabilities make an experiment with continuous photon exposure impossible, so we need an efficient way to switch the photon exposure on and off. We decided to insert a fast spinning chopper disk into the 427 nm pump beam, thereby having no additional losses during the exposure. The chopper disk with 51 mm radius is milled out of an conventional compact disk by our workshop. It has 20 slits with a total duty cycle of $\sim 9\,\%$. The rotation speed was 89 Hz, and the wheel is positioned in the center of an 1 : 1 telescope made of two aspheric lenses with 13.86 mm focal length. The theoretical limit for the rise- and fall time based on these values is then $\sim 0.5\,\mu\mathrm{s}$, the exposure window is $\sim 51\,\mu\mathrm{s}$, followed by a blocking period of $\sim 505\,\mu\mathrm{s}$. To synchronize the state preparation with the photon exposure we detect the remaining pump light with a photo diode behind the SPDC resonator. A detected rising edge of the photo diode was used to generate a trigger signal for the next exposure window. The necessary delay is chosen such that it triggers the preparatory RF- and 729 nm pulses, the preparation is therefore finished at the beginning of the next exposure window.[12] To verify the correct switching we correlate the predicted rising times with the detection of the generated 854 nm SPDC photons. The result is shown in figure 4.7: a rising edge of $\sim 3.5\,\mu\mathrm{s}$, and a falling edge of $\sim 5\,\mu\mathrm{s}$ are measured. One reason for the longer rise time is the disk thickness, whereby the beam cannot be cut perfectly at

[12] The motor, disk and trigger source of this experiment were replaced for later experiments. The new motor (Faulhaber 2232S012BX4S + speed controller SC1801S3530) in combination with a disk machined from a 3.5″ hard disk allow for rotation speeds up to 150 turns per second.

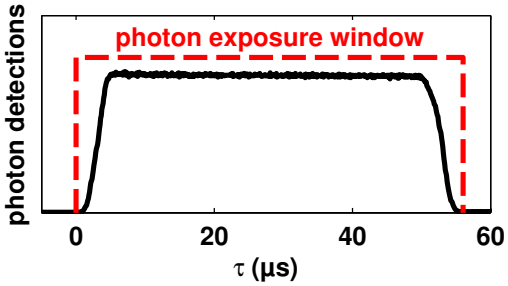

Figure 4.7.: Correlation of the predicted open gate of the chopper with the detected 854 nm photons.

the position of its waist. Another reason is the precision of machining. This induces small deviations in the slit width that cause a additional jitter at the falling edge. The correlation shows that a window of 56 µs covers the whole photon exposure.

Preparatory measurement: 393 nm detection efficiency

The last preparatory measurement concerns the detection efficiency of the 393 nm photons. We prepare the ion in the state $|D_{5/2},\ m = -5/2\rangle$, and switch on a 854 nm laser. The laser pulse is long enough to ensure generation of a 393 nm photon with $> 99\,\%$ probability, from what 0.6 % account for the decay to $D_{3/2}$. The generated circularly-polarized photons are split by the polarizing beam splitter onto $|H\rangle$ in 50 % of the cases and onto $|V\rangle$ in the other 50 %. The comparison of detected 393 nm photons in the two arms with the number of preparations yields the detection efficiency of 0.67(1) % for $|H\rangle$-polarized and 0.46(1) % for $|V\rangle$-polarized 393 nm photons, which includes the collection of the HALO, the detector efficiency, and loss in the optical components.

4.2.1. Pulse sequence

The time line of the sequence is shown in figure 4.8. We start with Doppler cooling, followed by frequency-selective optical pumping to the $|S_{1/2},\ m = -1/2\rangle$ Zeeman sub level by driving the transition from $|S_{1/2},\ m = +1/2\rangle$ to $|D_{5/2},\ m = -3/2\rangle$ with the 729 nm laser, and an additional 854 nm laser. After optical pumping, the ion is in an energy eigenstate, and we are waiting for the aforementioned trigger from the chopper (*c.f.* figure 4.9(a)). The trigger starts an RF $\pi/2$-pulse that generates the superposition of the ion in the ground state (*c.f.* figure 4.9(b)), and the two sub-

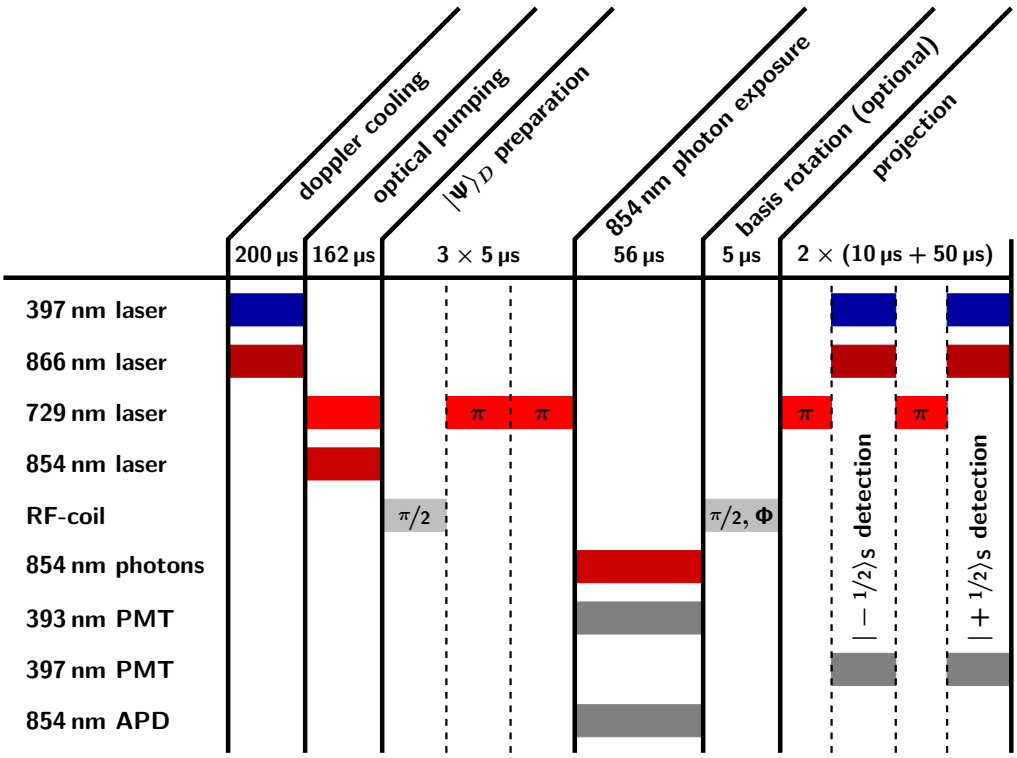

Figure 4.8.: Time line of the experimental sequence.

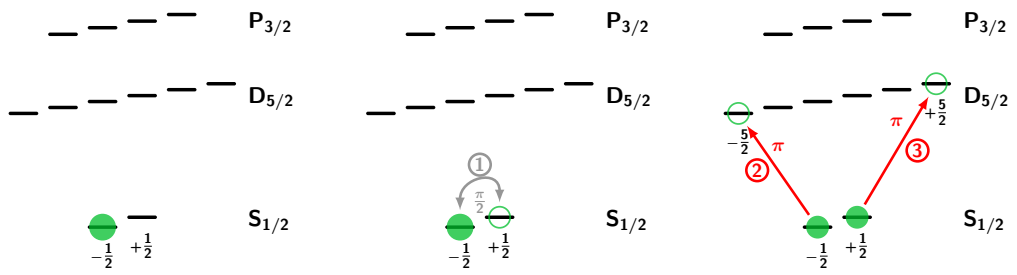

Figure 4.9.: Pulses for coherent generation of the superposition in the $D_{5/2}$ level.

sequent 729 nm π-pulses. One pulse transfers the population from $|S_{1/2},\ m = -1/2\rangle$ to $|D_{5/2},\ m = -5/2\rangle$, and the other one from $|S_{1/2},\ m = +1/2\rangle$ to $|D_{5/2},\ m = +5/2\rangle$ (*c.f.* figure 4.9(c)). Then the 854 nm-photon exposure window starts, and the gate of the 393 nm PMTs and the 854 nm APDs are opened. After the exposure the gates are closed again, and we perform an optional RF $\pi/2$-pulse that rotates the state

for the tomography. The projection is performed in two periods. In the first period we transfer the $|S_{1/2},\ m=-1/2\rangle$ population to $|D_{5/2},\ m=-3/2\rangle$ and perform fluorescence detection with the cooling lasers. In the second period we transfer the $|D_{5/2},\ m=-3/2\rangle$ population back to $|S_{1/2},\ m=-1/2\rangle$, and perform fluorescence detection again. This procedure has the advantage that we can discriminate cycles where no absorption has happened if we detect no fluorescence in both periods. When we detect fluorescence in the first step, then we ignore the second step.

4.2.2. Atomic state reconstruction

To verify the photon-to-atom quantum-state mapping, six input polarizations $\{|H\rangle, |D\rangle, |V\rangle, |A\rangle, |R\rangle, |L\rangle\}$ are prepared and sent to the ion, where the protocol of section 4.1 is applied. For each input polarization a full quantum-state tomography on the atomic ground-state qubit is performed. The procedure to reconstruct the atomic quantum state is explained in the following.

The basis of choice is the natural basis $|-\rangle = |S_{1/2}, m=-1/2\rangle$, $|+\rangle = |S_{1/2}, m=+1/2\rangle$ to represent the qubit. The density matrix

$$\hat{\rho} = \alpha\,|-\rangle\langle-| + \beta\,|+\rangle\langle+| + \gamma\,|-\rangle\langle+| + \gamma^*\,|+\rangle\langle-| = \begin{pmatrix} \alpha & \gamma \\ \gamma^* & \beta \end{pmatrix} \tag{4.20}$$

is then reconstructed by two measurements. In the first one we project onto the eigenstates $|+\rangle$ and $|-\rangle$. As a result we get the diagonal elements of the density matrix

$$\langle-|\,\hat{\rho}\,|-\rangle = \alpha \qquad \langle+|\,\hat{\rho}\,|+\rangle = \beta \tag{4.21}$$

In the second measurement we project onto the superposition states

$$|\Phi\rangle = \frac{1}{\sqrt{2}}\left(|-\rangle + e^{i\Phi}\,|+\rangle\right) \tag{4.22}$$

This is done with the optional RF-$\pi/2$-pulse which rotates the superpositions on the Bloch sphere before we project onto the eigenstates $|\pm\rangle$. In the presented measurements the axis of rotation is fixed, but the phase of the superposition has an additional oscillating part due to the Larmor precession (*c.f.* equation 4.6). We obtain the value of this phase by the time difference between the detection time of the 393 nm herald, and the time of preparation of the initial superposition in $D_{5/2}$. This time difference multiplied by the effective Larmor frequency is the phase difference $\Delta\Phi$ between the superposition and the rotation axis of the $\pi/2$-pulse. The effective Larmor frequency

is given by the energy difference of the two superimposed $|\mathrm{D}_{5/2},\ m = \pm 5/2\rangle$ states and the $|S_{1/2},\ m = \pm 1/2\rangle$ splitting. A phase histogram, as depicted in figure 4.10, of

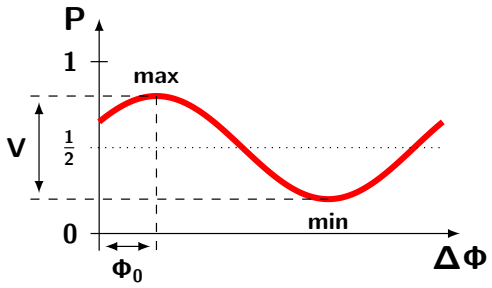

Figure 4.10.: Schematic of the reconstructed probability to detect the ion in $|+\rangle$ (or $|-\rangle$) in dependence of the Larmor phase, measured with the $|+\rangle$ respectively $|-\rangle$ detection events. The sinusoidal curve yields the visibility and offset phase to reconstruct the off-diagonal elements of the atomic density matrix.

the detected events, conditioned on the $|+\rangle$ respectively $|-\rangle$ outcomes, delivers the probabilities for each phase difference. The reconstructed probability in dependence of the phase is in general a sinusoidal curve as depicted in figure 4.10 for each input polarization.

To estimate the background we calculate the time correlation between the 854 nm heralds and the 393 nm, conditioned on the $|+\rangle$ respectively $|-\rangle$ outcome of the projection. This correlation shows a double sided exponential, and we use the average offset at long time differences to estimate the contained number of background events. A detailed description of the background correction, and probability estimation is given in appendix A.1.

A fit on the phase histogram with the periodic function

$$\mathrm{P}\left(V, \Delta\Phi, \Phi_0\right) = \frac{1 + V \cdot \sin\left(\Delta\Phi - \Phi_0\right)}{2} \tag{4.23}$$

yields the visibility V, and the offset phase Φ_0. The phase difference is related to the superposition phase by $\Delta\Phi = \Phi + \pi/2$, which leads to the probability to detect a superposition with phase Φ

$$\mathrm{P}\left(V, \Phi, \Phi_0\right) = \frac{1 + V \cdot \cos\left(\Phi - \Phi_0\right)}{2} \tag{4.24}$$

The expectation values for the superpositions (equation 4.22) with $\Phi = 0$ and $\Phi = \pi/2$

$$\langle \Phi = 0 | \, \hat{\rho} \, | \Phi = 0 \rangle \; = \frac{\alpha + \beta}{2} + \mathrm{Re}\,(\gamma) \qquad \text{and} \qquad \langle \Phi = \pi/2 | \, \hat{\rho} \, | \Phi = \pi/2 \rangle \; = \frac{\alpha + \beta}{2} + \mathrm{Im}\,(\gamma)$$

combined with the measured probabilities at the same phases (equation 4.24)

$$\mathrm{P}\,(V, \Phi = 0, \Phi_0) = \frac{1 + V \cdot \cos(\Phi_0)}{2} \qquad \text{and} \qquad \mathrm{P}\,(V, \Phi = \pi/2, \Phi_0) = \frac{1 + V \cdot \sin(\Phi_0)}{2}$$

lead with $\mathrm{tr}(\rho) = 1$ to the off-diagonal elements of the density matrix

$$\gamma = \mathrm{Re}\,(\gamma) + i \;\; \mathrm{Im}\,(\gamma) = \frac{V}{2} \exp(i\Phi_0) \tag{4.25}$$

Thus the two measurements and equations 4.21, 4.25 allow the reconstruction of the atomic density matrix 4.20.

4.2.3. Quantum-state transfer: Results

To characterize the protocol of the photon-to-atom quantum-state transfer, we reconstruct the quantum process matrix [126]. This is performed by a tomography of the atomic quantum state, after applying the protocol, for several input polarizations of the heralded 854 nm input photons. The atomic quantum state tomography is performed according to section 4.2.2.

Figure 4.11(a-d) shows the measured probabilities of the atomic ground state readout, i.e. to detect the ion in $|S_{1/2}, m = +1/2\rangle$ with and without basis rotation, for six input polarizations $\{|H\rangle_{854}, |D\rangle_{854}, |V\rangle_{854}, |A\rangle_{854}, |R\rangle_{854}, |L\rangle_{854}\}$ after applying the photon-to-atom state mapping protocol. A time window of ± 30 ns is used in which the detection of a herald of absorption at 393 nm and the detection of the 854 nm partner-photon in arm A are counted as a coincidence. This window corresponds to $\sim 85\,\%$ of the original two-photon wave packet.

The 393 nm vertically polarized ($|V\rangle_{393}$) photons are used for mapping the state onto the joint state (*c.f* equation 4.6) because it turned out that the polarizing beam splitter had a bad extinction ratio at the horizontally polarized arm.

Plot 4.11(a) shows the probabilities to detect the ion in $|S_{1/2}, m = +1/2\rangle$ without the optional RF $\pi/2$-pulse, *c.f.* equation 4.21, which corresponds to a measurement in the $|S_{1/2}, m = \pm 1/2\rangle$-basis (diagonal elements α, β). The gray (colored) bars are the data points without (with) background correction. The results are close to the ideal values of 50 % for the linear polarizations and zero, respectively one, for the

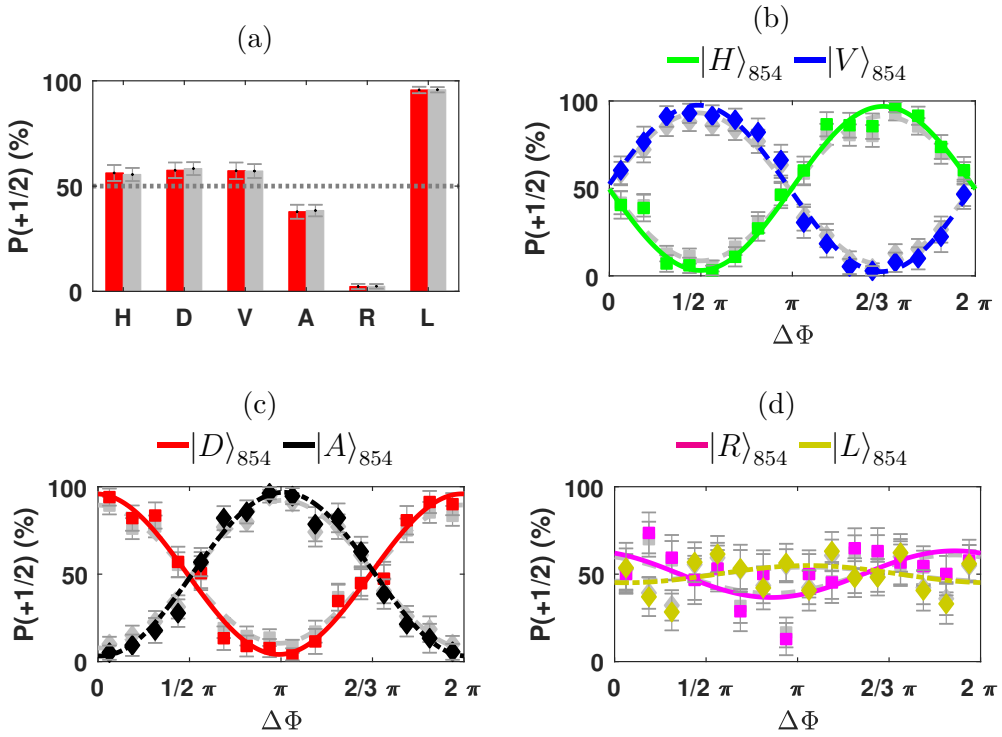

Figure 4.11.: (a) $|S_{1/2}, m = +1/2\rangle$ probabilities without basis rotation ($|S_{1/2}, m = \pm 1/2\rangle$-basis) for the six input polarizations (red bars). The gray bars are without background correction. (b-d) $|S_{1/2}, m = +1/2\rangle$ probabilities in dependence of the phase with basis rotation (superposition basis) for the six input polarizations. The gray dashed lines show the data without background correction:
(b) green (squares): $|H\rangle$, blue (diamonds): $|V\rangle$
(c) red (squares): $|D\rangle$, black (diamonds): $|A\rangle$
(d) magenta (squares): $|R\rangle$, yellow (diamonds): $|L\rangle$

circular polarizations. Plot 4.11(b-d) shows the probabilities to detect the ion in $|S_{1/2}, m = +1/2\rangle$ in dependence of the Larmor phase for the different input polarizations with the optional RF $\pi/2$-pulse for basis rotation. This corresponds to a measurement in the superposition basis (off-diagonal element γ). The gray (colored) points are the data points without (with) background correction. The solid lines are fits with the function 4.23 to extract the visibility V and the phase Φ_0. Phases and visibilities of the histograms are listed in table 4.1. A phase shift of about $\pi/2$ between $|H\rangle$ and $|D\rangle$,

$|D\rangle$ and $|V\rangle$, $|V\rangle$ and $|A\rangle$ is observed. The mean visibility is 93.6 % with background correction and 83 % without. In the $|R\rangle/|L\rangle$ measurement 4.11(c), a small residual oscillation is visible, which ideally should not exist. The reason is a slight rotation of the input polarization, and small polarizing effects of the dielectric mirrors used in the ion setup.

The measured probabilities are fed into a maximum-likelihood algorithm[13] to reconstruct the process χ-matrix [75, 117] shown in figure 4.12, expressed in the basis $\{\mathbb{1}, \sigma_x, \sigma_y, \sigma_z\}$. The identity part of this matrix is identified as process fidelity. With background correction we get $\chi_{(1,1)} = 94.8\,\%$, without any correction we get 89.9 %. From this value, we infer the mean overlap fidelity $\langle F\rangle = (2\,\chi_{(1,1)}+1)/3 = 96.5\,\%$ with background correction, and 93.3 % without background correction. This is in good agreement with the mean of the measured overlap fidelities, $1/6\,\sum_i \langle i|\,\rho_i\,|i\rangle = 96.7(8)\,\%$ with background correction, and 93(3) % without background correction. The major source of infidelity is the coherence decay of the ion due to magnetic field fluctuations during the exposure time of 56 µs.

We now compare the number of detected events with the number of trials to extract the efficiency of the protocol. We repeated the protocol 1.13×10^8 times, which leads to a total exposure time of 1 h45 min. In this time we record in total 7810 detected (background corrected) coincidences between the 854 nm herald and the 393 nm photon. We generated 9.3×10^8 heralded fiber coupled 854 nm photons in this exposure

[13] The maximum likelihood algorithm ensures that the reconstructed process matrix is physical when the matrix is reconstructed with – in general noisy – experimental data.

Table 4.1.: Phase and Visibility of the sinusoidal fits.

	with background correction		without background correction	
input state	Phase (°)	Visibility	Phase (°)	Visibility
$\|H\rangle_{854}$	179(3)	0.94(3)	180(3)	0.83(3)
$\|D\rangle_{854}$	268(3)	0.92(4)	268(3)	0.79(3)
$\|V\rangle_{854}$	357(3)	0.95(2)	357(2)	0.86(3)
$\|A\rangle_{854}$	93(2)	0.94(3)	92(2)	0.84(3)
$\|R\rangle_{854}$	244(23)	0.27(10)	244(23)	0.22(9)
$\|L\rangle_{854}$	101(48)	0.10(8)	101(48)	0.08(7)

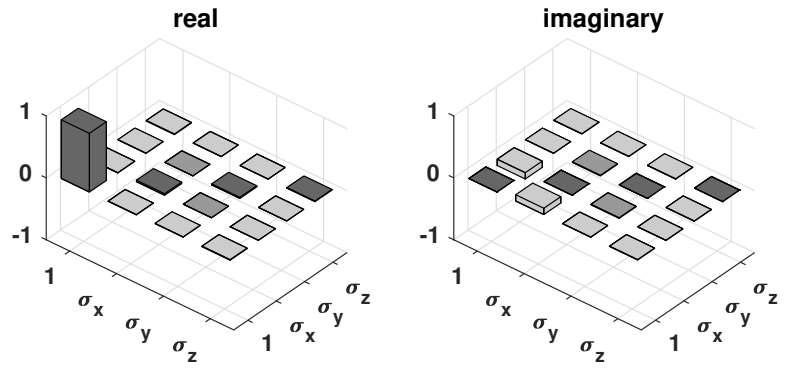

$$\begin{pmatrix} 0.948 & -0.005 & 0.004 & -0.010 \\ -0.005 & 0.025 & -0.000 & -0.001 \\ 0.004 & -0.000 & 0.017 & -0.000 \\ -0.010 & -0.001 & -0.000 & 0.009 \end{pmatrix} \qquad \begin{pmatrix} 0.000 & -0.102 & 0.002 & 0.006 \\ 0.102 & 0.000 & 0.010 & 0.004 \\ -0.002 & -0.010 & 0.000 & 0.005 \\ -0.006 & -0.004 & -0.005 & 0.000 \end{pmatrix}$$

Figure 4.12.: Reconstructed process matrix with background correction. The identity part is 94.8 %.

time. The success probability for a fiber coupled photon is then $\eta = 8.4 \times 10^{-6}$. By extracting the 393 nm detection efficiencies we get an absorption probability of $\eta_{abs} = 7.4 \times 10^{-4}$, which is in good agreement with formerly measured values [92, 96].

4.2.4. Summary

With this experiment we have demonstrated that a defined polarization state of a heralded single photon is successfully mapped onto the atomic ground state qubit. The process fidelity of the heralded photon-to-atom state mapping protocol is determined to $\chi_{(1,1)} = 94.8\,\%$. The major limitation is the coherence time of the atomic superposition due to magnetic field fluctuations. The protocol is used in the next experiments to demonstrate the generation of atom-photon entanglement by heralded absorption of one photon of an entangled photon-photon state.

4.3. Photon-photon to atom-photon entanglement transfer

The photon-to-atom state mapping protocol of section 4.1 is used in this experiment to transfer the polarization-entangled two-photon state of the photon-pair source of chapter 3 to an entangled atom-photon state. In this case the ion acts as a receiver, that is waiting for a photon which has an entangled partner. It is an alternative to the direct generation of atom-photon entanglement as shown in [44].

Two separate measurements are performed: the first one with the photon-pair source presented in section 3.3, whereby the entangled state is generated with a non-polarizing beam-splitter, and the second measurement with the source in interferometric configuration as introduced in section 3.4. Besides the technical differences of the pair generation, that result in differences in the initial two-photon state fidelities, pair rates and scaling of the signal to background ratio, we also generate two different Bell states in the two measurements. In the first case the $|\Psi^+\rangle$ Bell state is generated, and in the second case, with the tunable source, the phase is adjusted to the $|\Psi^-\rangle$ Bell state.

Experiments with polarization qubits are sensitive to changes of the birefringence of the optical fibers that guide the photons from the photon pair source to the atomic setup. Over several days of acquisition time these changes become significant, the effect is a drift of the polarization. This drift can be compensated directly or the measurement basis has to be corrected. In both ways is the two particle-reference frame maintained. For the two experiments, the technical realization of the polarization-basis calibration is done with two different strategies. In the first measurement we use a scheme that corrects the basis with additional reference points. In the second measurement we correct for the polarization drift with a reference laser, and a set of two quarter- and one half waveplates.

The common schematic setup of the two experiments is illustrated in figure 4.13. The photon pair source provides entangled photon pairs in the two output arms. Arm A is connected to a projection stage consisting of a $\lambda/2$, $\lambda/4$ waveplate, a polarizing beam splitter and an avalanche photo diode on each output. The partner photons in arm B are guided with a single mode fiber to the ion setup and focused onto the ion with the HALO. We apply the photon-to-atom state mapping protocol as explained in section 4.1. In this case the results are used to characterize the joint quantum state of photon A and ion after the state mapping.

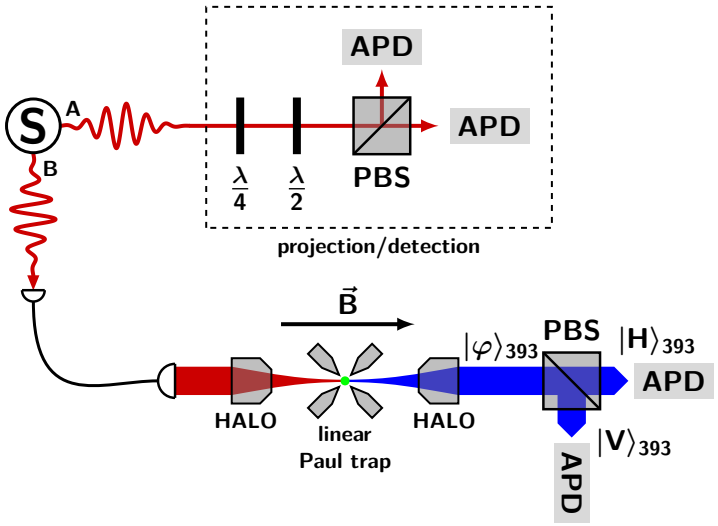

Figure 4.13.: Schematic of the experiment. One of the two arms of the entangled photon pair source is connected to a projection stage, and the other arm to the ion-trap setup.

An overview of the atom-photon state reconstruction is given in section 4.3.1. Section 4.3.2 contains the transfer of the $|\Psi^+\rangle$ Bell state generated by the source of section 3.3. In section 4.3.3 the transfer of the photonic $|\Psi^-\rangle$ Bell state generated by the source in interferometric configuration of section 3.4 onto the combined atom-photon state is demonstrated.

4.3.1. Atom-photon quantum state reconstruction

To reconstruct the two-qubit quantum state a tomographically complete set of measurements is performed [66, 118]. The chosen observables are the 16 tensor products $\{\hat{\sigma}_i \otimes \hat{\sigma}_j | i,j = 0,\ldots,3\}$ of the identity operator and the Pauli spin operators $\{\hat{\sigma}_{0,\ldots,3}\} = \left\{\hat{\mathbb{1}}, \hat{\sigma}_x, \hat{\sigma}_y, \hat{\sigma}_z\right\}$. The expectation values of the underlying density matrix ρ are

$$\langle \hat{\sigma}_i \otimes \hat{\sigma}_j \rangle_\rho = \mathrm{tr}\left(\hat{\sigma}_i \otimes \hat{\sigma}_j \ \rho\right) \tag{4.26}$$

and allow for direct reconstruction of ρ by linear combination

$$\rho = \frac{1}{4} \sum_{i,j=0}^{3} \langle \hat{\sigma}_i \otimes \hat{\sigma}_j \rangle_\rho \cdot \ \hat{\sigma}_i \otimes \hat{\sigma}_j \tag{4.27}$$

We approximate the expectation values by [66]

$$\langle \hat{\sigma}_i \otimes \hat{\sigma}_j \rangle = \lambda_{|0_i\rangle} \cdot P\left(|0_i\rangle\right) \cdot \langle \hat{\sigma}_j \rangle \Big|_{|0_i\rangle} + \lambda_{|1_i\rangle} \cdot P\left(|1_i\rangle\right) \cdot \langle \hat{\sigma}_j \rangle \Big|_{|1_i\rangle} \tag{4.28}$$

where $\lambda_{|0_i\rangle}$, $\lambda_{|1_i\rangle}$ denote the eigenvalues of the observable $\hat{\sigma}_i$, $|0_i\rangle$ and $|1_i\rangle$ are the eigenstates of this observable, and $P\left(|0_i\rangle\right)$ and $P\left(|1_i\rangle\right)$ are the measured probabilities to detect the photonic qubit in the eigenstates of this observable. $\langle \hat{\sigma}_j \rangle \Big|_{|0_i\rangle}$ and $\langle \hat{\sigma}_j \rangle \Big|_{|1_i\rangle}$ are the conditioned expectation values of the atomic qubit after detection of the photonic qubit in the eigenstate $|0_i\rangle$ respectively $|1_i\rangle$. The products are simplified to

$$\left\langle \hat{\mathbb{1}} \otimes \hat{\mathbb{1}} \right\rangle = 1 \tag{4.29}$$

$$\left\langle \hat{\mathbb{1}} \otimes \hat{\sigma}_j \right\rangle = P\left(|0_i\rangle\right) \cdot \langle \hat{\sigma}_j \rangle \Big|_{|0_i\rangle} + P\left(|1_i\rangle\right) \cdot \langle \hat{\sigma}_j \rangle \Big|_{|1_i\rangle} \quad ; \quad i,j = 1,2,3 \tag{4.30}$$

$$\left\langle \hat{\sigma}_i \otimes \hat{\mathbb{1}} \right\rangle = P\left(|0_i\rangle\right) - P\left(|1_i\rangle\right) \quad ; \quad i = 1,2,3 \tag{4.31}$$

$$\langle \hat{\sigma}_i \otimes \hat{\sigma}_j \rangle = P\left(|0_i\rangle\right) \cdot \langle \hat{\sigma}_j \rangle \Big|_{|0_i\rangle} - P\left(|1_i\rangle\right) \cdot \langle \hat{\sigma}_j \rangle \Big|_{|1_i\rangle} \quad ; \quad i,j = 1,2,3 \tag{4.32}$$

The conditioned atomic expectation values $\langle \hat{\sigma}_j \rangle \Big|_{|0_i/1_i\rangle}$ are calculated by reconstructing the atomic density matrix ρ_{at} under the condition of a photon detection in $|0_i/1_i\rangle$ as described in section 4.2.2. The expectation values are then given by $\langle \hat{\sigma}_j \rangle = \mathrm{tr}\left(\hat{\sigma}_j \ \rho_{at}\right)$.

4.3.2. Experiment I : $|\Psi^+\rangle$ - state transfer

The photon pair source described in section 3.3.8 is used in this experiment. The generated photon pairs are split by a non-polarizing beam splitter. The pump power dependence of the state fidelity limits the pump power, and therefore the photon pair rate. As a compromise between state infidelity and measurement time, we decided to use 10 mW, thereby generating the entangled $|\Psi^+\rangle$-state shown in figure 3.23 with a background-corrected fidelity of $\langle \Psi^+ | \, \hat{\rho} \, | \Psi^+ \rangle = 89.7\,\%$. Compared to the photon-to-atom quantum-state transfer measurement (section 4.1) we expect only 21 % of the signal: 42 % reduction due to the lower pump power and 50 % reduction due to the probabilistic splitting of the photon pairs. As a consequence, we expanded the exposure window to 120 µs to increase the absorption probability per window. A drawback is the higher decoherence of the prepared superposition of the ion in $D_{5/2}$ during the time from the preparation until the absorption, and in the mapped superposition in the $S_{1/2}$ from the absorption time to the end of the exposure window. From a Ramsey measurement we infer a coherence time in the $S_{1/2}$

level of 398(10) µs. Calculated from this value we infer a coherence time of the initial $(|\mathrm{D}_{5/2}, \mathrm{m} = -5/2\rangle + |\mathrm{D}_{5/2}, \mathrm{m} = +5/2\rangle)/\sqrt{2}$ superposition of 133 µs due to the threefold higher energy difference of the prepared superposition in $D_{5/2}$. The achievable visibility after 120 µs of exposure time is therefore estimated to 66.4(13) %. The mapping process is thus limited by the coherence of the atomic superposition.

The control over the polarization of both photons after the beam splitter is important to select the correct projection polarization. The photons of the transmitted arm (A) travel in free space, so we do not expect polarization rotations during the experiment. The photons in the reflected arm (B) are guided to the ion with an optical fiber. Variations in the mechanical stress onto the ∼5 m long optical fiber during the several days that the experiment lasts is an error source that must be controlled. A second problem is that we cannot measure the polarization at exactly the position of the ion. The closest position is in front of the vacuum chamber. We do not know if the viewport of the vacuum chamber or the HALO is birefringent. The viewport underlies mechanical stress due to the pressure difference and is a candidate for constant polarization changes. To overcome this problem, we use a laser beam that is sent through the same fiber, and we calibrate the polarization at a reference point in front of the vacuum chamber, by optimizing the ions absorption. The polarization at the reference point is in fixed relation with the polarization at the ion. This relation is used to measure the polarization rotation matrix of the fiber in arm B and to compensate by changing the projector setting of the partner photons in arm A. A detailed explanation of this procedure is given in appendix A.2. The sequence that controls the ion and the photon switching with the optical chopper is similar to section 4.2, the only difference is the exposure time that we have chosen differently for the two experiments.

4.3.2.1. $|\Psi^+\rangle$ - state transfer: Experimental Results

To verify the entanglement between the ion and the parter photon in arm A (*c.f.* figure 4.13), a tomographic set of measurements is performed. Therefore six projector settings $\{|H\rangle_{854}, |D\rangle_{854}, |V\rangle_{854}, |A\rangle_{854}, |R\rangle_{854}, |L\rangle_{854}\}$ are chosen in arm A, and for each projector setting the atomic quantum state is reconstructed according to the explanations in section 4.2.2 with and without the optional atomic basis rotation (RF $\pi/2$-pulse). A time window of ±84 ns is used in which the detection of a herald of absorption at 393 nm and the detection of the 854 nm partner-photon in arm A is counted as a coincidence. This window corresponds to ∼ 99 % of the original two-

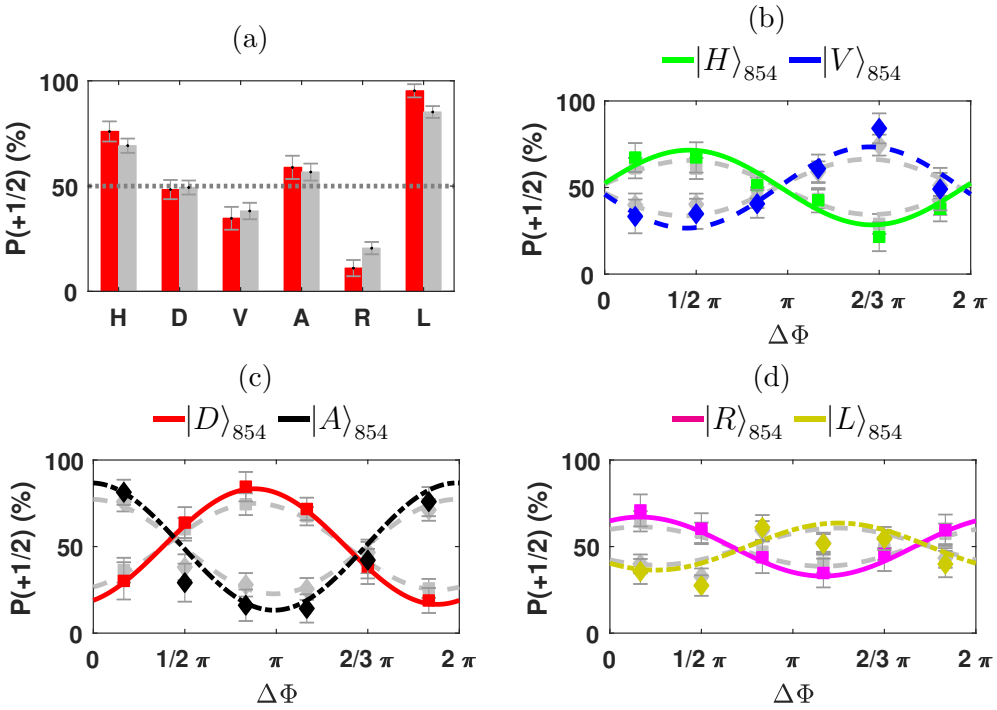

Figure 4.14.: Probabilities, after applying the photon-to-atom state mapping protocol, of the atomic ground state readout, i.e. to detect the ion in $|S_{1/2}, m = +1/2\rangle$ for six projector settings $\{|H\rangle_{854}, |D\rangle_{854}, |V\rangle_{854}, |A\rangle_{854}, |R\rangle_{854}, |L\rangle_{854}\}$ of the partner photon in arm A. (a) Probabilities without basis rotation (red bars). The gray bars are without background correction. (b-d) Probabilities in dependence of the Larmor phase (with basis rotation). The colored (gray) points show the data with (without) background correction. The solid lines are fits to the data. The projection settings for the partner photons are:

(b) green (squares): $|H\rangle_{854}$, blue (diamonds): $|V\rangle_{854}$
(c) red (squares): $|D\rangle_{854}$, black (diamonds): $|A\rangle_{854}$
(d) magenta (squares): $|R\rangle_{854}$, yellow (diamonds): $|L\rangle_{854}$

photon wave packet. The joint atom-photon quantum state is then reconstructed according to section 4.3.1. Figure 4.14(a-d) shows the measured probabilities, after applying the photon-to-atom state mapping protocol, of the atomic ground state readout, i.e. to detect the ion in $|S_{1/2}, m = +1/2\rangle$ with and without basis rotation for six projector settings $\{|H\rangle_{854}, |D\rangle_{854}, |V\rangle_{854}, |A\rangle_{854}, |R\rangle_{854}, |L\rangle_{854}\}$ of the partner photon in arm A. The 393 nm vertically polarized ($|V\rangle_{393}$) photons are used for mapping the

Figure 4.15.: Phase and Visibility of the sinusoidal fits.

projection state	with background correction		without background correction	
	Phase (°)	Visibility	Phase (°)	Visibility
$\|H\rangle_{854}$	353(14)	0.43(11)	353(16)	0.31(9)
$\|D\rangle_{854}$	69(2)	0.67(3)	69(3)	0.50(2)
$\|V\rangle_{854}$	170(16)	0.47(13)	169(17)	0.33(9)
$\|A\rangle_{854}$	268(13)	0.74(15)	268(10)	0.55(9)
$\|R\rangle_{854}$	300(9)	0.34(5)	299(14)	0.23(5)
$\|L\rangle_{854}$	135(38)	0.27(17)	134(35)	0.21(13)

state onto the joint state (*c.f* equation 4.6) because the bad extinction ratio at the horizontally polarized output of the used polarizing beam splitter limits the fidelity too strongly.

Figure 4.14(a) shows the probabilities to detect the ion in $|S_{1/2}, m = +1/2\rangle$ without the optional RF $\pi/2$-pulse, *c.f.* equation 4.21), which corresponds to a measurement in the $|S_{1/2}, m = \pm 1/2\rangle$-basis (to reconstruct the diagonal elements α, β). The red bars are with background correction, and the gray bars without. With some deviation, the values reproduce the ideal result of 50 % for the four linear partner-photon projections, zero for $|R\rangle$, and one for $|L\rangle$.

Figure 4.14(b-d) show the probabilities to detect the ion in $|S_{1/2}, m = +1/2\rangle$ in dependence of the Larmor phase with the optional RF $\pi/2$-pulse for basis rotation. This corresponds to a measurement in the superposition basis (off-diagonal element γ). Shown is one plot for each projector setting of the partner photon in arm A. The colored points show the data with background correction (including a correction for accidental coincidences), the gray points are without background correction. The solid lines are fits to the data with the function 4.23 to extract the visibility V and the phase Φ_0. A phase shift of $\sim \pi/2$ between $|H\rangle$-$|D\rangle$, $|D\rangle$-$|V\rangle$, $|V\rangle$-$|A\rangle$, and $|A\rangle$-$|H\rangle$ is observable. The 58 % mean visibility in the curves with projection of the partner photon onto a linear polarization is mainly limited by the coherence of the ion of 66.4(13) %, and the 89.7 % state fidelity of the two-photon state from the pair source. The curves with circular partner-photon projection still show an oscillation, the reason for this is not completely clear. One possibility is a rotation of the polarization; this is supported by the π phase shift between $|R\rangle$-$|L\rangle$, and the almost equal visibility

of the two curves.

Table 4.2 lists the probabilities to detect the 854 nm partner photon in the eigenstate of the observables $\hat{\sigma}_x$ ($|H\rangle$, $|V\rangle$), $\hat{\sigma}_y$ ($|D\rangle$, $|A\rangle$) and $\hat{\sigma}_z$ ($|R\rangle$, $|L\rangle$). The atom-

Table 4.2.: Probabilities to detect the 854 nm partner photon in the eigenstate of the observables $\hat{\sigma}_x$ ($|H\rangle$, $|V\rangle$), $\hat{\sigma}_y$ ($|D\rangle$, $|A\rangle$) and $\hat{\sigma}_z$ ($|R\rangle$, $|L\rangle$).

$\hat{\sigma}_x$		$\hat{\sigma}_y$		$\hat{\sigma}_z$	
$P(\|H\rangle)$	49.2(25) %	$P(\|D\rangle)$	53.7(26) %	$P(\|R\rangle)$	42.8(23) %
$P(\|V\rangle)$	50.4(25) %	$P(\|A\rangle)$	46.3(26) %	$P(\|L\rangle)$	57.2(23) %

photon quantum state is reconstructed according to section 4.3.1, the resulting density matrix is shown in figure 4.16, expressed in the atomic $\{|0\rangle = |S_{1/2}, m = -1/2\rangle$, $|1\rangle = |S_{1/2}, m = +1/2\rangle\}$ and the photonic $\{|R\rangle, |L\rangle\}$ basis. In this basis, the two-photon state $|\Psi^+\rangle_{H/V,H/V} = (\hat{a}^\dagger_{A,H}\,\hat{a}^\dagger_{B,V} + \hat{a}^\dagger_{A,V}\,\hat{a}^\dagger_{B,H})/\sqrt{2}\,|vac\rangle$ translates after the state mapping of the photon in arm B to $|\Psi^+\rangle_{R/L,0/1} = (\hat{a}^\dagger_{A,R}\,\hat{a}^\dagger_{B,0} - \hat{a}^\dagger_{A,L}\,\hat{a}^\dagger_{B,1})/\sqrt{2}\,|vac\rangle$. We get a fidelity with the maximally entangled $|\Psi^+\rangle$ Bell state of $\langle\Psi^+|\,\hat{\rho}\,|\Psi^+\rangle = 74.6(35)\,\%$. Without background correction we get a fidelity of $\langle\Psi^+|\,\hat{\rho}\,|\Psi^+\rangle = 62.1(23)\,\%$. The inferred purities are $\mathrm{tr}(\rho^2) = 70(5)\,\%$, and $\mathrm{tr}(\rho^2) = 51(3)\,\%$ without correction. The concurrence as a measure of entanglement is $\mathrm{C} = 50(7)\,\%$ with correction, and $\mathrm{C} = 36(5)\,\%$ without. The background in this measurement is higher, which increases the

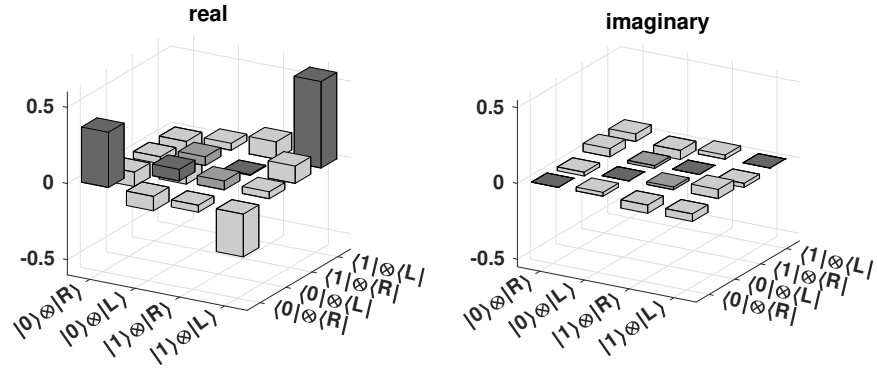

$$\begin{pmatrix} 0.36(2) & -0.09(2) & -0.05(4) & -0.28(3) \\ -0.09(2) & 0.08(2) & 0.06(3) & 0.05(4) \\ -0.05(4) & 0.06(3) & -0.01(2) & 0.11(2) \\ -0.28(3) & 0.05(4) & 0.11(2) & 0.57(2) \end{pmatrix} \qquad \begin{pmatrix} 0 & -0.026(9) & 0.05(2) & 0.05(2) \\ 0.026(9) & 0 & -0.02(2) & -0.06(2) \\ -0.05(2) & 0.02(2) & 0 & 0.027(9) \\ -0.05(2) & 0.06(2) & -0.027(9) & 0 \end{pmatrix}$$

Figure 4.16.: Reconstructed atom-photon density matrix.

accidental coincidences. This is because of the cases where the two photons are not split by the beam splitter. As a consequence we get a higher background correcting factor in the data.

We now compare the number of detected events with the number of trials to extract the efficiency of the protocol. The experiment contains in total $N_{run} = 116 \times 10^6$ runs, which yields, with the 120 µs exposure time per run, a total exposure time of $T_{exp} = 3\,\mathrm{h}52\,\mathrm{min}$. In this time we generated in total $N_{pair} = 12.5 \times 10^9$ photon pairs. We recorded in total $N_C = 3823$ background subtracted coincidences. This leads to the success probability per generated photon-pair to create a detected and entangled atom-photon pair of

$$\eta_{success,pair} = \frac{N_C}{N_{pair}} = 0.31 \times 10^{-6} \tag{4.33}$$

and the success probability per run is

$$\eta_{success,run} = \frac{N_C}{N_{run}} = 33 \times 10^{-6} \tag{4.34}$$

The detection, and fiber-coupling efficiencies of arm A of $\eta_{854} = 5.9\,\%$, and the splitting efficiency of the photons at the non polarizing beam splitter of 50 % lead to $N_{heralded,854} = 728 \times 10^6$ heralded 854 nm photons in the fiber guided to the ion setup. With the measured 393 nm detection efficiency of $\eta_{393} = 1.4\,\%$ ($|H\rangle_{393}$ and $|V\rangle_{393}$) we infer the absorption efficiency per fiber-coupled 854 nm photon to

$$\eta_{abs} = \frac{N_C}{N_{heralded,854}\ \eta_{393}} = 3.8 \times 10^{-4} \tag{4.35}$$

which is lower by a factor of 2 compared to the heralded absorption experiment in section 4.2. The source for this reduction is the beam splitter that splits the photon pairs. In the case where both photons leave the beam splitter at the output B, that is guided to the ion, both photons can be absorbed without creating a coincidence. The probability of having such a absorption is equal to the probability of having an absorption of a photon pair that was split at the beam splitter, and will reduce the number of detected coincidences by a factor of 2.

The mean exposure time ($T_{ent.,mean,det.}$) to generate an entangled and detected atom-photon pair is given by the by the exposure time divided by detected number of coincidences

$$T_{ent.,mean,det.} = \frac{T_{exp}}{N_C} = 3.64\,\mathrm{s} \tag{4.36}$$

When excluding the detection efficiency of arm A ($\sim 30\,\%$) and including the duty cycle of the sequence (exposure time vs. (cooling + preparation + exposure time)

$\approx 20\,\%$) then we generate entangled fiber-coupled atom-photon pairs at a rate of $\sim 0.18\,\mathrm{s}^{-1}$.

4.3.3. Experiment II : $|\Psi^-\rangle$ - state transfer

In this experiment we use the interferometric photon-pair source as described in section 3.4. We pump the source with 44 mW of 427 nm power, and generate $2 \times 10^6\,\mathrm{s}^{-1}$ available entangled photon pairs. The phase of the source was set to the $|\Psi^-\rangle$ Bell state (shown in figure 3.29) with a background-corrected fidelity of $\langle\Psi^-|\,\hat{\rho}\,|\Psi^-\rangle = 98.3(5)\,\%$. The photon-to-atom state-mapping protocol was implemented with the sequence shown in figure 4.17. A new high speed optical chopper[14] was used to switch the photon generation. The benefits of the new chopper are an adjustable duty cycle, a high rotation speed of up to 150 turns per second, and home-build electronics based on an FPGA that predict the next open window with $< 1\,\mu\mathrm{s}$ precision. The main

[14]Faulhaber: Motor 2232S012BX4S + speed controller SC1801S3530

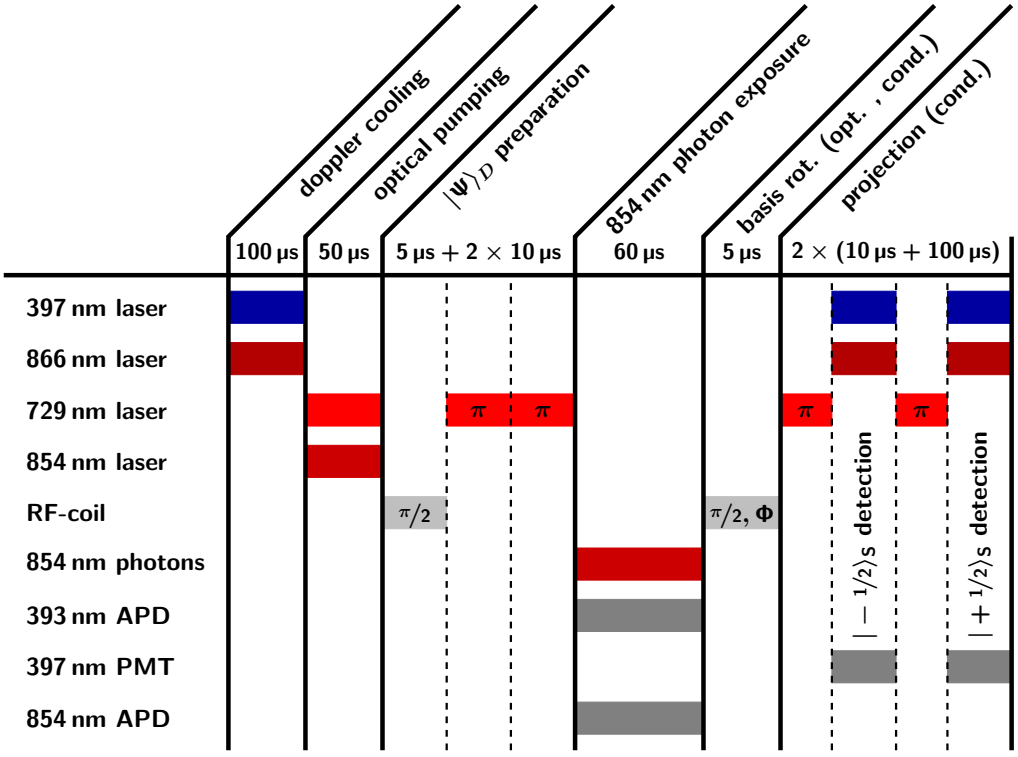

Figure 4.17.: The time line of the experimental sequence.

change in the sequence is the 854 nm exposure time to 60 µs, and that the atomic state readout is conditioned on the detection of a 393 nm herald. This increases the duty cycle of the exposure time to 21 %, and the repetition rate to $\sim 4000\,\mathrm{s}^{-1}$.

For this experiment, we used an improved projection setup for the 393 nm photons. The polarizing beam splitter was replaced by a Wollaston prism[15] that separates both polarizations with an extinction ratio $> 1 \times 10^5$, and two APDs with $\eta_{det} \approx 55\,\%$ detection efficiency were used. The transmission of the optical components in the 393 nm projection path is $\eta_{loss,393} \approx 90\,\%$. With the collection efficiency of the HALO η_σ for σ-transitions we get an ideal detection efficiency of $\eta_\sigma\,\eta_{det}\,\eta_{loss,393} = 2.97\,\%$. The measured detection efficiency for the σ-polarized emission pattern of the ion is 2.25 % (both detectors) with this setup, the difference to the ideal value arise from optical loss in the HALO and view port and imaging aberrations.

The polarization characteristic of arm B, that guides the photons to the ion setup, was monitored in intervals of $\sim$ 1-2 h with a reference laser. This beam is coupled with a flip-mirror behind the ion-trap and detected with a polarimeter using an additional flip-mirror in front of the photon pair source (*c.f.* figure 3.25). By sending right-circularly- and horizontally polarized light we compensate for rotations with a set of two quarter-, and one half-waveplate.

4.3.3.1. $|\Psi^-\rangle$ - state transfer: Experimental Results

To verify the entanglement between the ion and the parter photon in arm A (*c.f.* figure 4.13), a tomographic set of measurements is performed. Therefore six projector settings $\{|H\rangle_{854},\ |D\rangle_{854},\ |V\rangle_{854},\ |A\rangle_{854},\ |R\rangle_{854},\ |L\rangle_{854}\}$ are chosen in arm A, and for each projector setting the atomic quantum state is reconstructed according to the explanations in section 4.2.2 with and without the optional atomic basis rotation (RF $\pi/2$-pulse). A time window of ± 30 ns is used in which the detection of a herald of absorption at 393 nm and the detection of the 854 nm partner-photon in arm A are counted as a coincidence. This window corresponds to $\sim$ 85 % of the original two-photon wave packet. The joint atom-photon quantum state is then reconstructed according to section 4.3.1. A summary of the measured probabilities after applying the photon-to-atom state mapping protocol in arm A is shown in figure 4.18. The probabilities of the atomic ground state readout, i.e. to detect the ion in $|S_{1/2}, m = +1/2\rangle$ with and without basis rotation, conditioned on the projector settings $\{|H\rangle_{854},\ |D\rangle_{854},\ |V\rangle_{854},\ |A\rangle_{854},\ |R\rangle_{854},\ |L\rangle_{854}\}$ of the partner photon in arm A. The

[15] Thorlabs, WP10-A

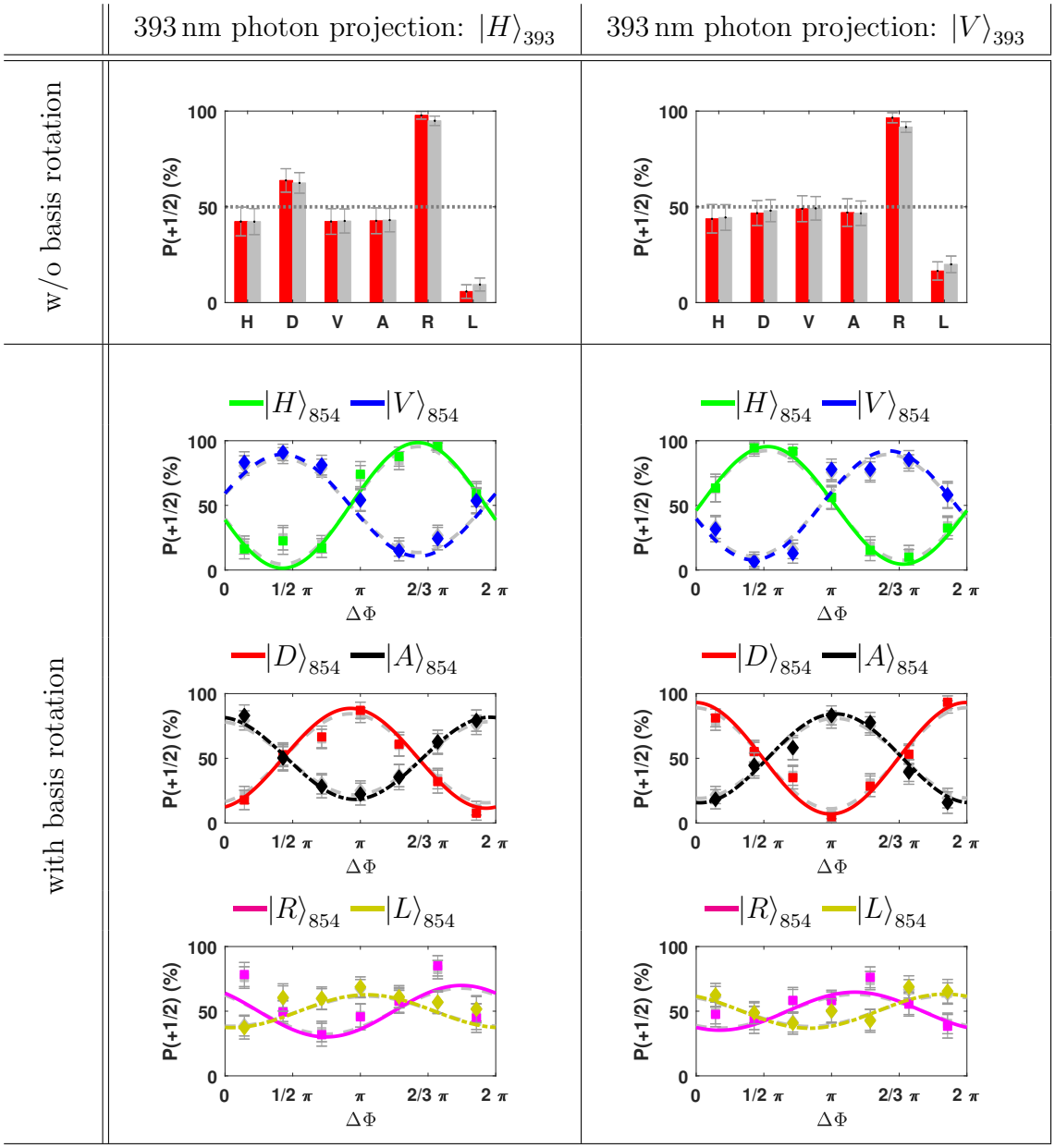

Figure 4.18.: The probabilities of the atomic ground state readout, i.e. to detect the ion in $|S_{1/2}, m = +1/2\rangle$ with and without basis rotation, conditioned on the projector settings $\{|H\rangle_{854}, |D\rangle_{854}, |V\rangle_{854}, |A\rangle_{854}, |R\rangle_{854}, |L\rangle_{854}\}$ of the partner photon in arm A and conditioned on the projection of the heralding 393 nm photon onto $\{|H\rangle_{393}, |V\rangle_{393}\}$.

probabilities are also conditioned on the projection of the heralding 393 nm photon onto $\{|H\rangle_{393}, |V\rangle_{393}\}$.

The data without the optional basis rotation (figure 4.18 top) shows the probabilities to detect the ion in $|S_{1/2}, m = +1/2\rangle$ without the optional RF $\pi/2$-pulse, *c.f.* equation 4.21), which corresponds to a measurement in the $|S_{1/2}, m = \pm 1/2\rangle$-basis (to reconstruct the diagonal elements α, β). The red bars are with background correction, and the gray bars without. With some deviation, the values reproduce the ideal result of 50 % for the four linear partner-photon projections, one for $|R\rangle$, and zero for $|L\rangle$.

The data with the optional basis rotation (figure 4.18 bottom) shows the probabilities to detect the ion in $|S_{1/2}, m = +1/2\rangle$ in dependence of the Larmor phase with the optional RF $\pi/2$-pulse. This corresponds to a measurement in the superposition basis (off-diagonal element γ). The colored points show the data with background correction (including correction for accidental coincidences), the gray points are without background correction. The solid lines are fits to the data with the function 4.23 to extract the visibility V and the phase Φ_0. The data with projection of the partner photon onto a linear polarization show high contrast. The plots with circularly-polarized projection shows a small residual oscillation. The π phase shift between the oscillations with horizontal and vertical projection of the 393 nm photon is clearly visible. A summary of the phases and visibilities is given in table 4.4.

Table 4.5 lists the probabilities to detect the 854 nm partner photon in the eigenstate of the observables $\hat{\sigma}_x$ ($|H\rangle$, $|V\rangle$), $\hat{\sigma}_y$ ($|D\rangle$, $|A\rangle$) and $\hat{\sigma}_z$ ($|R\rangle$, $|L\rangle$).

With the probabilities we reconstruct the density matrix as explained in section 4.3.1. The evaluation is separately done for the two projection measurement outcomes $|H\rangle_{393}$ and $|V\rangle_{393}$ of the herald of absorption. The corresponding density matrices are shown in figure 4.19 and 4.20, expressed in the atomic $\{|0\rangle = |S_{1/2}, m = -1/2\rangle$, $|1\rangle = |S_{1/2}, m = +1/2\rangle\}$ and the photonic $\{|R\rangle, |L\rangle\}$ basis. In this basis, the two-photon state $|\Psi^-\rangle_{H/V,H/V} = (\hat{a}^\dagger_{A,H}\,\hat{a}^\dagger_{B,V} - \hat{a}^\dagger_{A,V}\,\hat{a}^\dagger_{B,H})/\sqrt{2}\,|vac\rangle$ translates after the state mapping of the photon in arm B to $|\Psi^-\rangle_{R/L,0/1} = (\hat{a}^\dagger_{A,L}\,\hat{a}^\dagger_{B,0} - \hat{a}^\dagger_{A,R}\,\hat{a}^\dagger_{B,1})/\sqrt{2}\,|vac\rangle$. Conditioned on the $|H\rangle_{393}$ herald we get an overlap fidelity with (without) background correction with the maximally entangled $|\Psi^-\rangle$ Bell state of $\langle\Psi^-|\,\rho\,|\Psi^-\rangle = 86.5(34)\,\%$ ($81.5(32)\,\%$) with a purity of $\mathrm{tr}(\rho^2) = 81.7(57)\,\%$ ($73.0(49)\,\%$), and the concurrence $\mathrm{C} = 74.3(68)\,\%$ ($66.3(63)\,\%$). Conditioned on the $|V\rangle_{393}$ herald we get a fidelity of $\langle\Psi^-|\,\rho\,|\Psi^-\rangle = 86.0(37)\,\%$ ($80.5(33)\,\%$) with a purity of $\mathrm{tr}(\rho^2) = 77.3(61)\,\%$ ($68.50(506)\,\%$), and the concurrence $\mathrm{C} = 67(5)\,\%$ ($61.3(51)\,\%$).

The fidelity of the two-photon state (98.3(5) %, background corrected), and the process fidelity ($\chi_{(1,1)} = 94.8\,\%$, background corrected) of the mapping protocol in

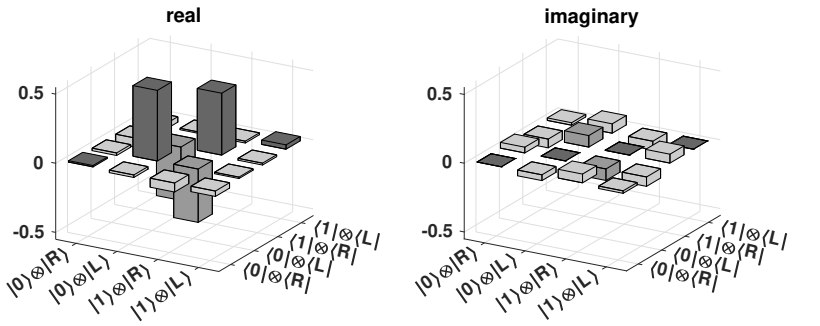

$$\begin{pmatrix} 0.01(2) & -0.02(3) & -0.07(5) & -0.04(3) \\ -0.02(3) & 0.51(2) & -0.39(3) & -0.01(5) \\ -0.07(5) & -0.39(3) & 0.45(2) & -0.01(3) \\ -0.04(3) & -0.01(5) & -0.01(3) & 0.03(2) \end{pmatrix} \quad \begin{pmatrix} 0 & 0.04(4) & -0.06(4) & 0.02(2) \\ -0.04(3) & 0 & 0.08(8) & 0.07(7) \\ 0.06(6) & -0.08(6) & 0 & -0.06(4) \\ -0.02(1) & -0.07(5) & 0.06(6) & 0 \end{pmatrix}$$

Figure 4.19.: Reconstructed atom-photon density matrix matrix with the 393 nm herald projected onto $|H\rangle_{393}$.

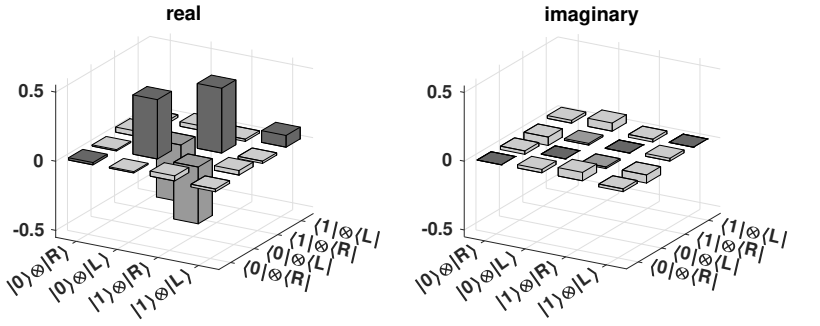

$$\begin{pmatrix} 0.02(2) & 0.01(3) & 0.04(3) & -0.02(3) \\ 0.01(3) & 0.43(2) & -0.41(3) & 0.03(3) \\ 0.04(3) & -0.41(3) & 0.47(2) & -0.02(3) \\ -0.02(3) & 0.03(3) & -0.02(3) & 0.08(2) \end{pmatrix} \quad \begin{pmatrix} 0 & -0.02(2) & -0.06(4) & 0.02(2) \\ 0.02(2) & 0 & 0.01(1) & 0.06(6) \\ 0.06(6) & -0.01(1) & 0 & -0.02(1) \\ -0.02(1) & -0.06(4) & 0.02(2) & 0 \end{pmatrix}$$

Figure 4.20.: Reconstructed atom-photon density matrix with the 393 nm herald projected onto $|V\rangle_{393}$.

Table 4.4.: Phase and Visibility of the fringes conditioned on $|S_{1/2}, m = +1/2\rangle$.

393 nm projector	854 nm projector	with correction		without correction	
		Phase (°)	Visibility	Phase (°)	Visibility
$\|H\rangle_{393}$	$\|H\rangle_{854}$	167(8)	0.97(10)	167(8)	0.91(11)
$\|H\rangle_{393}$	$\|D\rangle_{854}$	77(8)	0.77(8)	77(8)	0.69(7)
$\|H\rangle_{393}$	$\|V\rangle_{854}$	346(10)	0.79(12)	346(10)	0.73(12)
$\|H\rangle_{393}$	$\|A\rangle_{854}$	262(5)	0.63(5)	262(5)	0.57(4)
$\|H\rangle_{393}$	$\|R\rangle_{854}$	224(35)	0.40(24)	224(36)	0.36(22)
$\|H\rangle_{393}$	$\|L\rangle_{854}$	99(29)	0.25(12)	99(30)	0.23(11)
$\|V\rangle_{393}$	$\|H\rangle_{854}$	5(4)	0.91(5)	4(5)	0.85(5)
$\|V\rangle_{393}$	$\|D\rangle_{854}$	269(8)	0.86(8)	269(8)	0.78(8)
$\|V\rangle_{393}$	$\|V\rangle_{854}$	166(11)	0.84(13)	166(11)	0.79(13)
$\|V\rangle_{393}$	$\|A\rangle_{854}$	95(7)	0.69(8)	95(7)	0.62(7)
$\|V\rangle_{393}$	$\|R\rangle_{854}$	121(25)	0.29(12)	121(26)	0.26(11)
$\|V\rangle_{393}$	$\|L\rangle_{854}$	241(23)	0.26(11)	241(22)	0.24(9)

Table 4.5.: Probabilities to detect the 854 nm partner photon in the eigenstate of the observables $\hat{\sigma}_x$ ($|H\rangle$, $|V\rangle$), $\hat{\sigma}_y$ ($|D\rangle$, $|A\rangle$) and $\hat{\sigma}_z$ ($|R\rangle$, $|L\rangle$).

		$\|H\rangle_{393}$	$\|V\rangle_{393}$
$\hat{\sigma}_x$	$P(\|H\rangle)$	46.8(22) %	49.3(22) %
	$P(\|V\rangle)$	53.2(22) %	50.7(22) %
$\hat{\sigma}_y$	$P(\|D\rangle)$	52.3(20) %	54.5(19) %
	$P(\|A\rangle)$	47.7(20) %	45.5(19) %
$\hat{\sigma}_z$	$P(\|R\rangle)$	45.8(20) %	48.6(19) %
	$P(\|L\rangle)$	54.2(20) %	51.4(19) %

section 4.2 let us expect a higher value of 92.7 %. For this measurement, however, the photon exposure time was set to 60 µs, and the process fidelity is mainly limited by decoherence due to magnetic field fluctuations. Furthermore we found that the magnetic field noise situation changed between the two measurements. We infer a maximum process fidelity of 89.1(6) % from the visibility of a Ramsey measurement.

Together with the 98.3(5) % photon-state fidelity we expect the final state fidelity to be 87.3(11) %, which is in good agreement with the measured value.

We now compare the number of runs with the number of detected events to extract the efficiency and rate of the protocol. A time window of ±60 ns is used in which the detection of a herald of absorption at 393 nm and the detection of the 854 nm partner-photon in arm A are counted as a coincidence. This window corresponds to $\sim$ 97 % of the original two-photon wave packet. In total we accumulated $N_{run} = 150.77 \times 10^6$ measurement runs (with one exposure time per run) and recorded $N_c = 6197$ coincident events between a 393 nm herald and a 854 nm photon. The success probability per exposure time $\eta_{success,run}$ is then

$$\eta_{success,run} = \frac{N_c}{N_{run}} = 41.1 \times 10^{-6} \tag{4.37}$$

The total exposure time $T_{tot,exposure}$ is 9346 s $\approx$ 2.51 h, calculated by the product of N_{run} and the exposure window of 60 µs. With the pair rate per pump power, $4.5(5) \times 10^4$ /(s mW), and the pump power of 44 mW we get the total number of generated pairs in $T_{tot,exposure}$, $N_{pairs} = 18.5 \times 10^9$. The success probability per pair for the protocol is then

$$\eta_{success,pair} = \frac{N_c}{N_{pair}} = 0.33 \times 10^{-6} \tag{4.38}$$

The detection efficiency of the 854 nm photons in arm A including APD quantum efficiency, spectral filters, fibers, and all other optical components, is $\eta_{854,A} = 4.9\,\%$. The total coupling efficiency from the photon pair source to the ion setup in front of the vacuum chamber is $\eta_{854,B} = 30\,\%$. The measured 393 nm detection efficiency is $\eta_{393} = 2.25\,\%$. The remaining part is the absorption efficiency η_{abs}. We calculate this probability by dividing $\eta_{success,pair}$ by the known efficiencies and get

$$\eta_{abs} = \frac{\eta_{success,pair}}{\eta_{854,A}\ \eta_{854,B}\ \eta_{393}} = 1.0 \times 10^{-3} \tag{4.39}$$

The mean exposure time ($T_{ent.,mean,det.}$) to generate a an entangled and detected atom-photon pair is given by the by the exposure time divided by detected number of coincidences

$$T_{ent.,mean,det.} = \frac{T_{exp}}{N_C} = 1.51\,\text{s} \tag{4.40}$$

When excluding the detection efficiency of arm A ($\sim$ 30 %) and including the duty cycle of the sequence (exposure time vs. (cooling + preparation + exposure time) $\approx$ 25 %) then we generate entangled fiber-coupled atom-photon pairs at a rate of $\sim 0.55\,\text{s}^{-1}$.

4.3.4. Summary

The two experiments demonstrate the generation of atom-photon entanglement by heralded absorption of one photon of an entangled photon-photon state. In the first experiment, the photon-pair source presented in section 3.3 was used. A fidelity with the maximally entangled $|\Psi^+\rangle$ Bell state of $\langle\Psi^+|\,\hat{\rho}\,|\Psi^+\rangle = 74.6(35)\,\%$ ($62.1(23)\,\%$ without background correction) was measured. In this experiment we generated entangled atom-photon pairs at a rate of $\sim 0.18\,\mathrm{s}^{-1}$. In the second experiment, the source in interferometric configuration as introduced in section 3.4 was used. The phase was adjusted to the $|\Psi^-\rangle$ Bell state and a fidelity with the maximally entangled $|\Psi^-\rangle$ Bell state of $\langle\Psi^-|\,\hat{\rho}\,|\Psi^-\rangle = 86.5(34)\,\%$ ($81.5(32)\,\%$ without background correction) was measured. In this experiment we generated entangled atom-photon pairs at a rate of $\sim 0.55\,\mathrm{s}^{-1}$. The higher fidelity and threefold higher rate in the second experiment show the advantage of the interferometric photon-pair source. The major limitation of both experiments is the coherence time of the atomic superposition, and the efficiency of the photon-to-atom state mapping protocol of $\sim 2.09 \times 10^{-5}$. These two numbers have a large potential for improvements for example by the use of optical resonators to increase the atom-photon coupling and a magnetic field shielding. Despite the low efficiency both experiments show relatively large fidelities. This demonstrates the advantages of the heralded protocol.

4.4. Atom to photon quantum-state teleportation

The underlying principle of the quantum state teleportation [47] lies in the nonclassical correlations of the four Bell states. A brief explanation of the general teleportation scheme is given in the following, and later adapted to the atom-photon setup. The four Bell states are defined as

$$|\Phi^{\pm}\rangle_{i,j} = \frac{1}{\sqrt{2}}\Big(|0\rangle_i \otimes |0\rangle_j \pm |1\rangle_i \otimes |1\rangle_j\Big) \qquad |\Psi^{\pm}\rangle_{i,j} = \frac{1}{\sqrt{2}}\Big(|0\rangle_i \otimes |1\rangle_j \pm |1\rangle_i \otimes |0\rangle_j\Big) \tag{4.41}$$

between two particles i and j. The protocol starts with the distribution of a pair of particles that are prepared in one of the Bell states, for example $|\Psi^-\rangle_{1,2}$. Particle 1 is sent to location A and the partner is sent to location B. At position B a third particle with an unknown qubit state $|\varphi\rangle_3$ carries the information in the unknown amplitudes α and β that we want to transmit to location A. The joint state of the three particles is first given by

$$|\Psi^-\rangle_{1,2} \otimes |\varphi\rangle_3 = \frac{1}{\sqrt{2}}\Big(|0\rangle_1 \otimes |1\rangle_2 - |1\rangle_1 \otimes |0\rangle_2\Big) \;\otimes\; (\alpha\,|0\rangle_3 + \beta\,|1\rangle_3)$$

With the definition of the Bell states of equation 4.41 between particle 2 and 3 we transform the joint state to

$$\begin{aligned} |\Psi^-\rangle_{1,2} \otimes |\varphi\rangle_3 = \frac{1}{2}\Big(& (\alpha\,|0\rangle_1 - \beta\,|1\rangle_1) \otimes |\Psi^+\rangle_{2,3} \\ & - (\alpha\,|0\rangle_1 + \beta\,|1\rangle_1) \otimes |\Psi^-\rangle_{2,3} \\ & + (\beta\,|0\rangle_1 - \alpha\,|1\rangle_1) \otimes |\Phi^+\rangle_{2,3} \\ & - (\beta\,|0\rangle_1 + \alpha\,|1\rangle_1) \otimes |\Phi^-\rangle_{2,3} \;\Big) \end{aligned} \tag{4.42}$$

A projective measurement of particles 2 and 3 onto one of the Bell states projects the state of particle 1 to an intermediate state, which is related via a simple transformation

Table 4.6.

Bell state	Intermediate	Operation			Final
$\|\Psi^-\rangle_{2,3}$	$-(\alpha\,\|0\rangle_1 + \beta\,\|1\rangle_1)$	$-(\|0\rangle\langle 0\| + \|1\rangle\langle 1\|)$	$=$	$-\mathbb{1}$	$\rightsquigarrow$ $\alpha\,\|0\rangle_1 + \beta\,\|1\rangle_1$
$\|\Phi^-\rangle_{2,3}$	$-(\beta\,\|0\rangle_1 + \alpha\,\|1\rangle_1)$	$-(\|0\rangle\langle 1\| + \|1\rangle\langle 0\|)$	$=$	$-\sigma_x$	$\rightsquigarrow$ $\alpha\,\|0\rangle_1 + \beta\,\|1\rangle_1$
$\|\Phi^+\rangle_{2,3}$	$\beta\,\|0\rangle_1 - \alpha\,\|1\rangle_1$	$\|1\rangle\langle 0\| - \|0\rangle\langle 1\|$	$=$	$-i\,\sigma_y$	$\rightsquigarrow$ $\alpha\,\|0\rangle_1 + \beta\,\|1\rangle_1$
$\|\Psi^+\rangle_{2,3}$	$\alpha\,\|0\rangle_1 - \beta\,\|1\rangle_1$	$\|0\rangle\langle 0\| - \|1\rangle\langle 1\|$	$=$	σ_z	$\rightsquigarrow$ $\alpha\,\|0\rangle_1 + \beta\,\|1\rangle_1$

to the original state $|\varphi\rangle_3$ of particle 3. Detection of a Bell state reveals no information about the teleported state and the measurement outcome is the classical information which has to be transmitted to location A. Table 4.6 summarizes the projective measurement outcomes, and the transformations to complete the teleportation.

4.4.1. Atom to photon quantum-state teleportation: Protocol

The protocol is now adapted to the atom-photon system. The photon-pair source produces the state

$$|\Psi^-\rangle_{A,B} = \frac{1}{\sqrt{2}} \left(|R\rangle_A |L\rangle_B - |L\rangle_A |R\rangle_B\right) \tag{4.43}$$

of the photons in the two arms A and B. The photon in arm B is guided to the atom, which carries the quantum information, that we want to teleport onto the partner photon in arm A, in a superposition of the Zeeman levels $|\pm 5/2\rangle_D = |\mathrm{D}_{5/2},\ m = \pm 5/2\rangle$,

$$|\varphi\rangle_D = \alpha\, |-5/2\rangle_D + \beta\, |+5/2\rangle_D \tag{4.44}$$

with the amplitudes α and β. The joint product state of the photon pair and the atom is then

$$|\Psi^-\rangle_{A,B} \otimes |\varphi\rangle_D = \frac{1}{\sqrt{2}} \left(|R\rangle_A |L\rangle_B - |L\rangle_A |R\rangle_B\right) \otimes \left(\alpha\, |-5/2\rangle_D + \beta\, |+5/2\rangle_D\right) \tag{4.45}$$

With the definition of the Bell states between the 854 nm photon in arm B, and the atomic $\mathrm{D}_{5/2}$ state

$$\begin{aligned} |\Phi^\pm\rangle_{B,D} &= \frac{1}{\sqrt{2}} \left(|R\rangle_B |-5/2\rangle_D \pm |L\rangle_B |+5/2\rangle_D\right) \\ |\Psi^\pm\rangle_{B,D} &= \frac{1}{\sqrt{2}} \left(|R\rangle_B |+5/2\rangle_D \pm |L\rangle_B |-5/2\rangle_D\right) \end{aligned} \tag{4.46}$$

we rewrite the joint state to

$$\begin{aligned} |\Psi^-\rangle_{A,B} \otimes |\varphi\rangle_D = \frac{1}{2}\Big(& \left(\alpha\, |R\rangle_A - \beta\, |L\rangle_A\right) \otimes |\Psi^+\rangle_{B,D} \\ & - \left(\alpha\, |R\rangle_A + \beta\, |L\rangle_A\right) \otimes |\Psi^-\rangle_{B,D} \\ & + \left(\beta\, |R\rangle_A - \alpha\, |L\rangle_A\right) \otimes |\Phi^+\rangle_{B,D} \\ & - \left(\beta\, |R\rangle_A + \alpha\, |L\rangle_A\right) \otimes |\Phi^-\rangle_{B,D} \Big) \end{aligned} \tag{4.47}$$

In analogy to table 4.6 we see that we have to apply one of the transformations $\{-\mathbb{1}, -\sigma_x, -i\,\sigma_y, \sigma_z\}$ on the photon in arm A to complete the teleportation after the

projection onto one of the four Bell states between the photon in arm B and the atomic state. The Bell state measurement on the atom and the photon in arm B is performed by the heralded absorption process (see section 4.2) and subsequent projection of the 393 nm Raman photon onto the linear polarizations

$$|H\rangle_{393} = \frac{|R\rangle_{393} + |L\rangle_{393}}{\sqrt{2}} \qquad |V\rangle_{393} = \frac{|R\rangle_{393} - |L\rangle_{393}}{i\sqrt{2}} \tag{4.48}$$

and projection of the $S_{1/2}$ Zeeman levels onto the superpositions

$$|+\rangle_S = \frac{|-1/2\rangle_S + |+1/2\rangle_S}{\sqrt{2}} \qquad |-\rangle_S = \frac{|-1/2\rangle_S - |+1/2\rangle_S}{i\sqrt{2}} \tag{4.49}$$

In more detail, this is explained as follows: with the Raman process operator (*c.f.* equation 4.3)

$$\hat{\mathrm{R}}_{B,D} = \quad |L\rangle_{393}\,|-1/2\rangle_S\,\langle R|_B\,\langle -5/2|_D \quad + \quad |R\rangle_{393}\,|+1/2\rangle_S\,\langle L|_B\,\langle +5/2|_D$$

we rewrite the four eigenstates of the measurement

$$\begin{aligned} (\,\langle H|_{393}\,\langle +|_S\,)\;\hat{\mathrm{R}}_{B,D} &= \frac{1}{\sqrt{2}}\,\langle \Phi^+|_{B,D} \\ (\,\langle V|_{393}\,\langle -|_S\,)\;\hat{\mathrm{R}}_{B,D} &= \frac{1}{\sqrt{2}}\,\langle \Phi^+|_{B,D} \end{aligned} \tag{4.50}$$

$$\begin{aligned} (\,\langle H|_{393}\,\langle -|_S\,)\;\hat{\mathrm{R}}_{B,D} &= \frac{i}{\sqrt{2}}\,\langle \Phi^-|_{B,D} \\ (\,\langle V|_{393}\,\langle +|_S\,)\;\hat{\mathrm{R}}_{B,D} &= \frac{1}{i\sqrt{2}}\,\langle \Phi^-|_{B,D} \end{aligned} \tag{4.51}$$

We see that the two results 4.50 project onto $|\Phi^+\rangle_{B,D}$, and the two results 4.51 project onto $|\Phi^-\rangle_{B,D}$, and that there is no projection onto $|\Psi^\pm\rangle_{B,D}$. The reason for this is that the absorption process happens in 50 % of the cases. This is most easily seen when the ion is in one of the $|\pm 5/2\rangle_D$ states, because then it only absorbs one circular polarization. This is a general restriction independent of the initial $|\varphi\rangle_D$ state, such that there is no absorption in 50 % of the cases. This lowers the efficiency of the protocol by the same factor. A possible scheme to increase the efficiency and identify all possible Bell states of B and D would be by sending the 854 nm photon first parallel to the magnetic field, and then a second time anti-parallel. Thereby the polarization mapping onto the $\sigma^\pm$-transitions reverses, and we project onto the $|\Psi^\pm\rangle_{B,D}$ states at the second passage.

4.4.2. Atom to photon quantum-state teleportation: Results

To verify the teleportation protocol, we prepare atomic states that we would like to teleport

$$|\varphi\rangle_D = \alpha\,|{-5/2}\rangle_D + \beta\,|{+5/2}\rangle_D\ , \tag{4.52}$$

send the entangled photon pairs, perform the heralded absorption protocol as explained in section 4.4.1, and carry out a tomography on the polarization qubit in arm A by repeating each measurement with a projection on $|H\rangle_{854}/|V\rangle_{854}$, $|D\rangle_{854}/|A\rangle_{854}$, and $|R\rangle_{854}/|L\rangle_{854}$. A time window of ± 30 ns is used in which the detection of a herald of absorption at 393 nm and the detection of the 854 nm target photon in arm A are counted as a coincidence. This window corresponds to $\sim 85\,\%$ of the original two-photon wave packet.

We use the two atomic energy eigenstates $|{-5/2}\rangle_D$, $|{+5/2}\rangle_D$, and the superpositions $\left(|{-5/2}\rangle_D + e^{i\,\phi}\,|{+5/2}\rangle_D\right)/\sqrt{2}$ as input states. The superposition phase ϕ is given by the Larmor precession frequency multiplied with the time between the preparation of a superposition (with fixed phase) and the detection of the 393 nm heralding Raman photon. We therefore probe the teleportation scheme with a different but known phase

Table 4.7.: Summary of phase and visibility of the data in figure 4.21.

393 nm projector	854 nm projector	with correction		w/o correction	
		Phase	Visibility	Phase	Visibility
$\|-\rangle_S\,\|H\rangle_{393}$	$\|H\rangle_{854}$	342(7)	0.95(9)	342(7)	0.88(9)
	$\|D\rangle_{854}$	265(8)	0.67(8)	265(7)	0.59(6)
	$\|R\rangle_{854}$	55(38)	0.4(3)	55(38)	0.3(2)
$\|+\rangle_S\,\|V\rangle_{393}$	$\|H\rangle_{854}$	357(7)	0.89(8)	357(7)	0.83(8)
	$\|D\rangle_{854}$	268(8)	0.84(8)	268(8)	0.75(8)
	$\|R\rangle_{854}$	109(19)	0.27(9)	109(18)	0.24(7)
$\|+\rangle_S\,\|H\rangle_{393}$	$\|H\rangle_{854}$	171(9)	0.8(1)	171(9)	0.7(1)
	$\|D\rangle_{854}$	75(5)	0.75(6)	75(5)	0.67(5)
	$\|R\rangle_{854}$	268(34)	0.3(2)	268(34)	0.2(1)
$\|-\rangle_S\,\|V\rangle_{393}$	$\|H\rangle_{854}$	178(7)	0.86(7)	178(7)	0.80(8)
	$\|D\rangle_{854}$	95(10)	0.7(1)	95(10)	0.65(9)
	$\|R\rangle_{854}$	246(40)	0.2(2)	246(41)	0.2(2)

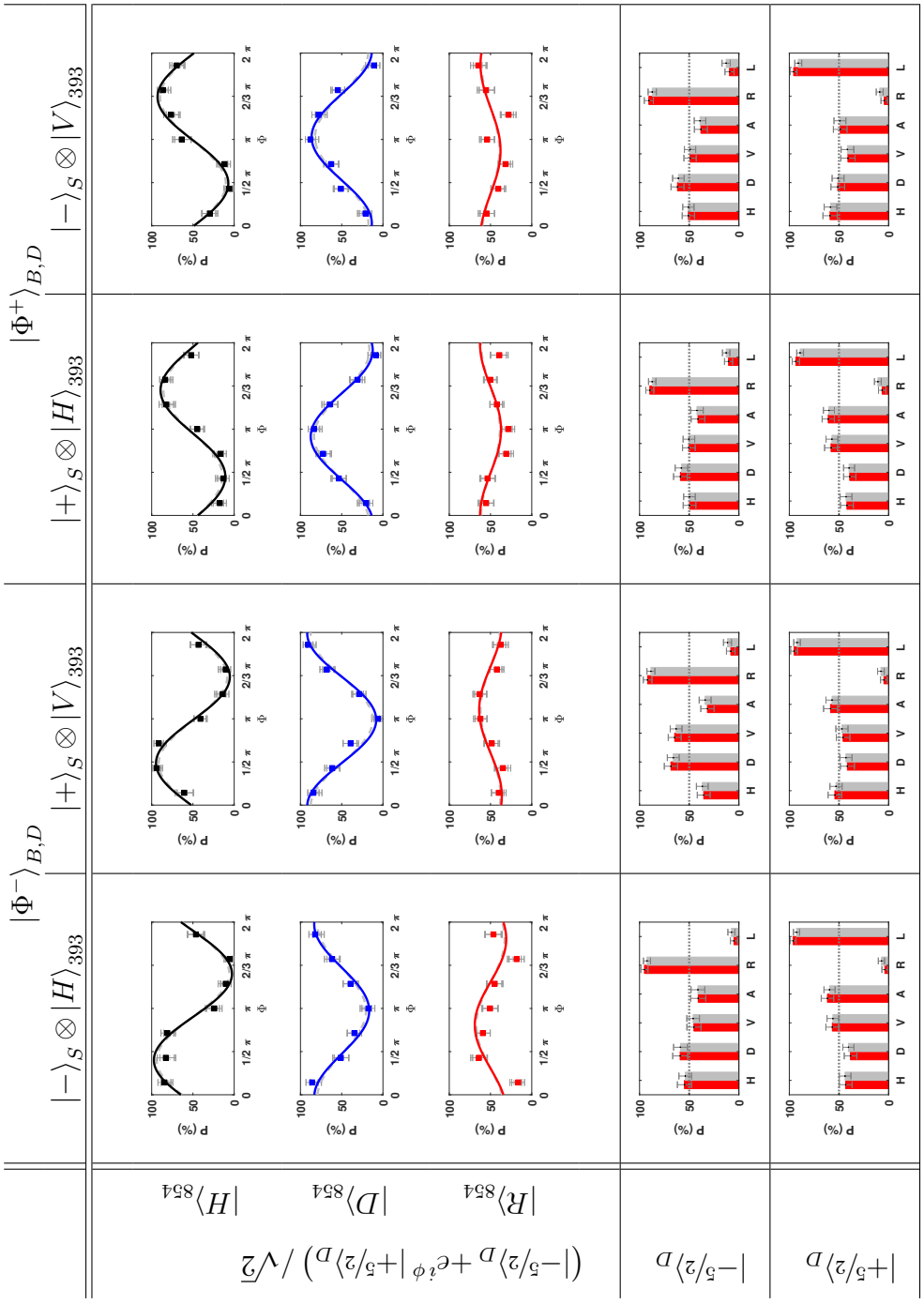

Figure 4.21.: Measured probabilities of the projection measurements for the two Bell-measurement outcomes and the three input states.

in each repetition. Thus we obtain a histogram of correlated events of Bell-state measurement and partner-photon polarization in dependence of the reconstructed phase for the photonic state tomography. A summary of the measurement data is shown in figure 4.21. Plotted are the probabilities to detect the different projection states of the 854 nm photon in arm A conditioned on the result of the atom-photon Bell-state measurement for the different input states $|\varphi\rangle_D$. The colored points show the data with background correction (including correction for accidental coincidences), the gray points are without background correction. The solid lines are fits to the data with the function 4.24 to extract the visibility V and the phase Φ_0. A high contrast in the data for the initial superposition states is observed when we project the 854 nm photon in arm A onto the linear polarizations $|H\rangle_{854}/|V\rangle_{854}$ and $|D\rangle_{854}/|A\rangle_{854}$. When projecting onto the circular polarizations $|R\rangle_{854}/|L\rangle_{854}$ we observe a small remaining oscillation, a sign of a slightly rotated basis, or polarizing effects. A π phase shift between the cases when we project on $|\Phi^-\rangle_{B,D}$, and $|\Phi^+\rangle_{B,D}$ is also observed. A summary of phase and contrast for each measurement is given in table 4.7. The measurements with the energy eigenstates $|\pm 5/2\rangle_D$ as input of the teleportation show the tendency to 50 % when projecting on a linear polarization, and a high contrast when projecting onto the circular polarizations. One can see that $|-5/2\rangle_D$ is teleported to the target photon A with $|R\rangle_A$ polarization, and $|+5/2\rangle_D$ is teleported to $|L\rangle_A$.

The data is fed into a maximum likelihood algorithm to reconstruct the quantum process matrices from the input state $|\varphi\rangle_D$ and the output state of the photon in arm A. This is done separately for the four results of the combined projection on atomic state in $S_{1/2}$ and 393 nm heralding photon. The reconstructed matrices are shown in figure 4.22. We see that either a σ_x or σ_y rotation needs to be applied on the target photon to reveal the prepared input state. The corresponding entries in the process matrix are referred to as process fidelities. The mean process fidelity is 86.1(30) %, and 81.1(29) % without background correction. The mean overlap fidelity of the final states of the photon in arm A with the input state is 89.6(46) %, and 86.2(47) % without correction.

In total we accumulated $N_{run} = 225.55 \times 10^6$ measurement runs (with one exposure window per run) and recorded $N_c = 9094$ coincident events between a 393 nm herald and a 854 nm photon. A time window of ± 60 ns is used for this estimation in which the detection of a herald of absorption at 393 nm and the detection of the 854 nm partner-photon in arm A are counted as a coincidence. This window corresponds to ~ 97 % of the original two-photon wave packet.

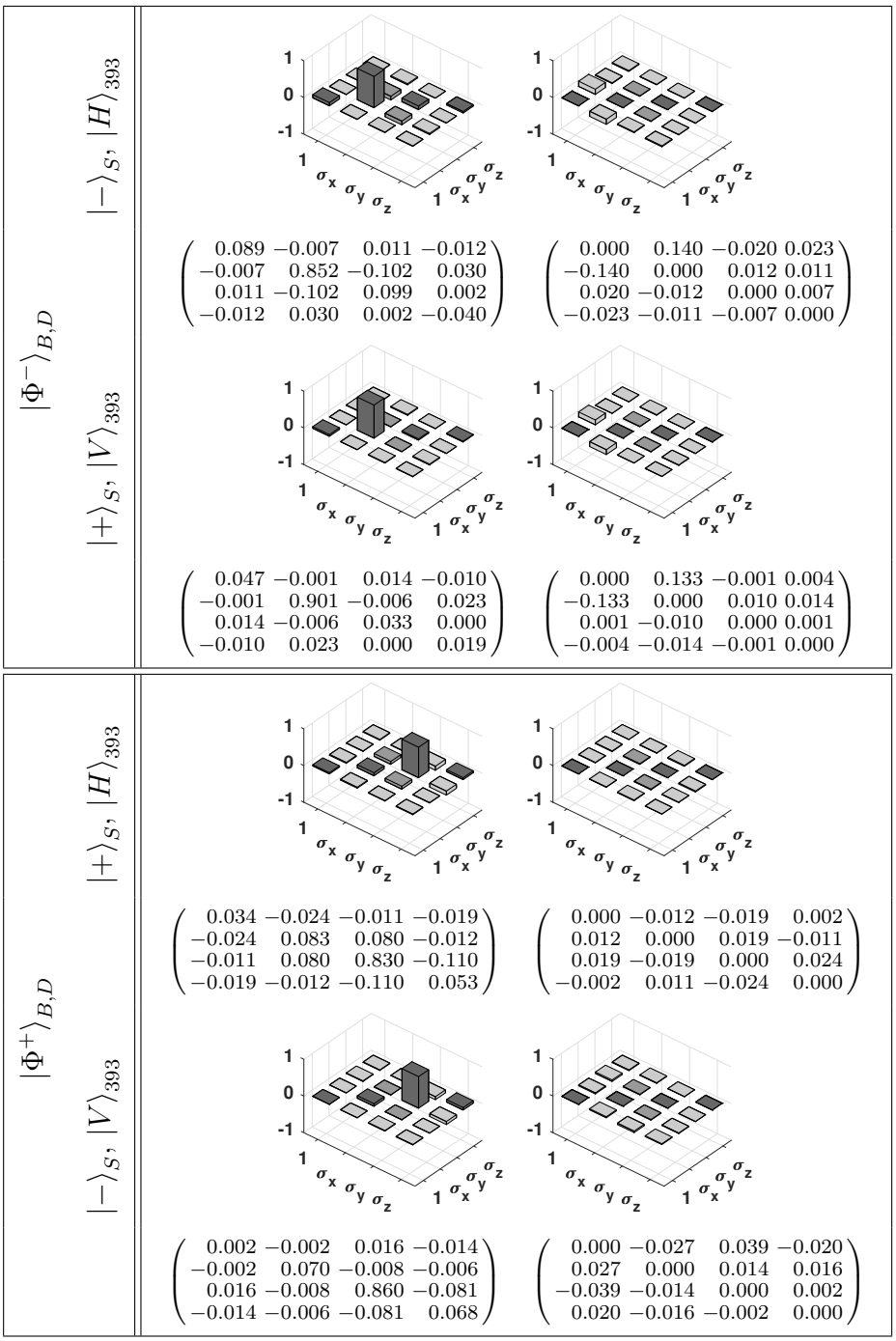

$$\begin{pmatrix} 0.089 & -0.007 & 0.011 & -0.012 \\ -0.007 & 0.852 & -0.102 & 0.030 \\ 0.011 & -0.102 & 0.099 & 0.002 \\ -0.012 & 0.030 & 0.002 & -0.040 \end{pmatrix} \quad \begin{pmatrix} 0.000 & 0.140 & -0.020 & 0.023 \\ -0.140 & 0.000 & 0.012 & 0.011 \\ 0.020 & -0.012 & 0.000 & 0.007 \\ -0.023 & -0.011 & -0.007 & 0.000 \end{pmatrix}$$

$$\begin{pmatrix} 0.047 & -0.001 & 0.014 & -0.010 \\ -0.001 & 0.901 & -0.006 & 0.023 \\ 0.014 & -0.006 & 0.033 & 0.000 \\ -0.010 & 0.023 & 0.000 & 0.019 \end{pmatrix} \quad \begin{pmatrix} 0.000 & 0.133 & -0.001 & 0.004 \\ -0.133 & 0.000 & 0.010 & 0.014 \\ 0.001 & -0.010 & 0.000 & 0.001 \\ -0.004 & -0.014 & -0.001 & 0.000 \end{pmatrix}$$

$$\begin{pmatrix} 0.034 & -0.024 & -0.011 & -0.019 \\ -0.024 & 0.083 & 0.080 & -0.012 \\ -0.011 & 0.080 & 0.830 & -0.110 \\ -0.019 & -0.012 & -0.110 & 0.053 \end{pmatrix} \quad \begin{pmatrix} 0.000 & -0.012 & -0.019 & 0.002 \\ 0.012 & 0.000 & 0.019 & -0.011 \\ 0.019 & -0.019 & 0.000 & 0.024 \\ -0.002 & 0.011 & -0.024 & 0.000 \end{pmatrix}$$

$$\begin{pmatrix} 0.002 & -0.002 & 0.016 & -0.014 \\ -0.002 & 0.070 & -0.008 & -0.006 \\ 0.016 & -0.008 & 0.860 & -0.081 \\ -0.014 & -0.006 & -0.081 & 0.068 \end{pmatrix} \quad \begin{pmatrix} 0.000 & -0.027 & 0.039 & -0.020 \\ 0.027 & 0.000 & 0.014 & 0.016 \\ -0.039 & -0.014 & 0.000 & 0.002 \\ 0.020 & -0.016 & -0.002 & 0.000 \end{pmatrix}$$

Figure 4.22.: Maximum likelihood reconstruction of the quantum process matrices for the four combined projections, that project onto the $|\Phi\pm\rangle_{B,D}$ Bell states.

The success probability per exposure time $\eta_{success,run}$ is then

$$\eta_{success,run} = \frac{N_c}{N_{run}} = 40.3 \times 10^{-6} \tag{4.53}$$

The total exposure time $T_{tot,exposure}$ is 13 533 s $\approx$ 3.75 h, calculated by the product of N_{run} and the exposure window of 60 µs. With the pair rate per pump power, $4.5(5) \times 10^4$ /(s mW), and the pump power of 44 mW we get the total number of generated pairs in $T_{tot,exposure}$, $N_{pairs} = 26.8 \times 10^9$. The success probability per pair for the teleportation protocol is then

$$\eta_{success,pair} = \frac{N_c}{N_{pair}} = 0.34 \times 10^{-6} \tag{4.54}$$

The detection efficiency of the 854 nm photons in arm A including APD quantum efficiency, spectral filters, fibers, and all other optical components, is $\eta_{854,A} = 4.9\,\%$. The total coupling efficiency from the photon pair source to the ion setup in front of the vacuum chamber is $\eta_{854,A} = 30\,\%$. The 393 nm (both polarizations together) detection efficiency is measured to $\eta_{393} = 2.25\,\%$. The remaining part is the absorption efficiency η_{abs}. We calculate this probability by dividing $\eta_{success,pair}$ by the known efficiencies and get

$$\eta_{abs} = \frac{\eta_{success,pair}}{\eta_{854,A}\ \eta_{854,B}\ \eta_{393}} = 1.0 \times 10^{-3} \tag{4.55}$$

The absorption probability per photon is in good agreement with former measured values [92, 96].

4.4.3. Summary

In this experiment an atomic quantum state was teleported onto the polarization of one photon of an entangled pair, which offers an alternative to direct mapping for quantum state readout. The required resource of entanglement was provided by the photon pair source in interferometric configuration as introduced in section 3.4. And the Bell state measurement on the atom and the photon in arm B was performed by the heralded absorption process (see section 4.2) and subsequent projection of the 393 nm Raman photon and the atomic ground state. With the implemented protocol we project on two of the four Bell states $|\Phi^{\pm}\rangle_{B,D}$. A mean overlap fidelity of the final photonic states with the input state was determined to 89.6(46) % (86.2(47) % without background correction). The efficiency of a single run, e.g to teleport an

input state, was measured to $\eta_{success,run} = 40.3 \times 10^{-6}$. The main limitation of the protocol is the coherence of the atomic superposition, which is the coherence time of the initial qubit.

4.5. Long haul entanglement distribution

State of the art quantum systems, such as single trapped ions, and nitrogen or silicon vacancy centers in diamond, that are possible candidates as quantum nodes in a large scale quantum network, have the relevant transitions often in the visible or the near-infrared regime. The variety of possible systems require strategies to interconnect these dissimilar quantum systems to a common bus wavelength. Quantum frequency conversion is such a technology that converts the wavelength of a photonic qubit by preserving its quantum properties. Choosing the bus wavelength in one of the so-called telecom bands, ranging from 1260 nm to 1675 nm, has the advantage of the low loss in standard optical fibers for long-distance telecommunication. Figure 4.23 illustrates the attenuation coefficient in dependence of the wavelength. As an example we look at

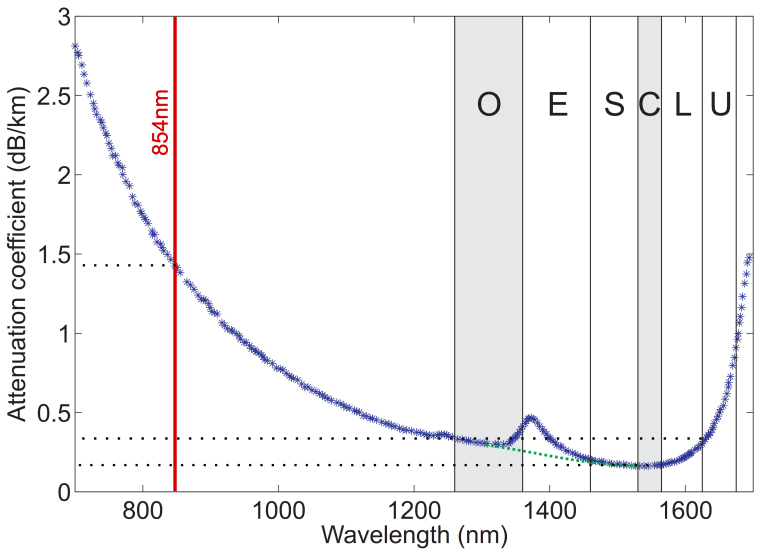

Figure 4.23.: Attenuation of optical single-mode fibers in dependence of the wavelength. Fibers with reduced OH-content show the attenuation of the green line. Indicated are the bands: O (original), E (extended), S (short wavelength), C (conventional), L (long wavelength), U (ultralong wavelength) (Origin: [69, 108])

the attenuation at 854 nm, which is a relevant interfacing transition of the $^{40}Ca^{+}$-ion. The loss at this wavelength is about 1.4 dB/km, while at telecom wavelength it reaches below 0.3 dB/km. A converter with a total efficiency of 25 %, which is demonstrated with current technologies, already pays off at $\sim$ 6 km transmission length.

This section reports briefly about the connection of the entangled photon-pair source of section 3.4, that produces frequency degenerate photon-pairs at 854 nm, to a telecom wavelength in the O-band via polarization-maintaining quantum frequency conversion. This experiment demonstrates the preservation of entanglement by the conversion process.

The converter was build and operated by our colleagues in the group of Christoph Becher, mainly by Andreas Lenhard and Matthias Bock. In the following a brief introduction to the device is given, more details are found in the dissertation [69] and the recent publication [44]. The conversion is based on three-wave mixing in a periodically poled Lithium-Niobate waveguide. As depicted in figure 4.24, difference frequency generation is used. By mixing the 854 nm photons with a strong pump at

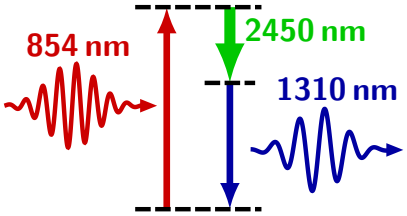

Figure 4.24.: Difference frequency mixing scheme of the conversion process.

2450 nm, the conversion is stimulated and photons at 1310 nm are generated, in the center of the telecom O-band. To obtain polarization-independent conversion, the interferometric setup of figure 4.25 is implemented. An incoming 854 nm photon is split into its polarization amplitudes by a polarizing beam splitter. The horizontally-polarized part is rotated to vertical, and both amplitudes are converted by the same waveguide, but in opposite directions. The originally horizontal part is back-rotated to horizontal polarization before overlapping it with the originally vertical amplitude on a second polarizing beam splitter. A dielectric bandpass filter and a fiber Bragg grating with a linewidth of 25 GHz are used in the 1310 nm arm for background reduction of the conversion process down to $\sim$ 12 photons/s. A chopped 854 nm laser is used to stabilize the whole interferometer. The efficiency of the converter is determined to 26.5 % from the input fiber to the output fiber.

The photon pair source in interferometric configuration of section 3.4 was used. We pumped with 10 mW of 427 nm laser light, and the phase was set to the $|\Psi^+\rangle$ Bell state, which was generated with a fidelity of $\langle\Psi^+|\,\rho_{854}\,|\Psi^+\rangle = 97\,\%$, a purity of $\mathrm{tr}(\rho_{854}^2) = 94.2\,\%$, and a concurrence of $\mathrm{C} = 94.4\,\%$, after background correction

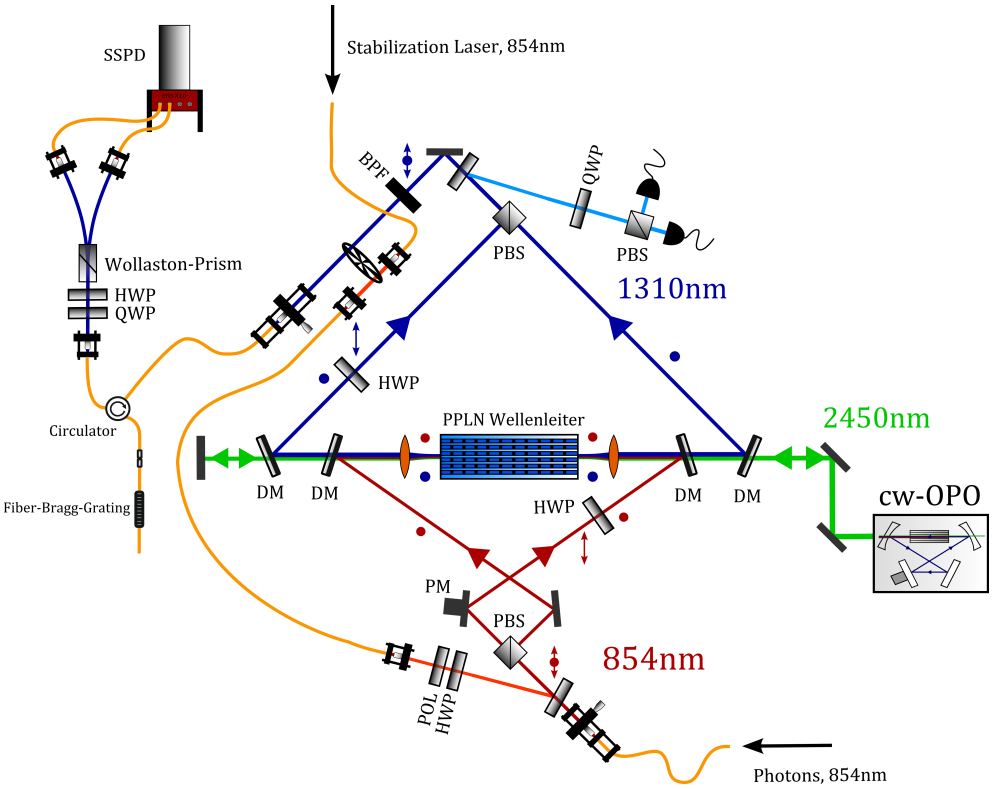

Figure 4.25.: Schematic of the converter. Description of the optical components: polarizer (POL), $\lambda/2$ wave-plate (HWP), $\lambda/4$ wave-plate (QWP), dichroic mirror (DM), piezo-movable mirror (PM), band-pass filter (BPF), superconducting single-photon detector (SSPD).(Origin: Matthias Bock)

(including accidental coincidences). One of the photons was sent to a projection stage in our laboratory, and the partner photon was sent through 90 m of single-mode fiber to the laboratory where the converter is installed. The linking fiber was not actively stabilized and crosses the lobby, another lab, and a maintenance duct on its way from the ground floor to the basement of the building. The polarization stability of this fiber was measured before and is surprisingly high, the peak-to-peak drift of a linear polarization was < 23 mrad on the Poincaré-sphere, recorded in 10 h [69]. In the other lab we converted the photons to 1310 nm and detect them with a projection setup, using superconducting nano-wire detectors (SSPD). The reconstructed density matrix is shown in figure 4.26. The fidelity is determined to $\langle\Psi^+|\,\rho_{1310}\,|\Psi^+\rangle = 91.2\,\%$, a purity to $\mathrm{tr}(\rho^2_{1310}) = 84.6\,\%$, and the concurrence to $C = 86.1\,\%$, with applied

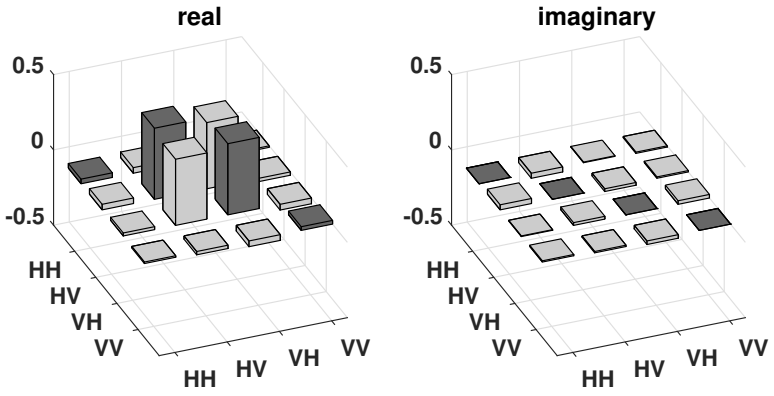

$$\begin{pmatrix} 0.03 & 0.04 & 0.02 & -0.01 \\ 0.04 & 0.47 & 0.44 & -0.02 \\ 0.02 & 0.44 & 0.47 & -0.04 \\ -0.01 & -0.02 & -0.04 & 0.02 \end{pmatrix} \begin{pmatrix} 0.00 & -0.03 & 0.00 & -0.01 \\ 0.03 & 0.00 & -0.02 & 0.01 \\ -0.00 & 0.02 & 0.00 & 0.02 \\ 0.01 & -0.01 & -0.02 & 0.00 \end{pmatrix}$$

Figure 4.26.: Reconstructed two-photon density matrix after conversion of one photon of a pair to 1310 nm.

background correction. This is a clear sign of the polarization-preserving properties of the converter. The observed reduction is mainly due to a mismatch of the two projection bases. Recent measurements of this device have shown a process fidelity of the conversion of 99.75(18) % [44].

5. Conclusions

The work of four generations of PhD students [61–64] has already been spent on advancing this quantum network experiment since it started at ICFO in Spain in 2004. Since the experiment moved to Saarbrücken in 2010, the experimental toolbox was extended by coherent control operations and a set of quantum interfaces [65–67, 70, 73, 75]. The results presented in this thesis extend the set of quantum interfaces on the 854 nm transition of the $^{40}Ca^{+}$ ion with the generation of atom-photon entanglement via an entangled photon-pair source. Also the quantum state readout of the atom by teleportation to a photon is demonstrated. A major part of this thesis is the setup and characterization of the photon-pair source (chapter 3), which combines the SPDC process with an optical resonator for spectral optimization and with an interferometer for the generation of entangled $|\Psi\rangle$ Bell-states with adjustable phase. The resulting $^{40}Ca^{+}$-resonant pair rate per pump power is $4.5(5)\times10^{4}/(\mathrm{s\,mW})$ for up to 40 mW available pump power, and overlap fidelities with the ideal Bell state above 98 % (with background subtraction, including accidental coincidences). These numbers are competitive with state of the art results for each of the combined technologies [93–97] . The unavoidable scaling of the signal to background ratio of cw-pumped SPDC-sources, and its effect on the detected state fidelity for an unbiased observer is discussed.

The new quantum network experiments reported in chapter 4 include the mapping of a polarization-qubit onto the $^{40}Ca^{+}$ quantum node with a process fidelity of 94.8 %. Furthermore, the generation of atom-photon entanglement by heralded absorption of one photon of an entangled photon pair is demonstrated. An overlap fidelity of 86.5(34) % with a maximal entangled Bell-state, and a concurrence of 74.3(68) % are achieved. The generation rate of fiber-coupled atom-photon pairs was determined to $\sim 0.55\,\mathrm{s}^{-1}$. Quantum-state teleportation from a node qubit to a photon is demonstrated with a process fidelity of 86.1(3) %. The implemented Bell-state measurement uses the heralded absorption process and allows the discrimination of the two $|\Phi^{\pm}\rangle$ states. All these protocols are realized for the first time. Finally the connection of the photon-pair source to a telecom wavelength by quantum frequency conversion, as required for

long-haul communication, is presented.

The parallel work of my colleagues on the interfaces at 854 nm include the generation of node-photon entanglement at 854 nm by single-photon emission from the $^{40}Ca^{+}$ ion and subsequent quantum frequency conversion to a telecom wavelength at 1310 nm [44, 72, 73]. A direct mapping scheme of the node qubit onto an 854 nm polarization qubit is presented in [73], and the effect of detuning on the phase of a mapped qubit is investigated in [74, 75].

Outlook

The two critical numbers for the implementation of a quantum network are the qubit rate and the qubit fidelity. The presented entangled photon-pair source offers high values for both, almost at the intrinsic limitation of continuously pumped SPDC sources, which is set by the decrease of the signal-to-background ratio with the generated pair rate. But there is still room to improve and optimize the photon-pair source for its use in quantum network experiments with the $^{40}Ca^{+}$ ion. The first is to improve the background-corrected fidelity. The main reason for the degradation seem to be back-reflections inside the SPDC resonator. A small angle of the crystal surfaces should solve this problem, whereby the reflections are no longer coupled to the counter-propagating mode. The scaling of the signal-to-background ratio can be optimized by increasing the bandwidth of the photons, the limitation being the linewidth of the $^{40}Ca^{+}$ ion of $2\pi \times 22.5\,\mathrm{MHz}$. Reducing the loss of the photons from its generation to the fiber coupling is one possibility to increase the rate. By removing the compensation crystal one can decrease the loss inside the resonator by a factor of two. As a consequence one gets a photon-pair escape probability of about 81.5 % instead of 67 %. Also the spatial overlap of the two interferometer arms is not yet at its absolute optimum. A better beam shaping and a beam guidance could improve the coupling efficiency in each arm by approximately 25 %. The higher escape probability and coupling will lead to almost a twofold improvement of the detected pair rate.

The presented quantum network experiments with the $^{40}Ca^{+}$ ion all show high fidelities and relatively low success probabilities. This setup leaves the highest potential for improvements. The observed success probability of the protocols are about $\sim 1 \times 10^{-5} - 1 \times 10^{-6}$, which is the efficiency from a photon sent to the setup, its absorption and the detection of the emitted Raman photon. Improvement of this efficiency is possible up to the percentage range by a new ion-trap setup with the use of a cavity for efficient absorption, emission, or both. The fidelities are mostly limited by the magnetic field fluctuations in the laboratory, which cause a degradation of the

coherence of Zeeman-sublevel superpositions. A large improvement would be possible, for example by an adequate magnetic shielding.

With these improvements the communication between two nodes becomes possible and opens the way to experiments with complex higher-level protocols, such as entanglement purification or the implementation of a quantum repeater.

Bibliography

[1] V. Giovannetti, S. Lloyd, L. Maccone: Quantum-Enhanced Measurements: Beating the Standard Quantum Limit. *Science* **306**, 1330–1336 (2004)

[2] R. P. Feynman: Simulating Physics with Computers. *International Journal of Theoretical Physics* **21**, 467–488 (1982)

[3] I. M. Georgescu, S. Ashhab, F. Nori: Quantum simulation. *Rev. Mod. Phys.* **86**, 153–185 (2014)

[4] R. P. Feynman: Quantum Mechanical Computers. *Optics News* **11**, 11–20 (1985)

[5] T. D. Ladd, F. Jelezko, R. Laflamme, Y. Nakamura, C. Monroe, J. L. O/'Brien: Quantum computers. *Nature* **464**, 45–53 (2010)

[6] C. Monroe, R. Raussendorf, A. Ruthven, K. R. Brown, P. Maunz, L.-M. Duan, J. Kim: Large-scale modular quantum-computer architecture with atomic memory and photonic interconnects. *Phys. Rev. A* **89**, 022317 (2014)

[7] K. R. Brown, J. Kim, C. Monroe: Co-designing a scalable quantum computer with trapped atomic ions. *npj Quantum Information* **2**, 16034 (2016)

[8] L. K. Grover: ANNUAL ACM SYMPOSIUM ON THEORY OF COMPUTING: A Fast Quantum Mechanical Algorithm for Database Search. ACM, 1996 212–219

[9] P. W. Shor: Polynomial-Time Algorithms for Prime Factorization and Discrete Logarithms on a Quantum Computer. *SIAM Journal on Computing* **26**, 1484–1509 (1997)

[10] J. M. Gambetta, J. M. Chow, M. Steffen: Building logical qubits in a superconducting quantum computing system. *npj Quantum Information* **3**, 2 (2017)

[11] M. H. Devoret, R. J. Schoelkopf: Superconducting Circuits for Quantum Information: An Outlook. *Science* **339**, 1169–1174 (2013)

[12] A. Córcoles, E. Magesan, S. J. Srinivasan, A. W. Cross, M. Steffen, J. M. Gambetta, J. M. Chow: Demonstration of a quantum error detection code using a square lattice of four superconducting qubits. *Nat. Commun.* **6**, 6979 (2015)

[13] D. Ristè, S. Poletto, M.-Z. Huang, A. Bruno, V. Vesterinen, O.-P. Saira, L. DiCarlo: Detecting bit-flip errors in a logical qubit using stabilizer measurements. *Nat. Commun.* **6**, 6983 (2015)

[14] J. Kelly, R. Barends, A. G. Fowler, A. Megrant, E. Jeffrey, T. C. White, D. Sank, J. Y. Mutus, B. Campbell, Y. Chen, Z. Chen, B. Chiaro, A. Dunsworth, I.-C. Hoi, C. Neill, P. J. J. O'Malley, C. Quintana, P. Roushan, A. Vainsencher, J. Wenner, A. N. Cleland, J. M. Martinis: State preservation by repetitive error detection in a superconducting quantum circuit. *Nature* **519**, 66 (2015)

[15] P. Schindler, J. T. Barreiro, T. Monz, V. Nebendahl, D. Nigg, M. Chwalla, M. Hennrich, R. Blatt: Experimental Repetitive Quantum Error Correction. *Science* **332**, 1059–1061 (2011)

[16] N. M. Linke, M. Gutierrez, K. A. Landsman, C. Figgatt, S. Debnath, K. R. Brown, C. Monroe: Fault-tolerant quantum error detection. *Science Advances* **3** (2017)

[17] T. Monz, P. Schindler, J. T. Barreiro, M. Chwalla, D. Nigg, W. A. Coish, M. Harlander, W. Hänsel, M. Hennrich, R. Blatt: 14-Qubit Entanglement: Creation and Coherence. *Phys. Rev. Lett.* **106**, 130506 (2011)

[18] N. Friis, O. Marty, C. Maier, C. Hempel, M. Holzäpfel, P. Jurcevic, M. B. Plenio, M. Huber, C. Roos, R. Blatt, B. Lanyon: Observation of Entangled States of a Fully Controlled 20-Qubit System. *Phys. Rev. X* **8**, 021012 (2018)

[19] E. Pednault, J. A. Gunnels, G. Nannicini, L. Horesh, T. Magerlein, E. Solomonik, R. Wisnieff: Breaking the 49-Qubit Barrier in the Simulation of Quantum Circuits. *arXiv* **1710.05867** (2017)

[20] A. K. Ekert: Quantum cryptography based on Bell's theorem. *Phys. Rev. Lett.* **67**, 661–663 (1991)

[21] F. Xu, B. Qi, H.-K. Lo: Experimental demonstration of phase-remapping attack in a practical quantum key distribution system. *New Journal of Physics* **12**, 113026 (2010)

[22] N. Jain, C. Wittmann, L. Lydersen, C. Wiechers, D. Elser, C. Marquardt, V. Makarov, G. Leuchs: Device Calibration Impacts Security of Quantum Key Distribution. *Phys. Rev. Lett.* **107**, 110501 (2011)

[23] H. J. Kimble: The quantum internet. *Nature* **453**, 1023 (2008)

[24] S. Wehner, D. Elkouss, R. Hanson: Quantum internet: A vision for the road ahead. *Science* **362** (2018)

[25] A. Stute, B. Casabone, B. Brandstätter, K. Friebe, T. E. Northup, R. Blatt: Quantum-state transfer from an ion to a photon. *Nature Photonics* **7**, 219 (2013)

[26] C. Kurz, M. Schug, P. Eich, J. Huwer, P. Müller, J. Eschner: Experimental protocol for high-fidelity heralded photon-to-atom quantum state transfer. *Nat. Commun.* **5**, 5527 (2014)

[27] C. Kurz, P. Eich, M. Schug, P. Müller, J. Eschner: Programmable atom-photon quantum interface. *Phys. Rev. A* **93**, 062348 (2016)

[28] N. Kalb, A. Reiserer, S. Ritter, G. Rempe: Heralded Storage of a Photonic Quantum Bit in a Single Atom. *Phys. Rev. Lett.* **114**, 220501 (2015)

[29] T. Ruster, C. T. Schmiegelow, H. Kaufmann, C. Warschburger, F. Schmidt-Kaler, U. G. Poschinger: A long-lived Zeeman trapped-ion qubit. *Appl. Phys. B* **122**, 254 (2016)

[30] Y. Wang, M. Um, J. Zhang, S. An, M. Lyu, J.-N. Zhang, L.-M. Duan, D. Yum, K. Kim: Single-qubit quantum memory exceeding ten-minute coherence time. *Nature Photonics* **11**, 646–650 (2017)

[31] M. Körber, O. Morin, S. Langenfeld, A. Neuzner, S. Ritter, G. Rempe: Decoherence-protected memory for a single-photon qubit. *Nature Photonics* **12**, 18–21 (2018)

[32] J. P. Gaebler, T. R. Tan, Y. Lin, Y. Wan, R. Bowler, A. C. Keith, S. Glancy, K. Coakley, E. Knill, D. Leibfried, D. J. Wineland: High-Fidelity Universal Gate Set for $^{9}Be^{+}$ Ion Qubits. *Phys. Rev. Lett.* **117**, 060505 (2016)

[33] S. Yang, Y. Wang, D. D. B. Rao, T. Hien Tran, A. S. Momenzadeh, M. Markham, D. J. Twitchen, P. Wang, W. Yang, R. Stöhr, P. Neumann, H. Kosaka, J. Wrachtrup: High-fidelity transfer and storage of photon states in a single nuclear spin. *Nature Photonics* **10**, 507 (2016)

[34] M. Schug, J. Huwer, C. Kurz, P. Müller, J. Eschner: Heralded Photonic Interaction between Distant Single Ions. *Phys. Rev. Lett.* **110**, 213603 (2013)

[35] H. M. Meyer, R. Stockill, M. Steiner, C. Le Gall, C. Matthiesen, E. Clarke, A. Ludwig, J. Reichel, M. Atatüre, M. Köhl: Direct Photonic Coupling of a Semiconductor Quantum Dot and a Trapped Ion. *Phys. Rev. Lett.* **114**, 123001 (2015)

[36] S. Ritter, C. Nölleke, C. Hahn, A. Reiserer, A. Neuzner, M. Uphoff, M. Mücke, E. Figueroa, J. Bochmann, G. Rempe: An elementary quantum network of single atoms in optical cavities. *Nature* **484**, 195 (2012)

[37] M. Żukowski, A. Zeilinger, M. A. Horne, A. K. Ekert: "Event-ready-detectors" Bell experiment via entanglement swapping. *Phys. Rev. Lett.* **71**, 4287–4290 (1993)

[38] L.-M. Duan, M. D. Lukin, J. I. Cirac, P. Zoller: Long-distance quantum communication with atomic ensembles and linear optics. *Nature* **414**, 413–418 (2001)

[39] D. L. Moehring, P. Maunz, S. Olmschenk, K. C. Younge, D. N. Matsukevich, L.-M. Duan, C. Monroe: Entanglement of single-atom quantum bits at a distance. *Nature* **449**, 68 (2007)

[40] B. Hensen, H. Bernien, A. E. Dréau, A. Reiserer, N. Kalb, M. S. Blok, J. Ruitenberg, R. F. L. Vermeulen, R. N. Schouten, C. Abellán, W. Amaya, V. Pruneri, M. W. Mitchell, M. Markham, D. J. Twitchen, D. Elkouss, S. Wehner, T. H. Taminiau, R. Hanson: Loophole-free Bell inequality violation using electron spins separated by 1.3 kilometres. *Nature* **526**, 682 (2015)

[41] Y. Yu, F. Ma, X.-Y. Luo, B. Jing, P.-F. Sun, R.-Z. Fang, C.-W. Yang, H. Liu, M.-Y. Zheng, X.-P. Xie, W.-J. Zhang, L.-X. You, Z. Wang, T.-Y. Chen, Q. Zhang, X.-H. Bao, J.-W. Pan: Entanglement of two quantum memories via metropolitan-scale fibers. *arXiv* **1903.11284v1** (2019)

[42] S. Lloyd, M. S. Shahriar, J. H. Shapiro, P. R. Hemmer: Long Distance, Unconditional Teleportation of Atomic States via Complete Bell State Measurements. *Phys. Rev. Lett.* **87**, 167903 (2001)

[43] Z. Y. Ou: Efficient conversion between photons and between photon and atom by stimulated emission. *Phys. Rev. A* **78**, 023819 (2008)

[44] M. Bock, P. Eich, S. Kucera, M. Kreis, A. Lenhard, C. Becher, J. Eschner: High-fidelity entanglement between a trapped ion and a telecom photon via quantum frequency conversion. *Nat. Commun.* **9**, 1998 (2018)

[45] H.-J. Briegel, W. Dür, J. I. Cirac, P. Zoller: Quantum Repeaters: The Role of Imperfect Local Operations in Quantum Communication. *Phys. Rev. Lett.* **81**, 5932 (1998)

[46] C. H. Bennett, G. Brassard, S. Popescu, B. Schumacher, J. A. Smolin, W. K. Wootters: Purification of Noisy Entanglement and Faithful Teleportation via Noisy Channels. *Phys. Rev. Lett.* **76**, 722–725 (1996)

[47] C. H. Bennett, G. Brassard, C. Crépeau, R. Jozsa, A. Peres, W. K. Wootters: Teleporting an unknown quantum state via dual classical and Einstein-Podolsky-Rosen channels. *Phys. Rev. Lett.* **70**, 1895–1899 (1993)

[48] D. Bouwmeester, J.-W. Pan, K. Mattle, M. Eibl, H. Weinfurter, A. Zeilinger: Experimental quantum teleportation. *Nature* **390**, 575–579 (1997)

[49] I. Marcikic, H.de Riedmatten, W. Tittel, H. Zbinden, N. Gisin: Long-distance teleportation of qubits at telecommunication wavelengths. *Nature* **421**, 509–513 (2003)

[50] O. Landry, J. A. W. Houwelingen, A. Beveratos, H. Zbinden, N. Gisin: Quantum teleportation over the Swisscom telecommunication network. *J. Opt. Soc. Am. B* **24**, 398–403 (2007)

[51] J. Yin, J.-G. Ren, H. Lu, Y. Cao, H.-L. Yong, Y.-P. Wu, C. Liu, S.-K. Liao, F. Zhou, Y. Jiang, X.-D. Cai, P. Xu, G.-S. Pan, J.-J. Jia, Y.-M. Huang, H. Yin, J.-Y. Wang, Y.-A. Chen, C.-Z. Peng, J.-W. Pan: Quantum teleportation and entanglement distribution over 100-kilometre free-space channels. *Nature* **488**, 185–188 (2012)

[52] X.-S. Ma, S. Kropatschek, W. Naylor, T. Scheidl, J. Kofler, T. Herbst, A. Zeilinger, R. Ursin: Experimental quantum teleportation over a high-loss free-space channel. *Opt. Express* **20**, 23126–23137 (2012)

[53] X.-S. Ma, T. Herbst, T. Scheidl, D. Wang, S. Kropatschek, W. Naylor, B. Wittmann, A. Mech, J. Kofler, E. Anisimova, V. Makarov, T. Jennewein, R. Ursin, A. Zeilinger: Quantum teleportation over 143 kilometres using active feed-forward. *Nature* **489**, 269–273 (2012)

[54] J.-G. Ren, P. Xu, H.-L. Yong, L. Zhang, S.-K. Liao, J. Yin, W.-Y. Liu, W.-Q. Cai, M. Yang, L. Li, K.-X. Yang, X. Han, Y.-Q. Yao, J. Li, H.-Y. Wu, S. Wan, L. Liu, D.-Q. Liu, Y.-W. Kuang, Z.-P. He, P. Shang, C. Guo, R.-H. Zheng, K. Tian, Z.-C. Zhu, N.-L. Liu, C.-Y. Lu, R. Shu, Y.-A. Chen, C.-Z. Peng, J.-Y. Wang, J.-W. Pan: Ground-to-satellite quantum teleportation. *Nature* **549**, 70–73 (2017)

[55] J. F. Sherson, H. Krauter, R. K. Olsson, B. Julsgaard, K. Hammerer, I. Cirac, E. S. Polzik: Quantum teleportation between light and matter. *Nature* **443**, 557–560 (2006)

[56] Y.-A. Chen, S. Chen, Z.-S. Yuan, B. Zhao, C.-S. Chuu, J. Schmiedmayer, J.-W. Pan: Memory-built-in quantum teleportation with photonic and atomic qubits. *Nature Physics* **4**, 103–107 (2008)

[57] F. Bussières, C. Clausen, A. Tiranov, B. Korzh, V. B. Verma, S. W. Nam, F. Marsili, A. Ferrier, P. Goldner, H. Herrmann, C. Silberhorn, W. Sohler, A. Mikael, N. Gisin: Quantum teleportation from a telecom-wavelength photon to a solid-state quantum memory. *Nature Photonics* **8**, 775–778 (2014)

[58] C. Nölleke, A. Neuzner, A. Reiserer, C. Hahn, G. Rempe, S. Ritter: Efficient Teleportation Between Remote Single-Atom Quantum Memories. *Phys. Rev. Lett.* **110**, 140403 (2013)

[59] X.-H. Bao, X.-F. Xu, C.-M. Li, Z.-S. Yuan, C.-Y. Lu, J.-W. Pan: Quantum teleportation between remote atomic-ensemble quantum memories. *Proceedings of the National Academy of Sciences* **109**, 20347–20351 (2012)

[60] W. Pfaff, B. J. Hensen, H. Bernien, S. B. Dam, M. S. Blok, T. H. Taminiau, M. J. Tiggelman, R. N. Schouten, M. Markham, D. J. Twitchen, R. Hanson: Unconditional quantum teleportation between distant solid-state quantum bits. *Science* **345**, 532–535 (2014)

[61] C. Schuck: Interfacing single ions and single photons for quantum networks, ICFO - The Institute of Photonic Sciences / Universitat Politècnica de Catalunya, Dissertation, 2009

[62] F. Rohde: Remote ion traps for quantum networking: Two-photon interference and correlations, ICFO - The Institute of Photonic Sciences / Universitat Politècnica de Catalunya, Dissertation, 2009

[63] M. Almendros: Towards Long-Distance Quantum Communication, ICFO - The Institute of Photonic Sciences / Universitat Politècnica de Catalunya, Dissertation, 2009

[64] N. Piro: Controlled absorption of heralded single photons by a single atom: Towards entanglement distribution in quantum networks, ICFO - The Institute of Photonic Sciences / Universitat Politècnica de Catalunya, Dissertation, 2010

[65] J. Huwer: Experimental tools for quantum networking operations with single photons and single ions, Universität des Saarlandes, ICFO - The Institute of Photonic Sciences / Universitat Politècnica de Catalunya, Dissertation, 2013

[66] C. Kurz: Quantum networking with single ions and single photons interfaced in free space, Universität des Saarlandes, Dissertation, 2015

[67] M. Schug: Single photons from single ions: quantum interference and distant ion interaction, Universität des Saarlandes, Dissertation, 2015

[68] A. Haase, N. Piro, J. Eschner, M. W. Mitchell: Tunable narrowband entangled photon pair source for resonant single-photon single-atom interaction. *Opt. Lett.* **34**, 55 (2009)

[69] A. Lenhard: Quantum Photonic Interfaces between Atomic and Telecommunication Wavelengths, Universität des Saarlandes, Dissertation, 2015

[70] J. M. Brito Rozas: Quantum interfaces based on single photons from parametric down-conversion, Universität des Saarlandes, Dissertation, 2016

[71] P. Müller, J. Eschner: Single calcium-40 ion as quantum memory for photon polarization: a case study. *Appl. Phys. B* **114**, 303 (2014)

[72] M. Bock: in preparation, Universität des Saarlandes, Dissertation

[73] P. Eich: Submitted: Single-ion based quantum interfaces for quantum-network applications, Universität des Saarlandes, Dissertation, 2019

[74] P. Müller, et al.: Measurement of the scattering phase of a single spontaneous Raman photon. *In preparation* (2019)

[75] P. Müller: in preparation, Universität des Saarlandes, Dissertation

[76] P. K. Ghosh: Ion traps. Oxford University Press, 1995

[77] W. Paul: Electromagnetic traps for charged and neutral particles. *Rev. Mod. Phys.* **62**, 531–540 (1990)

[78] C. Schuck, M. Almendros, F. Rohde, M. Hennrich, J. Eschner: Two-color photoionization of calcium using SHG and LED light. *Applied Physics B* **100**, 765–771 (2010)

[79] R. W. P. Drever, J. L. Hall, F. V. Kowalski, J. Hough, G. M. Ford, A. J. Munley, H. Ward: Laser phase and frequency stabilization using an optical resonator. *Appl. Phys. B* **31**, 97–105 (1983)

[80] F. Rohde, M. Almendros, C. Schuck, J. Huwer, M. Hennrich, J. Eschner: A diode laser stabilization scheme for $^{40}Ca^{+}$ single-ion spectroscopy. *Journal of Physics B: Atomic, Molecular and Optical Physics* **43**, 115401 (2010)

[81] M. Kreis: Magnetfeldstabilisierung für Hochpräzise Einzelatom Spektroskopie, Universität des Saarlandes, Master thesis, 2014

[82] S. Kucera: Digitale LASER Leistungsstabilisierung für Einzelatomspektroskopie, Universität des Saarlandes, Diploma thesis, 2013

[83] S. Gerber, D. Rotter, M. Hennrich, R. Blatt, F. Rohde, C. Schuck, M. Almendros, R. Gehr, F. Dubin, J. Eschner: Quantum interference from remotely trapped ions. *New Journal of Physics* **11**, 13032 (2009)

[84] M. Almendros, J. Huwer, N. Piro, F. Rohde, C. Schuck, M. Hennrich, F. Dubin, J. Eschner: Bandwidth-Tunable Single-Photon Source in an Ion-Trap Quantum Network. *Phys. Rev. Lett.* **103**, 213601 (2009)

[85] C. Kurz, J. Huwer, M. Schug, P. Müller, J. Eschner: A high-rate source for single photons in a pure quantum state. *New Journal of Physics* **15**, 055005 (2013)

[86] F. Rohde, J. Huwer, N. Piro, M. Almendros, C. Schuck, F. Dubin, J. Eschner: Polarization-correlated photon pairs from a single ion. *J. Opt. Soc. Am. B* **27**, A 81 (2010)

[87] M. Schug, C. Kurz, P. Eich, J. Huwer, P. Müller, J. Eschner: Quantum interference in the absorption and emission of single photons by a single ion. *Phys. Rev. A* **90**, 023829 (2014)

[88] N. Piro, A. Haase, M. W. Mitchell, J. Eschner: An entangled photon source for resonant single-photon–single-atom interaction. *J. Phys. B: At. Mol. Opt. Phys.* **42**, 114002 (2009)

[89] C. Schuck, F. Rohde, N. Piro, M. Almendros, J. Huwer, M. W. Mitchell, M. Hennrich, A. Haase, F. Dubin, J. Eschner: Resonant interaction of a single atom with single photons from a down-conversion source. *Phys. Rev. A* **81**, 011802 (2010)

[90] N. Piro, F. Rohde, C. Schuck, M. Almendros, J. Huwer, J. Ghosh, A. Haase, M. Hennrich, F. Dubin, J. Eschner: Heralded single-photon absorption by a single atom. *Nature Physics* **7**, 17 (2011)

[91] J. Huwer, J. Ghosh, N. Piro, M. Schug, F. Dubin, J. Eschner: Photon entanglement detection by a single atom. *New Journal of Physics* **15**, 025033 (2013)

[92] J. Brito, S. Kucera, P. Eich, P. Müller, J. Eschner: Doubly heralded single-photon absorption by a single atom. *Appl. Phys. B* **122**, 36 (2016)

[93] F. Wolfgramm, X. Xing, A. Cerè, A. Predojević, A. M. Steinberg, M. W. Mitchell: Bright filter-free source of indistinguishable photon pairs. *Opt. Express* **16**, 18145–18151 (2008)

[94] J. Fekete, D. Rieländer, M. Cristiani, H.de Riedmatten: Ultranarrow-Band Photon-Pair Source Compatible with Solid State Quantum Memories and Telecommunication Networks. *Phys. Rev. Lett.* **110**, 220502 (2013)

[95] M. Scholz, L. Koch, R. Ullmann, O. Benson: Single-mode operation of a high-brightness narrow-band single-photon source. *Appl. Phys. Lett.* **94**, 201105 (2009)

[96] A. Lenhard, M. Bock, C. Becher, S. Kucera, J. Brito, P. Eich, P. Müller, J. Eschner: Telecom-heralded single-photon absorption by a single atom. *Phys. Rev. A* **92**, 063827 (2015)

[97] A. Ahlrichs, O. Benson: Bright source of indistinguishable photons based on cavity-enhanced parametric down-conversion utilizing the cluster effect. *Applied Physics Letters* **108**, 021111 (2016)

[98] M. Förtsch, J. U. Fürst, C. Wittmann, D. Strekalov, A. Aiello, M. V. Chekhova, C. Silberhorn, G. Leuchs, C. Marquardt: A versatile source of single photons for quantum information processing. *Nat. Commun.* **4**, 1818 (2013)

[99] K. H. Luo, H. Herrmann, S. Krapick, B. Brecht, R. Ricken, V. Quiring, H. Suche, W. Sohler, C. Silberhorn: Direct generation of genuine single-longitudinal-mode narrowband photon pairs. *New Journal of Physics* **17**, 073039 (2015)

[100] P. G. Kwiat, P. H. Eberhard, A. M. Steinberg, R. Y. Chiao: Proposal for a loophole-free Bell inequality experiment. *Phys. Rev. A* **49**, 3209–3220 (1994)

[101] A. Fedrizzi, T. Herbst, A. Poppe, T. Jennewein, A. Zeilinger: A wavelength-tunable fiber-coupled source of narrowband entangled photons. *Opt. Express* **15**, 15377 (2007)

[102] M. Fiorentino, G. Messin, C. E. Kuklewicz, F. N. C. Wong, J. H. Shapiro: Generation of ultrabright tunable polarization entanglement without spatial, spectral, or temporal constraints. *Phys. Rev. A* **69**, 041801 (2004)

[103] C. Clausen, F. Bussières, A. Tiranov, H. Herrmann, C. Silberhorn, W. Sohler, M. Afzelius, N. Gisin: A source of polarization-entangled photon pairs interfacing quantum memories with telecom photons. *New Journal of Physics* **16**, 093058 (2014)

[104] B.-S. Shi, A. Tomita: Generation of a pulsed polarization entangled photon pair using a Sagnac interferometer. *Phys. Rev. A* **69**, 013803 (2004)

[105] R. W. Boyd: Nonlinear Optics. Academic Press, 2003

[106] Z.-Y. J. Ou: Multi-Photon Quantum Interference. Springer US, 2007

[107] B. Boulanger, J. P. Fève, G. Marnier, B. Ménaert, X. Cabirol, P. Villeval, C. Bonnin: Relative sign and absolute magnitude of d(2) nonlinear coefficients of KTP from second-harmonic-generation measurements. *J. Opt. Soc. Am. B* **11**, 750–757 (1994)

[108] B. E. A. Saleh, M. C. Teich: Fundamentals Of Photonics. Wiley, 2007

[109] K. Kato, E. Takaoka: Sellmeier and thermo-optic dispersion formulas for KTP. *Appl. Opt.* **41**, 5040–5044 (2002)

[110] G. D. Boyd, D. A. Kleinman: Parametric Interaction of Focused Gaussian Light Beams. *J. of Appl. Phys.* **39**, 3597–3639 (1968)

[111] A. Predojević: Rubidium resonant squeezed light from a diode-pumped optical-parametric oscillator, ICFO - The Institute of Photonic Sciences / Universitat Politècnica de Catalunya, Dissertation, 2009

[112] F. Wolfgramm: Atomic Quantum Metrology with Narrowband Entangled and Squeezed States of Light, ICFO - The Institute of Photonic Sciences / Universitat Politècnica de Catalunya, Dissertation, 2011

[113] A. E. Siegman: Nonlinear Optics. University Science Books, 1986

[114] P. Palittapongarnpim, A. MacRae, A. I. Lvovsky: Note: A monolithic filter cavity for experiments in quantum optics. *Review of Scientific Instruments* **83**, 066101 (2012)

[115] A. Ahlrichs, C. Berkemeier, B. Sprenger, O. Benson: A monolithic polarization-independent frequency-filter system for filtering of photon pairs. *Appl. Phys. Lett.* **103**, 241110 (2013)

[116] K. J. McNeil, C. W. Gardiner: Quantum statistics of parametric oscillation. *Phys. Rev. A* **28**, 1560–1566 (1983)

[117] I. L. Chuang, M. A. Nielsen: Quantum Computation and Quantum Information. Cambridge University Press, 2010

[118] D. F. V. James, P. G. Kwiat, W. J. Munro, A. G. White: Measurement of qubits. *Phys. Rev. A* **64**, 052312 (2001)

[119] W. K. Wootters: Entanglement of Formation of an Arbitrary State of Two Qubits. *Phys. Rev. Lett.* **80**, 2245–2248 (1998)

[120] A. Predojević, S. Grabher, G. Weihs: Pulsed Sagnac source of polarization entangled photon pairs. *Opt. Express* **20**, 25022–25029 (2012)

[121] F. N. C. Wong, J. H. Shapiro, T. Kim: Efficient generation of polarization-entangled photons in a nonlinear crystal. *Laser Physics* **16**, 1517–1524 (2006)

[122] T. Kim, M. Fiorentino, F. N. C. Wong: Phase-stable source of polarization-entangled photons using a polarization Sagnac interferometer. *Phys. Rev. A* **73**, 012316 (2006)

[123] L. Sansoni, K. H. Luo, C. Eigner, R. Ricken, V. Quiring, H. Herrmann, C. Silberhorn: A two-channel, spectrally degenerate polarization entangled source on chip. *npj Quantum Information* **3** (2017)

[124] J. Arensk̈otter: Photonenpaarquelle für Einzelatom-Einzelphoton Wechselwirkung, Universität des Saarlandes, Master thesis, 2016

[125] P. Müller, T. Tentrup, M. Bienert, G. Morigi, J. Eschner: Spectral properties of single photons from quantum emitters. *Phys. Rev. A* **96**, 023861 (2017)

[126] I. L. Chuang, M. A. Nielsen: Prescription for experimental determination of the dynamics of a quantum black box. *Journal of Modern Optics* **44**, 2455–2467 (1997)

[127] C. Howson, P. Urbach: Scientific Reasoning: The Bayesian Approach. *Open Court Publishing Company* (2005)

A. Appendix

A.1. Probability estimation and background correction

The quantum-state reconstruction of a qubit is based on projective measurements onto defined states $|\varphi\rangle$. For each projection setting we estimate the probability to detect the state $|\varphi\rangle$ and not its orthogonal counterpart $|\varphi_\perp\rangle$. These probabilities are the accessible quantities of the qubit quantum state that is in general represented by a density matrix. This section describes the procedure how the probabilities are estimated. We therefore use a finite number of measurements for a fixed projection setting to update the *prior* distribution of p with Bayesian inference [66, 75, 127]. The result is the *posterior* distribution of p. We now use the expectation value $\langle p \rangle$ as estimator and the standard deviation Δp as a measure of its uncertainty. In the following this procedure is explained, first under ideal conditions, and then under the more realistic conditions considering losses and background.

Case I: Ideal experiment

An idealized picture of a lossless projective measurement is given in figure A.1. By repeating the measurement N times for a fixed projection setting we detect k_1 events in one arm and $k_2 = N - k_1$ events in the other output. We estimate the underlying probability p with the Bayesian inference method, and update the *prior* probability distribution $\mathrm{P}(p)$ by the measurement result. We use the expectation value $\langle p \rangle$ and the standard deviation Δp of the updated *posterior* distribution $\mathrm{P}(p \,|\, N, k_1)$ as estimators for the underlying probability p and its uncertainty. The posterior is then calculated with Bayes theorem

$$\mathrm{P}(p \,|\, N, k_1) = \frac{\mathrm{P}(k_1 \,|\, N, p)\ \mathrm{P}(p)}{\mathrm{P}(k_1 \,|\, N)} \tag{A.1}$$

whereby $\mathrm{P}(k_1 \,|\, N, p)$ denotes k_1 events in N independent projections with the underlying probability p, which is the binomial distribution. We use the uniform prior $\mathrm{P}(p) = 1$, which corresponds to complete ignorance about the qubit that is projected

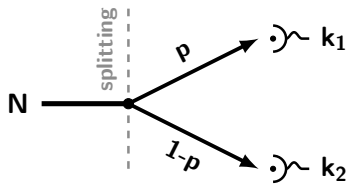

Figure A.1.: Ideal projection measurement: Each try results in a click of one detector with the underlying probability p.

in the measurement[1]. The denominator is given by[2]

$$\mathrm{P}(k_1 \,|\, N) = \int_0^1 \mathrm{P}(k_1 \,|\, N, p) \cdot \mathrm{P}(p)\ dp = \frac{1}{N+1} \tag{A.2}$$

as a result we obtain the updated distribution

$$\mathrm{P}(p \,|\, N, k_1) = (N+1) \binom{N}{k_1}\ p^{k_1}\ (1-p)^{N-k_1} \tag{A.3}$$

With the distribution we calculate the expectation value as the estimator

$$\langle p \rangle = \int_0^1 p \cdot \mathrm{P}(p \,|\, N, k_1)\ dp = \frac{k_1+1}{N+2} \tag{A.4}$$

and with the second moment

$$\langle p^2 \rangle = \int_0^1 p^2 \cdot \mathrm{P}(p \,|\, N, k_1)\ dp = \frac{(k_1+1)(k_1+2)}{(N+2)(N+3)} \tag{A.5}$$

we get the uncertainty

$$\Delta p = \sqrt{\langle p^2 \rangle - \langle p \rangle^2} \tag{A.6}$$

The estimator $\langle p \rangle$ in equation A.4 becomes never zero or one ($0 < \langle p \rangle < 1$), and the uncertainty is also larger than zero ($\Delta p > 0$) for a finite number of measurements. This is also the case when $k_1 = 0$, which is in contrast to the reconstructed values with frequentist inference.

[1] One might think about the simple projection measurement of a photonic polarization qubit consisting of a half-wave plate, a polarizing beam splitter and two detectors at its output. In this case it is more convenient to treat the angle φ of the half-wave plate as equally distributed. As a result the probability in dependence of this angle is no longer equally distributed. The situation becomes different when a quarter-wave is included to cover all possible projection polarizations and not only the linear ones and the probability distribution of p becomes uniform $\mathrm{P}(p) = 1$.

[2] Integration: $\int_0^1 \binom{N}{k}\ p^k\ (1-p)^{N-k}\ dp = \frac{1}{N+1}$

Case II: Detection efficiencies

For experiments with single photons we need to include detection efficiencies of the two channels. The situation is depicted in figure A.2, the projection with probability p splits the N trials into k_1', and k_2' in the two arms. We treat the detection as

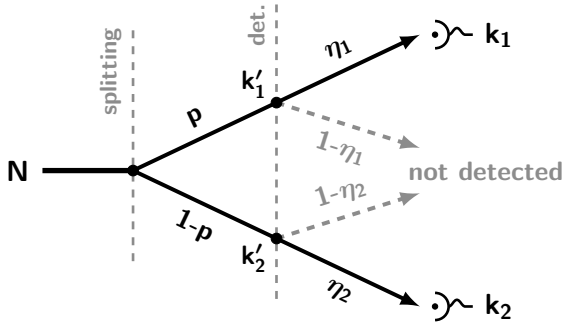

Figure A.2.: Projection measurement with losses in the detection.

subsequent Bernoulli process with probabilities η_1, η_2. The appropriate probability distributions are binomial distributions of the form

$$\begin{aligned} \mathrm{P}(k_1 \,|\, k_1', \eta_1) &= \binom{k_1'}{k_1} \, \eta_1^{k_1} \, (1-\eta_1)^{k_1'-k_1} \\ \mathrm{P}(k_2 \,|\, k_2', \eta_2) &= \binom{k_2'}{k_2} \, \eta_2^{k_2} \, (1-\eta_2)^{k_2'-k_2} \end{aligned} \tag{A.7}$$

These are stochastically independent, and the probability to detect k_1 events in one arm and k_2 events in the other can therefore be expressed as the product

$$\mathrm{P}(k_1 \wedge k_2 \,|\, k_1', k_2', \eta_1, \eta_2) = \mathrm{P}(k_1 \,|\, k_1', \eta_1) \cdot \mathrm{P}(k_2 \,|\, k_2', \eta_2) \tag{A.8}$$

To combine the detection with the projection we need to sum over all possible combinations

$$\mathrm{P}(k_1 \wedge k_2 \,|\, N, p, \eta_1, \eta_2) = \sum_{k_1'} \mathrm{P}(k_1 \,|\, k_1', p) \cdot \mathrm{P}(k_1 \wedge k_2 \,|\, k_1', N-k_1', \eta_1, \eta_2) \tag{A.9}$$

$$= \frac{N!}{k_1!\, k_2!\, (N-k_1-k_2)!} (\eta_1\, p)^{k_1} (\eta_2\, (1-p))^{k_2} (1-\eta_2+p\,(\eta_2-\eta_1))^{N-k_1-k_2} \tag{A.10}$$

Two special cases can be pointed out. The first is the situation of equal detection probability $\eta = \eta_1 = \eta_2$. With this assumption the distribution simplifies to

$$\mathrm{P}(k_1 \wedge k_2 \,|\, N, p, \eta) = \binom{N}{k_1+k_2} \left(\frac{\eta}{1-\eta}\right)^{k_1+k_2} (1-\eta)^N \binom{k_1+k_2}{k_1} p^{k_1} (1-p)^{k_2} \tag{A.11}$$

With Bayes Theorem we calculate the probability distribution of p

$$\mathrm{P}(p \,|\, N, \eta, k_1 \wedge k_2) = (k_1 + k_2 + 1) \binom{k_1 + k_2}{k_1} p^{k_1} (1-p)^{k_2} \tag{A.12}$$

and we get

$$\langle p \rangle = \frac{k_1 + 1}{k_1 + k_2 + 2} \qquad \langle p^2 \rangle = \frac{(k_1 + 1)(k_1 + 2)}{(k_1 + k_2 + 2)(k_1 + k_2 + 3)} \tag{A.13}$$

as estimator. We see that for equal detection efficiency the estimator is independent of the true number of trials N.

In the second special case one has maximal detection efficiency in one arm, $\eta_2 = 1$, then the probability distribution to detect k_1 and k_2 simplifies to a product of two binomial probability distributions

$$\mathrm{P}(k_1 \wedge k_2 \,|\, N, p, \eta_1) = \mathrm{P}(N - k_2 \,|\, N, p) \cdot \mathrm{P}(k_1 \,|\, N - k_2, \eta_1) \tag{A.14}$$

And we obtain

$$\langle p \rangle = \frac{(N - k_2) + 1}{N + 2} \qquad \langle p^2 \rangle = \frac{((N - k_2) + 1)((N - k_2) + 2)}{(N + 2)(N + 3)} \tag{A.15}$$

as estimators. It is important that the number of trials $N \geq k_1 + k_2$ can not be substituted from the estimators.

Case III: Background

Background correction has to be handled carefully, in particular when the signal that we want to correct is low compared to the Background. Consider a time-correlation measurement, for example the tomography of an entangled two-photon state. Each of the two photons is guided to a projection setup. With ideal detectors we observe no coincidences in certain projection state combinations in the two arms. When changing one arm to its orthogonal projection state, we see coincidences. The underlying probability for the splitting in this arm would be zero for the first case, and one for the second. When detector dark counts and stray light enter the coincidence measurements, then the correlation histograms get raised by a noisy background. This is the case for all uncorrelated background events. We typically divide the correlation measurements in two parts. In a time window with fixed width around zero time delay we expect the coincidences of true two-photon events; in the following these events

are called signal. Outside this time window only background events contribute, from which we estimate the expectation value of background counts per bin, λ_B. We treat the background as Poisson-distributed

$$\mathrm{P}_B(B) = \frac{(\lambda_B)^B}{B!}\, e^{-\lambda_B} \tag{A.16}$$

with the variance λ_B. At first it seems obvious to treat the two outputs of one projection stage independently and simply subtract the mean background λ_B from the detected signal S for each of the two correlation functions, to get the corrected signal coincidences C. For an ideal entangled state, however, we face a problem: when the signal is close to zero, the fluctuations of the background B can cause negative corrected values which are for sure not physical.

In the following two approaches are discussed to correct for the background. The first corrects the number detected coincidences of each of the two projection arms independently which are then fed into equations A.4 and A.6 to get the estimators. The second uses Bayesian inference to reconstruct the estimators directly with the knowledge of the Background distribution of each arm.

In the first approach we handle the problem by taking the distributions into account. Coincidences, and background are independent processes, the probability of C coincidences, and B background is then the product

$$\mathrm{P}(C \wedge B) = \mathrm{P}_C(C) \cdot \mathrm{P}_B(B) \tag{A.17}$$

of the Poissonian distributions for background $\mathrm{P}_B(B)$, and the coincidences $\mathrm{P}_C(C)$. The probability to detect S signal counts is then the sum over all possible combinations

$$\begin{aligned} \mathrm{P}(S) &= \sum_{B+C=S} \mathrm{P}_C(C) \cdot \mathrm{P}_B(B) \\ &= \sum_{C=0}^{S} \mathrm{P}_C(C) \cdot \mathrm{P}_B(S-C) \end{aligned} \tag{A.18}$$

and the expectation value of coincidences $\langle C \rangle$ is given by

$$\langle C \rangle = \frac{\sum_{C=0}^{N} C \cdot \mathrm{P}_C(C) \cdot \mathrm{P}_B(S-C)}{\sum_{C=0}^{N} \mathrm{P}_C(C) \cdot \mathrm{P}_B(S-C)} \tag{A.19}$$

We approximate that all possible numbers of coincidences have the same probability $\mathrm{P}_C(C) = const$ for all $C < S$. This simplifies the expectation value

$$\langle C \rangle = \frac{\sum_{C=0}^{N} C \cdot \mathrm{P}_B(S-C)}{\sum_{C=0}^{N} \mathrm{P}_B(S-C)} \tag{A.20}$$

which is numerically easy to solve. The background-corrected number of coincidences of two orthogonal projection settings are then used to calculate the estimator $\langle p \rangle$ and its uncertainty Δp according to equations A.4 and A.6. The advantages are that the number of coincidences is between zero and the detected value, and the background statistic is considered.

To avoid the assumption $\mathrm{P}_C(C) = const$, at the cost of higher numerical effort, we consider the situation of figure A.3. Each detector has a Poissonian background contribution with λ_{B1} and λ_{B2} as expectation values. The number of qubits sent onto the projection stage is also Poisson-distributed with expectation value λ_N. All three expectation values can either be extracted from the data itself, or from reference measurements. We now detect k_1 events in one arm, k_2 events in the other arm and

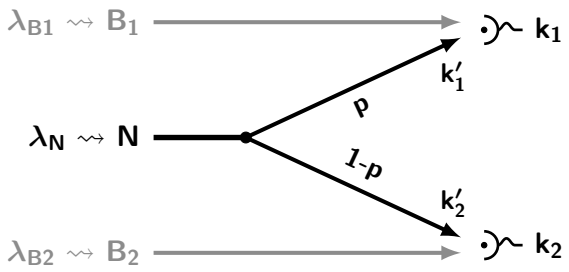

Figure A.3.: Projection measurement with background contribution, and poissonian signal statistics.

ask for the splitting probability p. We therefore divide the process into two parts, the splitting, and the subsequent detection. We imagine the situation where N qubits are split by the projection into k_1' events in the upper arm, and k_2' events in the lower arm. The probability to detect k_1 under the condition of having k_1' from the projection and the Poisson distributed background is then given by

$$\mathrm{P}_{det}(k_1 \,|\, k_1', \lambda_{B1}) = \begin{cases} \mathrm{P}_B(k_1 - k_1' \,|\, \lambda_{B1}) & 0 \le k_1' \le k_1 \\ 0 & \text{otherwise} \end{cases} \tag{A.21}$$

and analogously for the other arm

$$\mathrm{P}_{det}(k_2 \,|\, k_2', \lambda_{B2}) = \begin{cases} \mathrm{P}_B(k_2 - k_2' \,|\, \lambda_{B2}) & 0 \le k_2' \le k_2 \\ 0 & \text{otherwise} \end{cases} \tag{A.22}$$

The two detections are independent under the condition of the previously performed projection. We write the joint probability as the product

$$\mathrm{P}_{det}(k_1 \wedge k_2 \,|\, k_1' \wedge k_2', \lambda_{B1}, \lambda_{B2}) = \mathrm{P}_{det}(k_1 \,|\, k_1', \lambda_{B1}) \cdot \mathrm{P}_{det}(k_2 \,|\, k_2', \lambda_{B2}) \tag{A.23}$$

The projection is described by the binomial distribution

$$\mathrm{P}_{proj.}(k_1' \wedge k_2' \,|\, N, p) = \mathrm{P}_{proj.}(k_1' \,|\, N, p) = \binom{N}{k_1'} \; p^{k_1'} \; (1-p)^{N-k_1'} \tag{A.24}$$

which is the probability of having k_1', and k_2' events from the projection under the condition of having N qubits and the projection probability p. The joint probability distribution of projection, and detection under the condition of having N qubits, the projection probability p , and the two background expectation values $\lambda_{B1,B2}$ is then the sum over all possible splitting combinations

$$\mathrm{P}(k_1 \wedge k_2 \,|\, \lambda_{B1}, \lambda_{B2}, N, p) = \sum_{k_1'=0}^{N} \mathrm{P}_{det}(k_1 \wedge k_2 \,|\, k_1' \wedge k_2', \lambda_{B1}, \lambda_{B2}) \cdot \mathrm{P}_{proj.}(k_1' \wedge k_2' \,|\, N, p) \tag{A.25}$$

The next step takes the Poissonian distribution $\mathrm{P}_N(N \,|\, \lambda_N)$ of the number of qubits into account. The joint probability distribution under the condition of the three expectation values, and the splitting probability p is then

$$\begin{aligned} \mathrm{P}(k_1 \wedge k_2 \,|\, \lambda_{B1}, \lambda_{B2}, \lambda_N, p) &= \sum_{N=0}^{k_1+k_2} \mathrm{P}(k_1 \wedge k_2 \,|\, \lambda_{B1}, \lambda_{B2}, N, p) \cdot \mathrm{P}_N(N \,|\, \lambda_N) \\ &= \sum_{N=0}^{k_1+k_2} \left(\sum_{k_1'=0}^{N} \mathrm{P}_B(k_1 - k_1' \,|\, \lambda_{B1}) \cdot \mathrm{P}_B(k_2 - (N - k_1') \,|\, \lambda_{B2}) \cdot \mathrm{P}_{proj.}(k_1' \,|\, N, p) \right) \cdot \mathrm{P}_N(N \,|\, \lambda_N) \end{aligned} \tag{A.26}$$

With Bayes theorem we get the posterior distribution of the probability p

$$\begin{aligned} \mathrm{P}(p \,|\, \lambda_{B1}, \lambda_{B2}, \lambda_N, k_1 \wedge k_2) &= \frac{\mathrm{P}(k_1 \wedge k_2 \,|\, \lambda_{B1}, \lambda_{B2}, \lambda_N, p) \; P(p)}{\mathrm{P}(k_1 \wedge k_2 \,|\, \lambda_{B1}, \lambda_{B2}, \lambda_N)} \\ &= \frac{\mathrm{P}(k_1 \wedge k_2 \,|\, \lambda_{B1}, \lambda_{B2}, \lambda_N, p) \; P(p)}{\int_0^1 \mathrm{P}(k_1 \wedge k_2 \,|\, \lambda_{B1}, \lambda_{B2}, \lambda_N, p) \; P(p) \; dp} \end{aligned} \tag{A.27}$$

With the prior distribution $\mathrm{P}(p) = 1$ of the underlying probability p. This allows to

calculate the estimators

$$\langle p\rangle = \frac{\int_0^1 p\ \mathrm{P}(k_1 \wedge k_2 \,|\, \lambda_{B1}, \lambda_{B2}, \lambda_N, p)\ P(p)\ dp}{\int_0^1 \mathrm{P}(k_1 \wedge k_2 \,|\, \lambda_{B1}, \lambda_{B2}, \lambda_N, p)\ P(p)\ dp}$$
$$= \frac{\sum_{N=0}^{k_1+k_2} \left(\sum_{k_1'=0}^{N} \mathrm{P}_B(k_1 - k_1' \,|\, \lambda_{B1}) \cdot \mathrm{P}_B(k_2 - (N - k_1') \,|\, \lambda_{B2}) \cdot \frac{k_1'+1}{(N+1)(N+2)} \right) \cdot \mathrm{P}_N(N \,|\, \lambda_N)}{\sum_{N=0}^{k_1+k_2} \left(\sum_{k_1'=0}^{N} \mathrm{P}_B(k_1 - k_1' \,|\, \lambda_{B1}) \cdot \mathrm{P}_B(k_2 - (N - k_1') \,|\, \lambda_{B2}) \cdot \frac{1}{(N+1)} \right) \cdot \mathrm{P}_N(N \,|\, \lambda_N)} \tag{A.28}$$

$$\langle p^2\rangle = \frac{\int_0^1 p^2\ \mathrm{P}(k_1 \wedge k_2 \,|\, \lambda_{B1}, \lambda_{B2}, \lambda_N, p)\ P(p)\ dp}{\int_0^1 \mathrm{P}(k_1 \wedge k_2 \,|\, \lambda_{B1}, \lambda_{B2}, \lambda_N, p)\ P(p)\ dp}$$
$$= \frac{\sum_{N=0}^{k_1+k_2} \left(\sum_{k_1'=0}^{N} \mathrm{P}_B(k_1 - k_1' \,|\, \lambda_{B1}) \cdot \mathrm{P}_B(k_2 - (N - k_1') \,|\, \lambda_{B2}) \cdot \frac{(k_1'+1)(k_1'+2)}{(N+1)(N+2)(N+3)} \right) \cdot \mathrm{P}_N(N \,|\, \lambda_N)}{\sum_{N=0}^{k_1+k_2} \left(\sum_{k_1'=0}^{N} \mathrm{P}_B(k_1 - k_1' \,|\, \lambda_{B1}) \cdot \mathrm{P}_B(k_2 - (N - k_1') \,|\, \lambda_{B2}) \cdot \frac{1}{(N+1)} \right) \cdot \mathrm{P}_N(N \,|\, \lambda_N)} \tag{A.29}$$

The numbers of terms in the nominator and denominator are of the order of $(k_1+k_2)^2$ which is the numerical cost of this method.

Case IV: Background and detection efficiencies

The next step is to include detection efficiencies. For different efficiencies we assume without loss of generality that $\eta_1 < \eta_2$. We further divide the detection of the arm with the lower efficiency η_1 into two parts one with η_2 and another with $\eta_{rel} = \frac{\eta_1}{\eta_2}$ so that we get $\eta_1 = \eta_2 \cdot \frac{\eta_1}{\eta_2} = \eta_2 \cdot \eta_{rel}$. As a result we have a part with equal detection efficiency η_2 and a second part where η_{rel} is depleting one arm. In case II we found the special situation of equal detection efficiency. The estimators (*c.f.* equation A.13) are independent of the true number of trials. This allows to factorize the equal part of the detection efficiency (η_1) by using the depleted expectation value $\lambda_N' = \eta_1 \cdot \lambda_N$. The remaining system is depicted in figure A.4. It is the direct extension of case III with efficiency η_{rel} in one arm. For simplicity we write in the following $\eta_{rel} = \eta$. The mathematical derivation is analogous to case III, the main difference is that we have to replace the distribution of the projection by the combined distribution of projection, and detection efficiency (*c.f.* equation A.14) described by

$$\mathrm{P}_{proj./eff}(k_1'' \wedge k_2' \,|\, N, \eta, p) = \mathrm{P}_{proj}(N - k_2' \,|\, N, p) \cdot \mathrm{P}_{eff}(k_1'' \,|\, N - k_2', \eta) \tag{A.30}$$

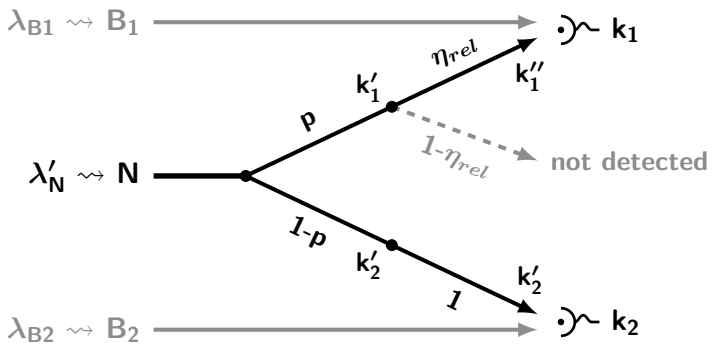

Figure A.4.: Projection measurement with included background contribution, detection efficiencies, and poissonian statistics of the signal.

The joint probability distribution under the condition of the three expectation values, the relative efficiency η, and the splitting probability p is then

$$\mathrm{P}(k_1 \wedge k_2 \,|\, \lambda_{B1}, \lambda_{B2}, \lambda'_N, \eta, p) = \sum_{N=0}^{\infty} \left(\sum_{k''_1, k'_2} \mathrm{P}_B(k_1 - k''_1 \,|\, \lambda_{B1}) \cdot \mathrm{P}_B(k_2 - k'_2 \,|\, \lambda_{B2}) \cdot \mathrm{P}_{proj./eff}(k''_1 \wedge k'_2 \,|\, N, \eta, p) \right) \cdot \mathrm{P}_N(N \,|\, \lambda'_N) \tag{A.31}$$

The exterior sum over N is now a infinite sum, and the interior sum is over all possible combinations that fulfill the condition $k''_1 + k'_2 \leq N$. With Bayes theorem, and the prior distribution $\mathrm{P}(p) = 1$ of the underlying probability p we get the estimators

$$\langle p \rangle = \frac{\sum_{N=0}^{\infty} \left(\sum_{k''_1, k'_2} \mathrm{P}_B(k_1 - k''_1 \,|\, \lambda_{B1}) \, \mathrm{P}_B(k_2 - k'_2 \,|\, \lambda_{B2}) \, \mathrm{P}_{det}(k''_1 \,|\, N - k'_2, \eta) \, \frac{(N - k'_2) + 1}{(N+1)(N+2)} \right) \mathrm{P}_N(N \,|\, \lambda'_N)}{\sum_{N=0}^{\infty} \left(\sum_{k''_1, k'_2} \mathrm{P}_B(k_1 - k''_1 \,|\, \lambda_{B1}) \, \mathrm{P}_B(k_2 - k'_2 \,|\, \lambda_{B2}) \, \mathrm{P}_{det}(k''_1 \,|\, N - k'_2, \eta) \, \frac{1}{(N+1)} \right) \mathrm{P}_N(N \,|\, \lambda'_N)} \tag{A.32}$$

$$\langle p^2 \rangle = \frac{\sum_{N=0}^{\infty} \left(\sum_{k''_1, k'_2} \mathrm{P}_B(k_1 - k''_1 \,|\, \lambda_{B1}) \, \mathrm{P}_B(k_2 - k'_2 \,|\, \lambda_{B2}) \, \mathrm{P}_{det}(k''_1 \,|\, N - k'_2, \eta) \, \frac{((N - k'_2) + 1)((N - k'_2) + 2)}{(N+1)(N+2)(N+3)} \right) \mathrm{P}_N(N \,|\, \lambda'_N)}{\sum_{N=0}^{\infty} \left(\sum_{k''_1, k'_2} \mathrm{P}_B(k_1 - k''_1 \,|\, \lambda_{B1}) \, \mathrm{P}_B(k_2 - k'_2 \,|\, \lambda_{B2}) \, \mathrm{P}_{det}(k''_1 \,|\, N - k'_2, \eta) \, \frac{1}{(N+1)} \right) \mathrm{P}_N(N \,|\, \lambda'_N)} \tag{A.33}$$

With the binomial distribution

$$\mathrm{P}_{det}(k_1'' \,|\, N - k_2', \eta) = \binom{N - k_2'}{k_1''} \, \eta^{k_1''} \, (1-p)^{N-k_2'-k_1''} \tag{A.34}$$

Although the exterior sum can be aborted at a finite value because of the Poissonian statistics, the interior sum makes the computational effort much higher compared to case III.

Summary

Four cases and procedures to estimate the splitting probability of a finite set of projective measurements were discussed in this section. The expectation value $\langle p \rangle$ and its standard deviation Δp were used as estimators and its uncertainty. The ideal case (I) is for example used to estimate the probabilities for the atomic state reconstruction (*c.f.* section 4.2.2) with the fluorescence detection method. Case IV with considered background and detection efficiencies is used in the quantum network experiments (*c.f.* section 4). The methods for background correction of this section are only practicable for relatively small data sets, because of the large computational effort.

A.2. Polarization-basis correction scheme

The correction scheme uses a reference point in which the polarization is in fixed relation with the polarization at the location of the ion. This enables us to measure the polarization changes of the fiber that connects the photons from the photon-pair source with the ion setup.

Three basic mechanisms are needed to describe the behavior of the optical components: rotations, attenuation, and polarizing effects. A sufficient method to describe these effects is the Müller calculus, that forms a set of matrices that manipulate the polarization of light described as stokes-vectors $\vec{S}$. For the correction scheme only rotations M_{rot} are considered. These are described by three-dimensional real rotation matrices R that operate on the $\{S_1, S_2, S_3\}$ subspace

$$\vec{S}_{out} = \mathrm{M}_{rot}\ \vec{S}_{in} \qquad \mathrm{M}_{rot} = \begin{pmatrix} 1 & 0 & 0 & 0 \\ 0 & & & \\ 0 & & \mathrm{R} & \\ 0 & & & \end{pmatrix} \tag{A.35}$$

In this description, the phase information of the light traveling in the channel is lost, which is not necessary for the compensation scheme. We measure these rotations by sending $n \geq 3$ different polarizations $\vec{S}_{i,in}$ and detecting the polarization $\vec{S}_{i,out}$ after the channel with a polarimeter[3]. One possibility to estimate the rotation matrix M_{rot} of equation A.35 is to use three linear independent input vectors and measure the output vectors. The rotation matrix is then given by

$$\rightsquigarrow \quad \mathrm{M}_{rot} = \left(\vec{S}_{1,out}, \vec{S}_{2,out}, \vec{S}_{3,out}\right) \cdot \left(\vec{S}_{1,in}, \vec{S}_{2,in}, \vec{S}_{3,in}\right)^{-1} . \tag{A.36}$$

But due to measurement noise and polarizing effects this can result in matrices with determinant unequal to one, which is a prerequisite for rotation matrices. A solution to decrease the measurement noise is to take the mean value of several measurements, and a solution to obtain the rotation is based on singular-value decomposition (SVD) of the matrix $\mathrm{M} = \mathrm{U}\Sigma\mathrm{V}^{\dagger}$). SVD of a matrix leads to two rotation matrices U V and the diagonal matrix Σ which contains the singular values. The singular values contain the polarizing effects of the channel which are neglected in this procedure. The rotations (U,V) are now determined by

$$\sum_{i=1}^{n\geq 3} \vec{S}_{i,in} \cdot \vec{S}_{i,out}^{T} \qquad \xrightarrow{\text{SVD}} \qquad \mathrm{U}, \mathrm{V}^{\dagger} \tag{A.37}$$

[3]Thorlabs, PAX5710IR

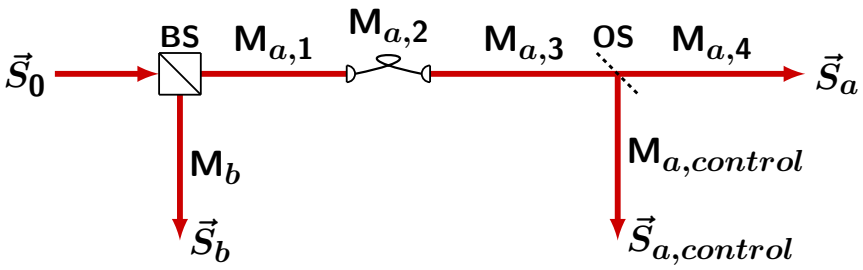

Figure A.5.: Schematic of the setup.

whereby the sum over more than three input polarizations accounts for the averaging. The Rotation matrix is then calculated by

$$M_{rot} = \begin{pmatrix} 1 & 0 & 0 & 0 \\ 0 & & & \\ 0 & & \mathrm{V}\cdot\mathrm{U}^{\dagger} & \\ 0 & & & \end{pmatrix} \tag{A.38}$$

A notional setup to explain the scheme to compensate for polarization drifts is sketched in figure A.5. A laser with polarization $\vec{S}_0$ enters the non polarizing beam splitter (BS), the reflected output beam is rotated by M_b, and the output polarization $\vec{S}_b$ is detected. In the atom-photon experiment is this the arm with the polarization projection setup. The transmitted beam is rotated by $\mathrm{M}_{a,1}$, then enters a single mode optical fiber where it gets rotated by $\mathrm{M}_{a,2}$ that is affected by any change in the environment (e.g. temperature, mechanical stress). The rotations behind the fiber to the optical switch (OS) are described by $\mathrm{M}_{a,3}$. One path of the switch gets rotated by $\mathrm{M}_{a,4}$, and ends in a polarization $\vec{S}_a$, which corresponds to the polarization at the position of the ion. The other path gets rotated by $\mathrm{M}_{a,control}$, and ends in a polarization $\vec{S}_{a,control}$, the polarization at the reference point. To describe the scheme we use the composite rotation matrices U_{ion} and $\mathrm{U}_{control}$ defined by

$$\begin{aligned} \vec{S}_b &= \mathrm{M}_b\,\vec{S}_0 \\ \vec{S}_a &= \underbrace{\mathrm{M}_{a,4}\,\mathrm{M}_{a,3}\,\mathrm{M}_{a,2}\,\mathrm{M}_{a,1}}_{\mathrm{U}_{ion}}\,\vec{S}_0 \\ \vec{S}_{a,control} &= \underbrace{\mathrm{M}_{a,control}\,\mathrm{M}_{a,3}\,\mathrm{M}_{a,2}\,\mathrm{M}_{a,1}}_{\mathrm{U}_{control}}\,\vec{S}_0 \end{aligned}$$

With these two matrices we calculate the rotation K

$$\mathrm{K} = \mathrm{U}_{ion}\cdot\mathrm{U}_{control}^{-1} = \mathrm{M}_{a,control}^{-1}\,\mathrm{M}_{a,4} \quad\rightsquigarrow\quad \vec{S}_a = \mathrm{K}\,\vec{S}_{a,control} \tag{A.39}$$

that connects the outputs of the switch. That means if we know K, we only need to measure the rotation $\mathrm{U}_{control}$ to the reference point, and we can reconstruct the rotation to the ion U_{ion}.

The input polarization in the ion-photon experiments is the polarization of the photon pairs. $\vec{S}_a$ is the corresponding polarization at the ion's position, and $\vec{S}_b$ is the corresponding polarization in front of the projection setup. $\vec{S}_{a,control}$ is the polarization at the auxiliary measurement position where the polarimeter is placed. What we need in the end, is a scheme that gives us the correct projection polarizations $\vec{S}_b$ in the ion's reference frame, and we want to be able to detect changes on the way to the ion. One problem is to find the ions reference frame. We cannot place a polarimeter direct at the ions position or at least without any further optical elements between the ion and the polarimeter, because the ion trap and the high numerical aperture laser objective (HALO) are located in the vacuum vessel. This opens two possibilities, the first is to neglect for the rotations caused by the view-port and HALO, the second is to measure the polarization with the ion itself. The scheme presented in the following uses the second approach. The quantization axis and the direction under which we excite the ion are collinear, so we drive only σ transitions.

The procedure to initialize the compensation scheme is the following:

1. Measure the rotations M_b and $\mathrm{U}_{control}$ with a laser and the polarimeter.

2. Adjust the input polarization $\vec{S}_0$ that only the σ^+ (or σ^-) transition is driven. Call this polarization $\vec{S}_{0,R}$ ($\vec{S}_{0,L}$). Ideally these two polarizations are orthogonal, if not then there are partial-polarizing elements in the path that will not be considered here.

3. Calculate 4 'pairwise-cyclic-orthogonal' vectors $\left\{\vec{S}_{0,H}, \vec{S}_{0,D}, \vec{S}_{0,V}, \vec{S}_{0,A}\right\}$ that are in the equatorial plane between the poles $\vec{S}_{0,R}$ and $\vec{S}_{0,L}$. These polarizations rotated by the matrix U_{ion} are the linear superpositions of the right- and left circular polarization that we treat as the ion's reference frame. The relations

$$\begin{aligned} \vec{S}_{a,H} &= \mathrm{U}_{ion}\,\vec{S}_{0,H} \quad & \vec{S}_{a,D} &= \mathrm{U}_{ion}\,\vec{S}_{0,D} \quad & \vec{S}_{a,R} &= \mathrm{U}_{ion}\,\vec{S}_{0,R} \\ \vec{S}_{a,V} &= \mathrm{U}_{ion}\,\vec{S}_{0,V} \quad & \vec{S}_{a,A} &= \mathrm{U}_{ion}\,\vec{S}_{0,A} \quad & \vec{S}_{a,L} &= \mathrm{U}_{ion}\,\vec{S}_{0,L} \end{aligned}$$

   lead to the rotation matrix U_{ion}. There is a missing unknown rotation around the S_3-axis that enters the total outcome as a constant phase in the mapped qubit in the ion.

4. Calculate the projector polarizations $\vec{S}_{b,\{H,D,V,A,R,L\}} = M_b\,\vec{S}_{0,\{H,D,V,A,R,L\}}$.

The following steps update the projector settings:

1. Measure $\mathrm{U}_{control}$.
2. Calculate $\mathrm{U}_{ion} = K \cdot \mathrm{U}_{control}$.
3. Calculate the corrected polarizations $\vec{S}_{0,\{H,D,V,A,R,L\}} = \mathrm{U}_{ion}\,\vec{S}_{\{H,D,V,A,R,L\}}$.
4. Calculate the new projector polarizations $\vec{S}_{b,\{H,D,V,A,R,L\}} = M_b\,\vec{S}_{0,\{H,D,V,A,R,L\}}$.

The compensation scheme is tested in an experimental situation in the following manner. We simulate the unknown rotations by waveplates that are available in our laboratory for the different wavelength, and that are inserted with arbitrary angle. The matrices $\mathrm{M}_{a,4}$, and $\mathrm{M}_{a,control}$, both represented by such a test waveplate, remain untouched during the test. Instead of using the ion we also use the polarimeter as a 'fake-ion' to measure $\vec{S}_a$ and follow the initialization instructions. To test the scheme, we insert a test waveplate in front of a flip-mirror that represents the optical switch (OS), and follow the update instructions. The polarizations of step 3 are then send through the setup, and measured with the polarimeter at the 'fake-ion' position. Figure A.6 shows the measured polarizations for 30 different rotations. The six spots

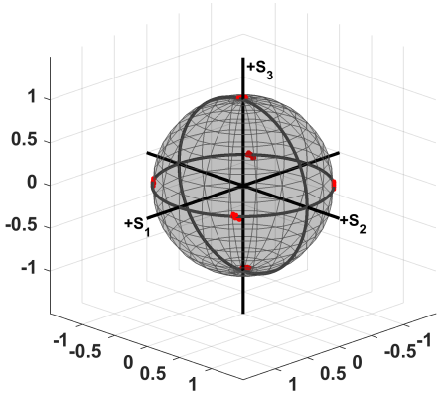

Figure A.6.: Experimental proof of the compensation protocol with 30 repetitions.

each contain 30 data points. The right and left circular polarization match with the polarimeter, and the $|R\rangle/|L\rangle$ superpositions show the expected phase offset.

Publications

S. Kucera, J. Arensk̈otter, M. Kreis, P. Eich, P. Müller, J. Eschner: Photon-photon to atom-photon entanglement transfer to a $^{40}Ca^{+}$ quantum node and state readout by teleportation. *In preparation*

M. Bock, P. Eich, S. Kucera, M. Kreis, A. Lenhard, C. Becher, J. Eschner: High-fidelity entanglement between a trapped ion and a telecom photon via quantum frequency conversion. *Nat. Commun.* **92**, 1998 (2018)

A. Lenhard, M. Bock, C. Becher, S. Kucera, J. Brito, P. Eich, P. Müller, J. Eschner: Telecom-heralded single-photon absorption by a single atom. *Phys. Rev. A* **92**, 063827 (2015)

J. Brito, S. Kucera, P. Eich, P. Müller, J. Eschner: Doubly-heralded single-photon absorption by a single atom. *Appl. Phys. B*, 122:36 (2016)

A. Lenhard, J. Brito, S. Kucera, M. Bock, J. Eschner, C. Becher: Single telecom photon heralding by wavelength multiplexing in an optical fiber. *Appl. Phys. B*, 122:20 (2016)

Danksagung

Am Ende meines Studiums möchte ich mich bei allen bedanken die mich auf dem Weg begleitet haben. An erster Stelle geht mein Dank an Jürgen Eschner der es mir ermöglicht hat an diesem außerordentlich spannenden Experiment zu arbeiten. Er schafft durch seine stets offene Tür und den großen Handlungsfreiraum ein äußerst angenehmes Arbeitsklima, auf das ich mich noch eine Zeit lang freuen darf. Mein weiterer Dank geht an die Kollegen mit denen ich Tage und Nächte im Labor und auch darüber hinaus verbringen konnte. Besonders ist José zu nennen: wir waren schließlich die *Hüter der alten Quelle*. Die Diskussionen mit südamerikanischem Temperament, Klettertouren und Partys werden hoffentlich nicht enden. Auch möchte ich mich bei Hannes für die Diskussionsbereitschaft und Aktivitäten außerhalb der Universität bedanken. *The ion guys:* Jan, Michael, Christoph, Matthias und besonders meine Zimmerkollegen Pascal und Philipp haben ebenfalls zum Gelingen dieser Arbeit beigetragen. Auch Andreas und Matthias, die Kollegen am Konverter, sind an dieser Stelle zu nennen. Der nächsten PhD Generation, darunter besonders Jan dem Mitstreiter an der neuen Quelle, wünsche ich viel Erfolg mit den bevorstehenden Experimenten und Herausforderungen. Zu guter Letzt möchte ich mich noch bei meiner Familie für die Unterstützung während der gesamten Zeit bedanken.